Mechanical properties of homogenous polymers and block copolymers : a molecular dynamics simulation approach

Ali Makke

N° d'ordre 67-2011 Année 2011

THESE DE L'UNIVERSITE DE LYON

Délivrée par

L'UNIVERSITE CLAUDE BERNARD LYON 1

ECOLE DOCTORALE MATERIAUX DE LYON

DIPLOME DE DOCTORAT

(arrêté du 7 août 2006)

soutenue publiquement le 29 Avril 2011
par

Ali MAKKE

MECHANICAL PROPERTIES OF HOMOGENOUS POLYMERS AND BLOCK COPOLYMERS:
A MOLECULAR DYNAMICS SIMULATION APPROACH

Directeurs de thèse : Jean Louis BARRAT et Michel PEREZ
co-Directeur de thèse: Olivier LAME

devant le jury formé de:

Joerg BASCHNAGEL (Université de Strasbourg)	Rapporteur
Bernard MONASSE (Ecole des Mines Paristech)	Rapporteur
Philippe CASSAGNAU (Université Claude Bernard, Lyon)	Examinateur
Jean-Louis BARRAT (Université Joseph Fourier, Grenoble)	Directeur de thèse
Michel PEREZ (INSA de Lyon)	Codirecteur de thèse
Olivier LAME (INSA de Lyon)	Codirecteur de thèse

Remerciements

En tous premier lieu, ces remerciements s'adressent à l'ensemble des membres du jury pour leur travail et l'intérêt qu'ils ont porté à cette thèse. Merci donc, M. Cassagnau pour votre présidence, M. Baschnagel et M. Monasse pour votre examen et vos rapports. Vous avez également ensemble permis la construction d'une discussion riche et ouverte à l'issue de la présentation de ce travail.

Toute ma reconnaissance s'adresse maintenant à mes encadrants qui au fil de mes années de thèse, m'ont aidé à mener à bien ce travail.

Merci Jean-Louis pour les discussions riches, la pédagogie et la patience dont tu as toujours fait preuve. Tu as été pour moi durant ces trois années un bon exemple de créativité et de sagesse.

Merci Michel pour l'énergie, l'enthousiasme et la passion que tu sais si bien transmettre. Tu as su à chaque période de doute de relancer une nouvelle dynamique.

Merci Olivier pour ta disponibilité et ta générosité, Merci d'avoir été justement présent, rigoureux et encourageant.

Merci mes encadrants pour tout, je souhaite que les valeurs scientifiques que vous incarnez, m'inspirent et m'accompagnent dans ma vie scientifique.

Ce travail a également été l'objet d'une collaboration extérieure au laboratoire. Je souhaite remercier M. Rottler de l'université de British Columbia, pour son accueil, son aide et sa disponibilité lors de mon stage à Vancouver.

Merci à l'ensemble des membres du MATEIS et LPMCN surtout le groupe PVMH qui participent à la bonne ambiance de travail et entretiennent un esprit stimulant au quotidien.

Merci encore à l'ensemble des membres du comité des clusters : P2CHPD et CINES qui m'ont offert les heures de calcul pour réaliser mes simulations.

Je souhaite encore remercier l'équipe d'enseignement de Science des Matériaux à L'IUT B Jean Colombani, Laurent Joly et Vittoria Pischedda pour m'avoir aider à développer une bonne expertise dans l'enseignement.

J'adresse encore mes remerciements à mes profs de Master: Sylvain Meille, Jérôme Chevalier, Jean-Yves Cavailler, Eric Maire, Jean-Yves Buffiere, Alain Vincent, Dominique Rouby, Olivier Dezelus...

Un remerciement spécial pour M. Gérard Guillot et M. Mohammed Zoaiter qui m'ont aidé pour venir faire mon Master en France dans le cadre d'une collaboration universitaire Franco-Libanaise.

Que tous mes collègues les thésards trouvent ici de ma plus sincère sympathie pour l'amitié qu'ils m'ont témoigné au cours de ces 3 années. Un gros Merci à l'ensemble du personnel administratif et technique du MATEIS.

Qu'il me soit permit d'exprimer ma plus profonde gratitude et reconnaissance à tous les membres de ma famille en particulier à mes parents pour le soutien et l'amour qui m'ont toujours démontré tout au long de ma vie.

Table des matières

Introduction

0.1 Elastomères *vs* thermoplastiques

Les polymères suscitent un grand intérêt dans des domaines industriels tels que l'aéronautique, l'électronique, l'automobile, le textile,... par leur facilité de mise en œuvre, leur masse volumique faible et leur moindre coût.

Un challenge essentiel pour l'avenir des matériaux polymères est de rendre leur fabrication et leur utilisation compatible avec des attentes environnementales de plus en plus fortes. Dans ce cadre le remplacement d'une part des élastomères non recyclables par des équivalents thermoplastiques est d'un grand intérêt. Ces derniers doivent cependant respecter le même cahier des charges notamment en termes de propriétés mécaniques.

De larges études ont été réalisées dans ce sens dans le but de bien comprendre le comportement mécanique des polymère thermoplastiques ainsi que les paramètres pertinents d'élaboration et de traitement qui permettent d'améliorer la résistance (mécanique, thermique, chimique...) de ces matériaux. Les polymères nanostructurés lamellaires tel que les copolymères bloc ou les semi cristallins attirent de plus en plus l'attention pour leur propriétés thermoplastiques couplées avec de bonnes propriétés mécaniques. Ces types de polymères sont caractérisés par des morphologies et des nanostructures très particulières qui répondent d'une manière complexe aux sollicitations mécaniques macroscopiques.

Les propriétés mécaniques de ces systèmes sont l'expression macroscopique de mouvements à l'échelle moléculaire. C'est pourquoi ce travail de recherche est orienté vers l'étude de la réponse mécanique des polymères et des copolymères bloc en simulant la dynamique moléculaire des chaines par une approximation grossière appelée "gros grains " ou "coarse grained " afin d'optimiser et comprendre l'origine des propriétés mécaniques des polymères nanostructurés lamellaires.

0.2 Apports de la simulation numérique

Depuis environ 6 décades la simulation numérique progresse et devient de plus en plus un outil prépondérant dans la recherche scientifique et la conception (figure 1). Ce domaine ne cesse de progresser grâce à l'évolution continue dans l'informatique (Langages et techniques de programmation, ordinateur, clusters de calcul, etc...). Le but de la simulation est double : d'une part c'est de vérifier les hypothèses physiques qui permettent d'interpréter le phénomène simulé et de tester de nouvelles idées permettant de progresser dans la compréhension du comportement locale de ces systèmes, et, d'autre part de prédire la réponse d'un matériau sous des conditions limites complexes.

Grâce au progrès considérables réalisés dans les méthodes de simulation, ces derniers peuvent être considérées comme des méthodes pluridisciplinaires et multiéchelles. La simulation s'intègre comme un ingrédient important dans des divers

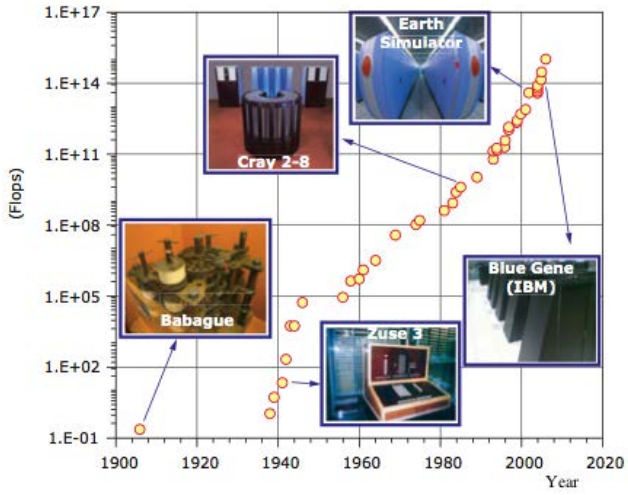

FIGURE 1 – Évolution de la puissance des calculateurs en Flops (Floating operations per second) au cours du dernier siècle [Becquart 2010].

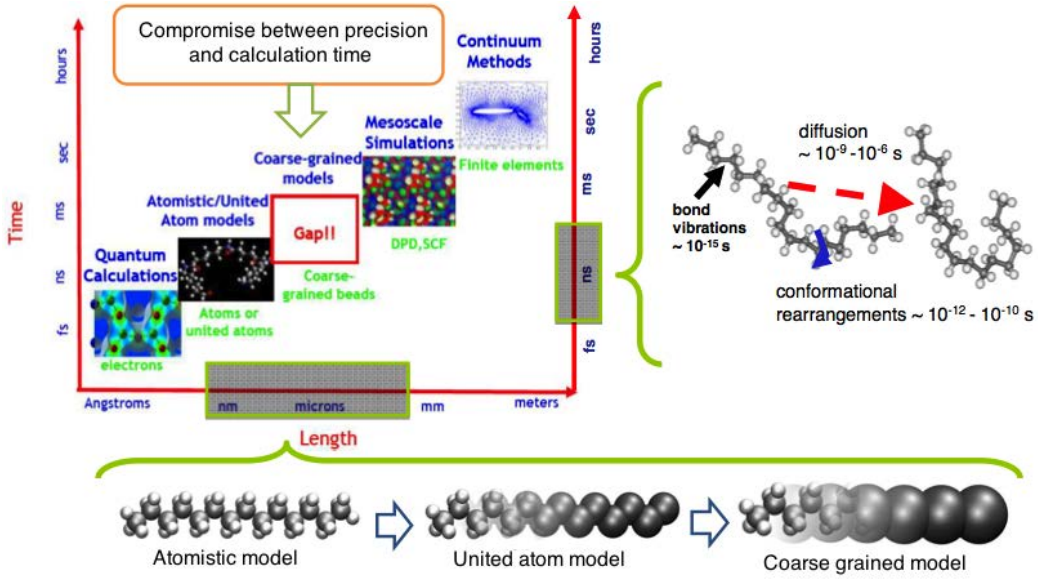

FIGURE 2 – les différentes méthodes de simulation et leurs échelles caractéristiques (temps et distance).

domaines scientifiques allant de la biologie jusqu'au mécanique en passant par la chimie et la physique des matériaux en recouvrant aussi une large échelle allant de quelques nanomètres (dans les méthodes de ab-initio) jusqu'à quelques km (dans les méthodes des élément finis) voire encore quelques dizaines d'années lumières dans les méthodes de Monte Carlo utilisées dans la simulation de Galaxies.

Afin d'optimiser le temps de calcul tout en obtenant les renseignements détaillés

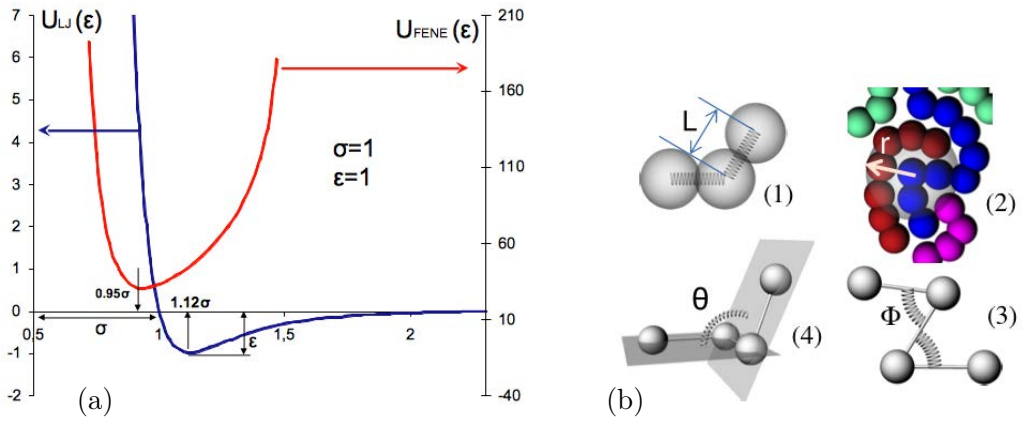

FIGURE 3 – (a) Les potentiels d'interactions Lennard Jones et FENE utilisés pour décrire les liaison faibles (Van der Waals) et fortes (covalentes). (b) les différents interactions inter et intra chaine (1) les liaisons covalentes, (2) les liaisons faibles, (3) la flexion entre deux liaisons covalentes successives et (4) l'angle dièdre.

recherchés pour le phénomène étudié, il est judicieux de choisir pour chaque simulation le modèle dont la longueur caractéristique correspond le mieux avec la longueur caractéristique du phénomène simulé. Pour réaliser notre étude sur le comportement mécanique de polymères, plusieurs types de simulation sont possibles. Dans notre étude on s'intéresse particulièrement à l'évolution de la configuration testée au cours de la déformation.

Ces configurations sont suffisamment représentatives pour assurer l'observation des évènements étudiés (la formation des cavités, le flambement des phases...) qui se déroulent réellement à une échelle très petite (quelque dizaines de nanomètre). C'est pour cela que le choix de la méthode de simulation est contraint d'une part par l'échelle de longueur et d'autre part par la durée de l'évènement. La dynamique moléculaire est une méthode particulièrement adaptée à notre étude. Cette méthode est parfaitement adaptée à la simulation des modèles de polymère à plusieurs échelles allant de la description atomique détaillée des chaines de polymère (modèle toute atome) jusqu'à la description grossière des chaines par le modèle “coarse grained” en passant par la description “meso” dans le modèle “atome unifié”. Compte tenu de l'objectif principal de cette thèse orientée vers l'étude des propriétés mécaniques des polymères, la prise en compte des détails chimiques dans le modèle de simulation ne présente qu'un intérêt limité et complexifie le modèle en augmentant de manière rédhibitoire le temps de calcul. Pour cette raison l'échelle de “coarse grained” est le choix le plus judicieux pour ces travaux de thèse.

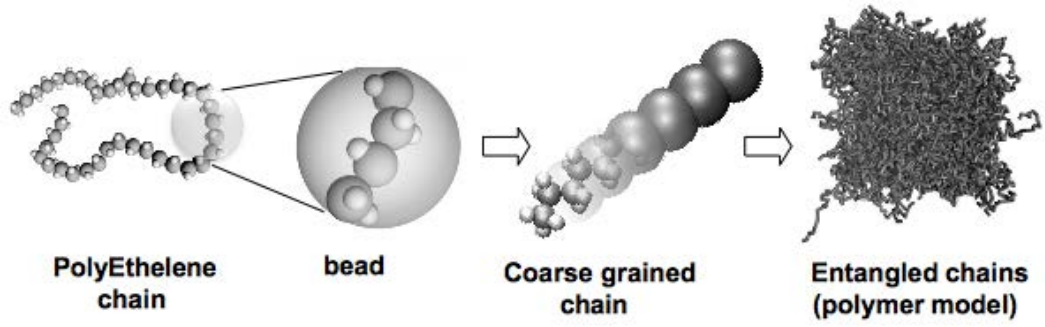

FIGURE 4 – Echantillon d'un polymer amorphe à l'échelle "coarse grained" (figure reproduit de [Schnell 2006, Becquart 2010])

0.3 Modèle "coarse grained " ou masse ressort

Dans un modèle masse-ressort une chaine de polymère est assimilée à un collier de perles liées entre elles par des ressorts. Ces perles représentent effectivement une séquence de particules connectées entre elles par des liaisons covalentes. Pour bien reproduire les interactions moléculaires d'un polymère réel, deux types d'interaction sont retenus. (1) les liaisons fortes entre deux "perles" ou masses consécutives qui représentent les liaisons covalentes et (2) les liaisons faibles qui représentent les liaisons de Van Der Waals.

Il existe des autres types d'interaction plus ou moins pertinentes qui ne sont pas pris en compte par nos modèles : (3) l'énergie de flexion entre deux liaisons successive et (4) l'énergie de l'angle dièdre (la torsion d'un liaison) (figure 3.b). L'interaction des liaisons faibles est prise en compte par le potentiel de Lennard Jones qui décrit l'interaction d'une particule avec ses proches voisins (équation 1.1 tracée dans la figure 3.a). L'interaction des liaisons covalente est modélisée par un potentiel FENE (Finite Extensible Nonlinear Elastic) dont les paramètres sont choisis de telle manière que deux chaines ne peuvent pas se traverser l'une l'autre (équation A.2 tracée dans la figure 3.a).

Le modèle bille ressort utilisé conserve les propriétés statistiques des chaines (distance de bout à bout, rayon de giration, longueur de persistance, etc...) sans faire appel à la description atomistique de ces chaines. Cette propriété présente le grand avantage d'économiser du temps de calcul sans trop perdre d'information au niveau de la description microstructurale des systèmes simulés (fluctuation des propriétés locales, enchevêtrement des chaines....). La génération des échantillons pour la simulation a été effectuée par l'algorithme de " "Radical-like polymerization " qui sera détaillé dans l'annexe de cette thèse.

0.4 Objectifs et organisation de ce travail

L'objectif principal visé par cette thèse consiste à essayer d'apporter par le biais de la simulation numérique de modèles " Coarse grained " des éléments nouveaux permettant d'améliorer la compréhension des processus moléculaires ayant, à priori, lieu dans les polymères amorphes homogènes ou nanostructurés lors d'une sollicitation mécanique. On s'intéresse particulièrement au comportement mécanique des modèles testés dans le but de corréler la réponse mécanique avec les paramètres moléculaires du modèle (densité d'enchevêtrement, l'architecture moléculaire) et/ou les propriétés locales du système. (fluctuation de la microstructure, les modules élastiques...)

Deux types des systèmes feront l'objet de notre étude : les polymères homogènes amorphes (chapitres 1,2 et 3) et les polymères nanostructurés lamellaires, ou copolymères bloc (deux derniers chapitres).

La nucléation des cavités dans les homo-polymères amorphes ainsi que la relation entre les sites de la cavitation et les propriétés mécaniques locales du système et l'un des objectifs ciblés par nos travaux. L'utilisation d'un modèle " coarse grained " pour l'étude de cette problématique est avantageux vu que l'échelle de la simulation ainsi que les variables mesurées sont difficilement accessibles par les outils expérimentaux, en plus dans la bibliographie la majorité des travaux de la simulation moléculaire ont été plutôt orientés vers l'étude de la plasticité du polymère (écoulement) que la cavitation.

Les propriétés mécaniques des polymères nanostructurés sont également l'objet de notre étude. En se basant sur un modèle " coarse grained " développé pour ces systèmes, le comportement mécanique de ces derniers a été simulé. L'avantage principal fourni par l'approche dynamique moléculaire dans ce cas est la facilité à contrôler et tester l'influence de chaque paramètre moléculaire indépendamment : (rôle des chaines liant les phases dures du copolymère bloc, effet de la tension de surface entre les blocs du copolymère. . ..).

La comparaison directe entre les résultats de la simulation DM et les résultats expérimentaux ne peut pas être quantitative à cause des nombreuse hypothèse simplificatrice sous-jacentes à notre approche : approximation " coarse grained ", vitesse de traction très élevée, taille de l'échantillon faible, etc...). Cependant, les résultats de la simulation DM montrent un bon accord avec l'expérience du point de vu qualitatif ce qui apporte un certain crédit aux simulations. Nous verrons que cette comparaison devient de plus en plus intéressante dans l'étude de flambement des phases dans les polymères nanostructurés lamellaires où un accord très satisfaisant est observé avec des modèles analytiques.

L'ensemble du travail est exposé dans ce manuscrit en cinq chapitres :

Le premier chapitre présente une comparaison des deux méthodes de traction : la méthode homogène qui consiste à déformer le système d'une manière affine puis à le relaxer et la méthode de la déformation pilotée par les bords inspirée de la traction des éprouvettes réelles. La deuxième méthode a été développée pour qu'elle s'adapte à des différentes conditions limites (uni-axiales et tri-axiales). Nous y aborderons

également le durcissement observé dans les essais uni-axiaux.

Dans le deuxième chapitre l'analyse de l'évolution de la densité d'enchevêtrement au cours des essais uni-axiaux et tri-axiaux sera présentée. Une grande attention sera apportée à l'observation des deux évènements contradictoires, mais simultanés : durcissement structural de l'échantillon et désenchevêtrement des chaines.

La nucléation des cavités dans les modèles des polymères amorphes fera l'objet du troisième chapitre : une analyse détaillée des propriétés locales (microstructurales et mécaniques) sera présentée dans le but d'identifier les sites les plus probables de la nucléation des cavités.

Dans le chapitre 4 : l'étude des propriétés mécaniques des modèles des copolymères tri-bloc sera présentée. Tous d'abord : la température de transition vitreuse de chaque phase sera identifiée dans le but de bien choisir la température des essais mécaniques numériques. A cette température, l'un des composants est à l'état caoutchoutique tandis que les autres blocs sont vitreux. Le comportement du modèle soumis à des essais de traction uni-axiale classique sera présenté. L'influence de l'architecture moléculaire sur la transmission des contraintes entre différentes phases sera détaillée ainsi que l'influence de la tension de surface entre les phases sur la cavitation.

L'étude du flambement des phases dans les copolymères à blocs par un modèle MD sera détaillée dans le cinquième et dernier chapitre de cette thèse. L'interprétation du phénomène de flambement en se basant sur l'état de contrainte locale de chaque phase sera présentée. La réponse mécanique des ces échantillons sera détaillée. Une analogie avec les résultats expérimentaux sera également présentée. L'influence de la taille d'échantillon sur la réponse mécanique ainsi que l'influence de la vitesse de traction seront étudiées. Les résultats seront discutés et interprétés dans l'optique d'un modèle analytique existant. Un modèle qui prend en compte l'influence de la cinétique du flambement sera suggéré pour interpréter la compétition entre les différents modes de flambement.

Chapitre 1

Mechanical testing of amorphous polymers

Contents

This chapter essentially reproduces the article [Makke 2009] published in Journal of Chemical Physics.

1.1 Introduction

Molecular dynamics (MD) simulations have now become a standard tool to investigate the mechanical response of model polymer systems under various conditions of deformation [Lyulin 2004, Rottler 2003, Hoy 2006, Schnell 2006]. Despite their well known shortcomings (small system sizes, large deformation rates) they are able to give a precise description of the molecular mechanisms at work during the deformation process [Papakonstantopoulos 2007], of the changes in entanglement networks [Hoy 2006] or to describe elastic heterogeneities [Yoshimoto 2004, Papakonstantopoulos 2008].

Despite their success, MD simulations are sometimes questioned in terms of their relevance to actual experiments. We already mentioned the issue of length and time scales. A third question arises from the method which is used to strain the samples, in particular when periodic boundary conditions are used. The typical MD calculation proceeds by straining the whole system at each time step in a completely homogeneous manner, with an imposed deformation rate or deformation velocity. Such a procedure is clearly different from the one used in experiments, in which the strain is transmitted to the sample through the imposed motion of the boundary. Indeed, homogenous deformation procedure leads to non physical local stretching

(small fluctuations), which could possibly be amplified for stochastic phenomena, *e.g.* the onset of plasticity. This is especially true in the case of glassy polymers, where the plastic deformation proceeds by individual plastic events that correspond to local instabilities of the system. Such instabilities will, generally speaking, be dependent on the precise deformation trajectory.

Another reason for interrogating the different deformation procedures is the current interest in nonhomogeneous polymeric systems, *e.g.* semi crystalline polymers, segregated block copolymers or polymer nanocomposites ; In such systems, the stress is transmitted from hard zones to softer zones of the material, with zones that are often of nanometric dimensions. The strain in the soft part will obviously be much larger that in the hard zones, which may even be considered as non deformable. The situation is then similar to a mechanical testing experiment at the nanometer scale, where the role of the "grips" is played by the harder zones in the composite material. In studying the deformation of the material as a whole, it is therefore interesting to understand the scale and size effects on the deformation of the softer part. To what extent can the deformation of a soft, nanometric zone be described using the stress-strain relation of an homogeneously deformed bulk material of the same nature ?

In order to investigate these two aspects, we have studied the deformation of glassy and rubbery polymer systems using standard periodic boundary conditions and homogeneous strain, and compared the resulting stress strain curves to those obtained using a boundary driven method. The boundary driven method introduces the molecular equivalent of grips, adapted to both uniaxial and triaxial tests. The "grips" are identical to the deformed material in terms of interaction potentials, but impose a constrained motion to the system boundary.

The next section describes sample preparation and the different deformation methods. Our results are presented in section 1.4.

1.2 Simulation techniques and sample generation

Our simulations are carried out for a well established coarse-grained model [Kremer 1990, Rakshit 2006] in which the polymer is treated as a chain of N beads which we refer to as monomers, of mass $m = 1$ connected by a spring to form a linear chain. The beads interact with a classical Lennard-Jones interaction :

$$\mathrm{U}_{\mathrm{LJ}}^{\alpha\beta}(\mathrm{r}) = \begin{cases} 4\varepsilon_{\alpha\beta}\left[(\sigma_{\alpha\beta}/r)^{12} - (\sigma_{\alpha\beta}/r)^{6}\right] & , r \leq r_c \\ 0 & , r \geq r_c \end{cases} \tag{1.1}$$

where the cutoff distance $r_c = 2.5\sigma_{\alpha\beta}$. In addition to (1.1), adjacent monomers along the chains are coupled through the well known anharmonic Finite Extensible Nonlinear Elastic potential (FENE) :

$$\mathrm{U}_{\mathrm{FENE}}(\mathrm{r}) = \begin{cases} -0.5kR_0^2 \ln\left(1 - (r/R_0)^2\right) & , r \leq R_0 \\ \infty & , r > R_0 \end{cases} \tag{1.2}$$

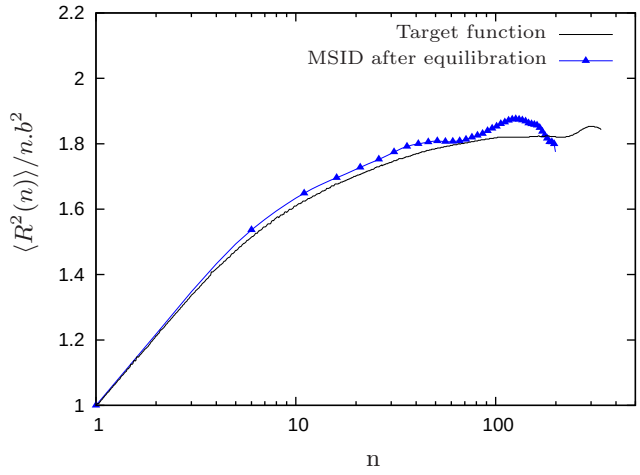

FIGURE 1.1 – Mean square internal distance (MSID) of mono-disperse melts ($k_bT = 2\ \varepsilon$). The effect of the number of MD steps between each growth step is studied. A larger value of n_{MDSbG} leads to better equilibrated systems, whom which MSID fits nicely with FPO and the target function of Auhl [Auhl 2003].

The parameters are identical to those given in Ref.[Kremer 1990], namely $k = 30\varepsilon_{\alpha\beta}/\sigma^2_{\alpha\beta}$ and $R_0 = 1.5\sigma_{\alpha\beta}$, chosen so that unphysical bond crossings and chain breaking are avoided. All quantities will be expressed in terms of length $\sigma_{\alpha\beta} = \sigma$, energy $\varepsilon_{\alpha\beta} = \varepsilon$, pressure ε/σ^3 and time $\tau_{LJ} = \sqrt{m\sigma^2/\varepsilon}$.

Newton's equations of motion are integrated with velocity-Verlet method and a time step $\delta t = 0.006$ [Allen 1987]. Periodic simulation cells of cubic size L containing M chains of size N were used under a Nosé-Hoover barostat, *i.e.* in the NPT ensemble. The pressure is fixed to $P = 0.5\ \varepsilon/\sigma^3$.

Our specimens are prepared using Radical Like Polymerization method [Perez 2008] which is an extension of Gao's work [Gao 1995]. Chains grow in monomer bath at $k_bT = 2\ \varepsilon$ and $P = 0.5\ \varepsilon/\sigma^3$. The whole system is relaxed during 300 MD steps between each growth step and polymerization is stopped when chains reach the chosen length $N = 200$ beads. Remaining single beads (solvent) are then removed and the resulting melt is equilibrated during 10^7 MD steps in NPT ensemble at low compressive pressure $P = 0.5\ \varepsilon/\sigma^3$ (see reference [Perez 2008] for more details). Figure 1.1 shows a good agreement between the normalized mean square internal distance (MSID) compared to the target function published by Auhl [Auhl 2003].

Rubbery and glassy states are obtained by cooling to $k_BT = 0.5\ \varepsilon$ and $k_BT = 0.2\ \varepsilon$ respectively. With a cooling rate of $k_B\dot{T} = -1.6 \times 10^{-3}\ \varepsilon/\tau_{LJ}$, the glass transition temperature is equal to $k_BT_g = 0.43\ \varepsilon$. Finally, an isothermal relaxation is applied to reach a zero pressure at a rate of $\dot{P} = 8 \times 10^{-5}\ \varepsilon/\sigma^3\tau_{LJ}$. Cooling and relaxation are achieved in NPT ensemble. The resulting glass and rubber have densities of $\rho_{glass} = 1.07\ \sigma^{-3}$ and $\rho_{rubber} = 1.02\ \sigma^{-3}$ respectively.

1.3 Methodology : triaxial and uniaxial tensile tests

1.3.1 Homogeneous deformation technique

The most common method used to strain a polymer specimen in numerical simulation is the homogeneous affine deformation [Rottler 2003, Hoy 2006, Schnell 2006, Capaldi 2002]. This technique is a finite sequence of two steps : deformation and relaxation. The deformation is imposed by modifying the simulation cell size in one or more direction and re-mapping all beads to the new box by a simple rescaling of all coordinates. The simulation box can be deformed at a constant elongation rate (*constant velocity*) [Schnell 2006] or non linear logarithmic strain rate [Rottler 2003]. Depending on the nature of load, homogenous tensile test allows one to modify the loading condition by controlling the amount of deformation in the three directions independently.

Axisymmetric triaxial tests -called thereafter triaxial tests- are performed by deforming the simulation box in only one direction (the tensile direction, say y), the two other dimensions remaining constant. The relaxation MD steps are integrated in the NVT ensemble (Nosé-Hover thermostat - rate of 0.1 τ_{LJ}^{-1}). The magnitude of the pressure tensor components in triaxial tests obeys the relation : $|P_{yy}| > |P_{xx}| = |P_{zz}| > 0$.

Uniaxial tests are performed by deforming the simulation box in one direction (the tensile direction, say y), the two other dimensions varying so that the pressure remains equal to zero in these directions. The relaxation MD steps are integrated in $NL_yP_xP_zT$ ensemble with anisotropic barostat which controls pressure only in x and z directions independently (Nosé-Hover thermostat and barostat - rates of 0.1 τ_{LJ}^{-1} [Nose 1984, Hoover 1984]). The magnitude of the pressure tensor components in uniaxial tests obeys the relation : $|P_{yy}| > |P_{xx}| = |P_{zz}| = 0$.

The virial stress is used to measure the true stress of our systems. The thermal contribution is small and can be neglected at these densities and temperatures.

Albeit natural, the homogenous affine method has some restrictions. The deformation is applied without respecting the bond strengths. In some case, particularly near the yield stress, this might activate violent motions or even break some high energetic stretched FENE bond.

1.3.2 Boundary driven deformation technique

1.3.2.1 Triaxial tensile test

In order to simulate a tensile test in a way that is analogous to a macroscopic experiment, we propose a method in which the deformation is applied first at boundaries and is then transmitted to the core of the sample by the material itself. To achieve this boundary driven deformation, we first remove the periodic boundary condition on the tensile axis (say y-axis), keeping the two other directions periodic. The "grips" are set to be the top and bottom parts of the sample (of size L_y in the

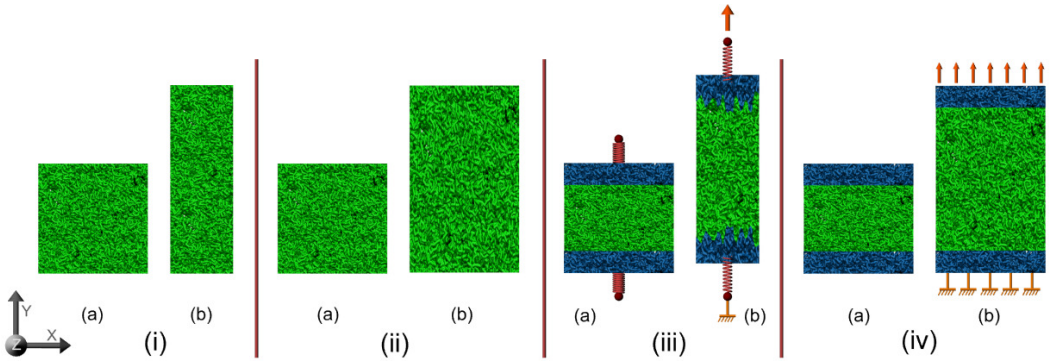

FIGURE 1.2 – Principle of the two techniques used in this paper. (From left to right) (i) homogeneous deformation uniaxial, (ii) homogeneous deformation triaxial, (iii) boundary driven deformation uniaxial, (iv) boundary driven deformation triaxial.

y direction), each of them having a thickness of 2.6σ [1] (see figure 1.2) :

$$y < 2.6\sigma \quad \rightarrow \quad \text{Lower grip} \tag{1.3}$$

$$2.6\sigma < y < L_y - 2.6\sigma \quad \rightarrow \quad \text{Gauge length} \tag{1.4}$$

$$y > L_y - 2.6\sigma \quad \rightarrow \quad \text{Upper grip} \tag{1.5}$$

Forces acting on beads belonging to the grips are set to zero. The initial velocity of lower and upper grip beads are set to zero and v_0, respectively. The lower grip is then an immobile rigid body and upper grip is submitted to a constant velocity as a rigid body. This velocity is adjusted to get the desired strain rate at initial time : $v_0 = \dot{\varepsilon_0} L_y^0$. During the tensile test, the motion of the beads inside the loaded part of the sample is integrated in a NVT ensemble (Nosè-Hover thermostat), NVE ensemble is employed to drive the motion of the grip. The volume of the loaded part $L_x(L_y - 5.2\sigma)L_z$ is used to compute the stress within the sample.

As chain breaking is not possible due to FENE bonds, it has been checked in each simulation that no chains are held by two opposite grips simultaneously. Note that with the boundary driven deformation method, as applied here on a triaxial tensile test, the deformation is limited to a single direction.

1.3.2.2 Uniaxial tensile test

In uniaxial deformations, the dimensions of the simulation box have to be relaxed in the directions perpendicular to the tensile direction [Brown 1991, Capaldi 2002, Capaldi 2004], in order to fulfill the condition : $P_{xx} = P_{zz} = 0$. Such a relaxation is not possible when using the grips of the triaxial case, that behave as rigid bodies.

1. The grips thickness must be larger than the cutoff radius to guarantee that all beads (specially those nearest to interface with the grip) have a similar environment.

A naive solution would be to zero the component of the force parallel to the traction axis ($F_y = 0$) for all atoms belonging to the grips and to apply the same velocity conditions as for the triaxial test ($v_y = 0$ for the lower grip and $v_y = v_0$ for the upper grip). However, this would lead to a very high rigidity of the grips, as their atoms would be constrained to stay in a plane perpendicular to the traction axis.

A linearly increasing force could also be applied to all beads of both grips. NPT integration with zero lateral pressure would then lead to an uniaxial tensile test. However, it would be a force-controlled tensile test, which is not well adapted to polymers exhibiting softening after the yield. This softening would lead to instabilities in such force-controlled tensile test.

The technique used in this paper is inspired from the work of Israilev *et al*, who suggested a way of extracting a ligand from the binding pocket of a protein, by the use of Steered Molecular Dynamic (SMD) [Izrailev 1998]. The basic idea of SMD is to restrain the ligand to a point in space (restraint point) by an external, *e.g.*, harmonic, potential.

In our case, instead of setting the force on grips beads to zero, we *add* a force to all beads of the grips *such that* the *mean* velocity of all these beads is the desired one. To do so, we introduce two restrained points, one for each grip : R^u and R^l with positions $\mathbf{r_R^u} = \mathbf{r_{R0}^u} + v_0 t \mathbf{e_y}$ and $\mathbf{r_R^l} = \mathbf{r_R^l}^0$ ($\mathbf{e_y}$ is the unit vector in y direction). The external force applied to all beads of upper and lower grips is given by :

$$\mathbf{F^u} = -K\left[\mathbf{r_{com}^u}(t) - \mathbf{r_{com}^u}(0) - v_0 t \mathbf{e_y}\right] \tag{1.6}$$

$$\mathbf{F^l} = -K\left[\mathbf{r_{com}^l}(t) - \mathbf{r_{com}^l}(0)\right] \tag{1.7}$$

where $\mathbf{r}_{com}^u(t)$ and $\mathbf{r}_{com}^l(t)$ are the positions of the upper and lower grip center of mass at time t. Equation 1.6 forms a feedback loop on the force applied to the upper grip. The specimen is therefore submitted to NVT conditions. Figure 1.2 shows the deformation methods used in both uniaxial and triaxial tensile tests. To ensure a zero lateral pressure, Verlet integration is performed in NPT ensemble for all beads in x and z directions. As a consequence, at each MD step, the motion of the restrained points induce a force on all beads of both grips, leading to a boundary driven deformation-controlled uniaxial tensile test.

The stiffness K of the springs has to be optimized. A too small value would lead to a loose spring absorbing all the deformation in place of the sample and a too large value would lead to numerical instabilities (due to high forces applied on grip beads - see figure 1.4). A spring 10 times as stiff as the initial sample leads to a numerically stable deformation scheme ; this value will be kept in the following.

There are two ways of calculating the stress experienced by the gauge length (or working zone) of the sample

– divide the force of the spring ($\mathbf{F^u}$ or $\mathbf{F^l}$) by the instantaneous surface of the sample ($L_x L_z$) perpendicular to the traction axis ;

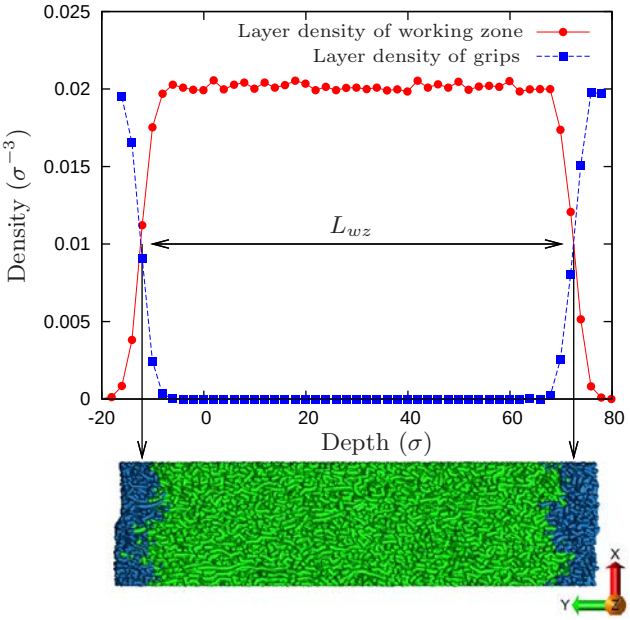

FIGURE 1.3 – Concentration profile of the sample deduced from layer analysis : the gauge length (L_{WZ}) is defined as the distance between the two inflexion points of the working zone beads concentration profile.

– compute the virial stress of the gauge length beads and divide it by the instant volume of the working zone.

The first method is simpler, but as it is averaged on less beads, it leads to a more noisy measure of the stress. The second method requires the gauge length L_g, which has been assumed to be proportional to the distance between upper and lower grips center of mass at time t $|\mathbf{r_t^{ul}}|$ over the same distance at time $t = 0$, leading to the volume of the working zone :

$$V_{WZ} = L_g L_x L_z = \frac{|\mathbf{r_t^{ul}}|}{|\mathbf{r_0^{ul}}|}(L_y - 5.2\sigma)L_x L_z \tag{1.8}$$

In order to check the accuracy of the former equation, V_{WZ} has been also calculated by a layer analysis at different deformation stages : the sample is divided in bins along to y axis and an analysis is made of the local concentration (in each layer) of grip beads, gauge length beads. This analysis leads to concentration profiles from which it is possible to measure the gauge length : distance between the two inflexion points (as shown in figure 1.3). This analysis, performed for several states of strain allowed us to validate the expression of the working zone volume (equation 1.8).

Figure 1.4 compares the stress obtained from the forces on springs or from the virial. For the values of the spring stiffness used in this work, these two measures are exactly equivalent. In what follows, the virial stress will be used preferentially as it is less noisy.

Figure 1.5 shows the time averaged velocity (averaged from initial to actual time)

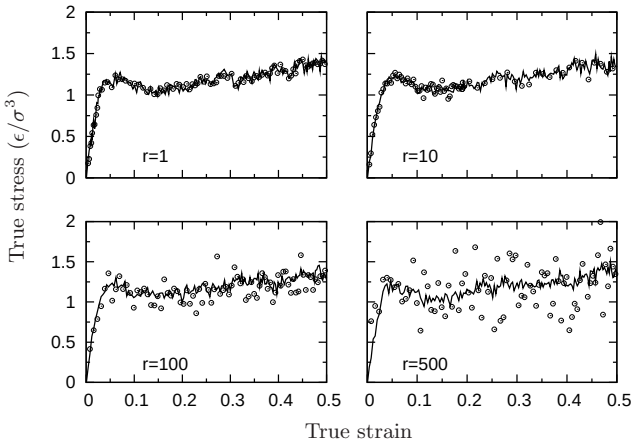

FIGURE 1.4 – Stress-strain curves (boundary driven deformation uniaxial tensile tests), at $k_BT = 0.2\ \varepsilon$, using various spring stiffness, r is the ratio of the spring stiffness over the sample stiffness. The line is the viral stress divided by the working zone volume (equation 1.8). Points ($\circ$) correspond to stress computed by the spring length. Both techniques lead to similar results.

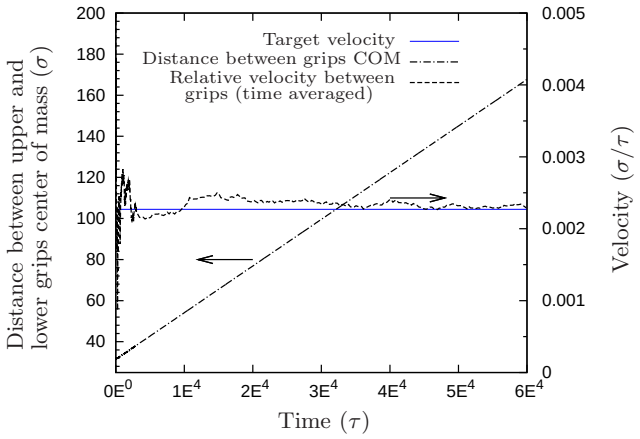

FIGURE 1.5 – Boundary driven deformation : distance between upper and lower grips center of mass (COM) versus time. secondary axes : time averaged velocity of upper grip COM with respect to lower grip COM and target velocity (0.00223 σ/τ). The mean velocity is very close to the target velocity, validating thus the uniaxial tensile technique.

of upper grip center of mass during a tensile test performed in 10^7 MD steps. It gives exactly the target value of 0.00223 σ/τ. In order to compute the appropriate temperature of any isothermal ensemble under deformation, the drawing velocity contribution is eliminated before computing the temperature.

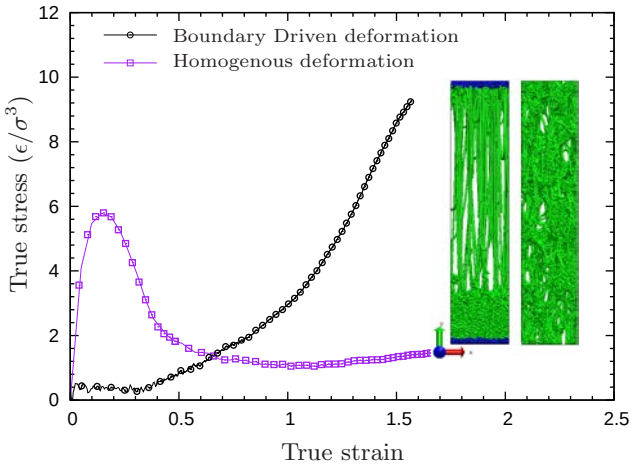

FIGURE 1.6 – High speed (drawing velocity $5\sigma/\tau$) tensile test : triaxial tensile test applied to a glassy specimen by using different methods, the mechanical responses are very different. Snapshots at a strain $\varepsilon_{yy} = 1.4$ show that homogenous deformation (right) results in an unphysical ductile behavior compared to the localized deformation when "grips" are used (left), which is more realistic.

1.3.3 Effect of deformation rate

In order to model as realistic tensile tests as possible, we have to ensure that the deformation velocity is small compared to the sound velocity. The typical sound velocity is here of the order of by $\sqrt{E'/\rho} \approx 10\,\sigma/\tau$ where E' is the principal modulus. If the velocity of the upper grip is small compared to this sound velocity, the imposed deformation will redistribute throughout the sample nearly "instantaneously", as the homogenous method does.

This condition might not be valid anymore for higher deformation rates. To illustrate this particular point, we plotted on figure 1.6 the response of the sample submitted to (i) boundary driven deformation and, (ii) homogenous deformation performed at a drawing velocity of $5\sigma/\tau$. It can be observed in this figure that the mechanical behavior of the sample is completely different depending on the solicitation method. All the deformation is indeed, localized near the upper grip for the boundary driven deformation method whereas it is homogeneously distributed with the homogenous method, which is, obviously unphysical. In the following, all results will be presented for the low deformation rate ($0.00223\ \sigma/\tau$), which is negligible compared to the speed of sound.

1.4 Results : tensile tests

The aim of this section is to compare the homogeneous and boundary driven deformation techniques presented in the previous section. Tensile tests are performed on 12 different cubic samples at two temperatures : $k_BT = 0.2\ \varepsilon$ (glassy state) and

$k_BT = 0.5\ \varepsilon$ (rubbery state) (see section 1.2). Stress-strain curves, as well as yield stress and associated strain, are investigated.

1.4.1 Uniaxial deformation

1.4.1.1 Glassy state

The uniaxial tensile test performed on a glassy polymer specimen typically proceeds in three stages : the stress rises to a maximum which for our system is located at a strain $\varepsilon_{yy} = 0.05$. In accordance with other previous studies it was found that the total deformation is completely recovered for $\varepsilon_{yy} \leqslant 0.02$ after removing the deformation or load constraint [2]. This value can be taken as the limit of the elastic region (at least at a mesoscopic scale, as local irreversibility is known to take place below this value [Yoshimoto 2004, Papakonstantopoulos 2008]). The deformation leaves some hysteresis when the sample is deformed beyond this value and relaxed.

From the elastic regime we extract a Young's modulus $E = 38.9 \pm 0.1\ \varepsilon/\sigma^3$ and a Poisson ratio $\nu = 0.36 \pm 0.02$, which are in good agreement with other works using the same flexible model [Schnell 2006].

The maximum is identified with a yield stress [Rottler 2003] at $\sigma_{yield} = 1.28 \pm 0.02\ \varepsilon/\sigma^3$ which marks the onset of plastic flow. The yield is followed by a smooth decrease of the stress (strain softening), until the stress becomes essentially constant, $\sigma_{flow} = 1.08 \pm 0.02\ \varepsilon/\sigma^3$.

The third part of the stress strain curve is the so called "strain hardening" regime [Lyulin 2005], associated with the debonding of the entanglement network [Hoy 2006]. This part of the curve can be modeled by the gaussian strain hardening expression as :

$$\sigma_{yy} = \sigma_{flow} + G_R g(\lambda) \tag{1.9}$$

G_R is the hardening modulus, $g(\lambda) = \lambda^2 - 1/\lambda$ and $\lambda = y_t/y_0$ is the elongation in y direction *(true strain* $\varepsilon_{yy} = \ln(\lambda)$*)*. The stress strain curves were plotted with ε_{yy} and $g(\lambda)$ in figure 1.7 show a nice fitting of the strain hardening regime to equation 1.9. However, as was extensively discussed in a recent work by Hoy and Robbins [Hoy 2008], the value of the hardening modulus G_R is much larger than the value that would be expected from an elastic model of the entanglement network at this temperature.

Figure 1.8 compares stress-strain curves resulting from homogeneous and boundary driven deformations techniques. In the glassy state ($k_BT = 0.2\ \varepsilon$), the two curves are completely superimposed. Despite removing the periodic boundaries in the direction of traction, the boundary driven deformation technique still captures the behavior of the polymer sample from the elastic to strain hardening domains. Mechanical properties such as, Young's Modulus, yield stress and strain evaluated

2. Recovery is performed by zeroing the spring forces F^u and F^l and relaxing the sample in the anisotropic NPT ensemble for the grip method. For homogenous method only relaxation in anisotropic NPT ensemble is required.

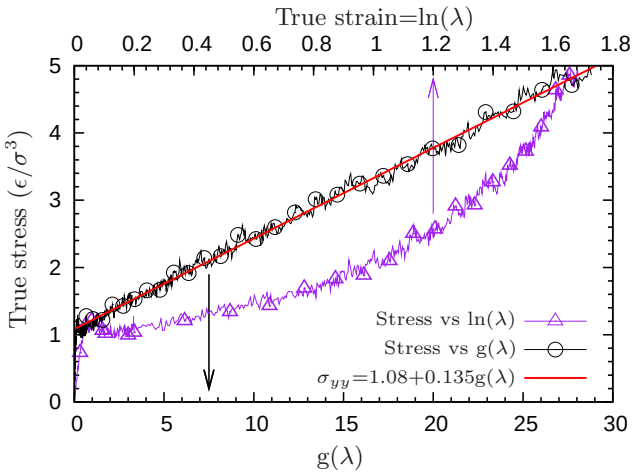

FIGURE 1.7 – Stress strain curves of uniaxial tensile test plotted versus true strain (upper axis) and $g(\lambda)$ (lower axis). The strain hardening regime is fitted linearly by the Gaussian expression (equation 1.9) of strain hardening $\sigma_{yy} = 1.08 + 0.1346g(\lambda)$

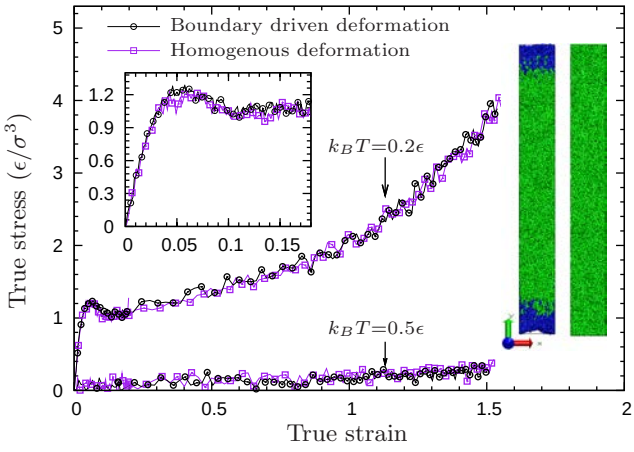

FIGURE 1.8 – Behavior curves of uniaxial tensile test glassy ($k_BT = 0.2\ \varepsilon$) and rubbery ($k_BT = 0.5\ \varepsilon$) specimen. A zoom of the yield region is shown in inset. No significant differences can be observed. The two snapshots correspond to a true strain of 1.5 at $k_BT = 0.2\ \varepsilon$.

from these curves are summarized in table 1.1, and show a good agreement between two methods in all samples tested.

1.4.1.2 Rubbery state

The same procedures were applied to perform uniaxial tensile tests in the rubbery region of our polymer model, at $k_BT = 0.5\ \varepsilon$. Compared to the glassy state, the rubbery state has a much weaker elastic response regime. This response can be fitted with a rubber modulus that is about two to three orders of magnitude below the glassy modulus, and a Poisson ratio very close to 1/2, as expected from a rubber. Strain recovery after a strain of 0.8 is about 0.18 .

As shown in figure 1.8 homogeneous and boundary driven deformation techniques lead to the same behavior. The test has then repeated on all specimens and again no significant differences were found.

It may seem surprising, that the boundary driven deformation technique and the homogeneous deformation technique give such similar results. In fact periodic boundary conditions were originally introduced in order to minimize boundary effects for thermodynamic properties. Here, our results show on the one hand that the possible shortcomings of homogeneous deformation (i.e. : an exaggerated deformation of the intramolecular bonds) can be ignored, and on the other hand that the boundary effects have negligible influences on the mechanical properties. This results is obtained with "grips" that have somewhat artificial properties, in the sense that they are allowed to deform freely in the same manner as the working zone in the direction transverse to the traction. In the following, we consider the more realistic case of a triaxial deformation, with grips that do not follow the deformation of the sample.

1.4.2 Triaxial deformation

1.4.2.1 Glassy state

Triaxial tensile tests were also performed using boundary driven and homogeneous deformation techniques. The stress strain curves obtained with each method, are plotted in figure 1.9, showing different regimes. As in uniaxial tensile tests, the stress first rises to $\sigma_{yield} = 4.2 \pm 0.08\ \varepsilon/\sigma^3$, the elastic modulus $E' = 80.35 \pm 1.3\ \varepsilon/\sigma^3$ is consistent with other previous works [Rottler 2001, Schnell 2006] and with the one predicted from the Young's modulus and Poisson ratio obtained in uniaxial tests, $E'_p = E(1+\nu)/((1-2\nu)(1-\nu)) = 83.5\ \varepsilon/\sigma^3$. At the yield point the polymer failure starts [Sixou 2007], voids nucleate and the stress becomes localized and carried by polymer "fibrils". After these fibrils or crazes are formed, the stress becomes essentially a constant drawing stress $\sigma_{drawing} = 0.95 \pm 0.05\ \varepsilon/\sigma^3$. The plastic flow proceeds at this constant stress value, with a progressive transformation of the bulk polymer into a fibril network connected by entanglements [Rottler 2001]. When the entire bulk is completely transformed into crazes, the stress would eventually rise again, as the chains align in the direction of traction [Kroger 1997].

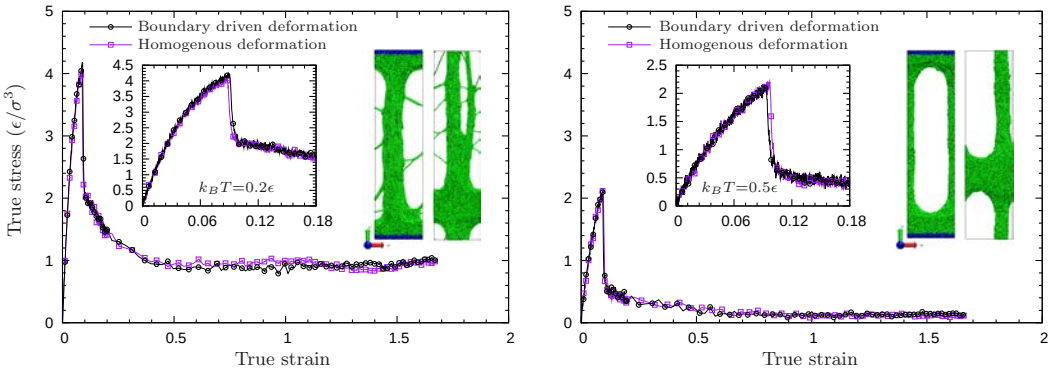

FIGURE 1.9 – Stress strain curves in a triaxial tensile test for a glassy sample ($k_BT = 0.2\ \varepsilon$) (left) and rubbery specimen ($k_BT = 0.5\ \varepsilon$) (right). The inset shows a zoom in the vicinity of yield. In both cases the agreement is remarkable between boundary driven and homogeneous deformation techniques.The snapshots correspond to a true strain of 1.5.

	Uniaxial (results are averaged over 6 tests)					
	$k_BT = 0.5\varepsilon$		$k_BT = 0.2\varepsilon$		$k_BT = 0.01\varepsilon$	
	Bound. dri.	*Homog. def.*	*Bound. dri.*	*Homog. def.*	*Bound. dri.*	*Homog. def.*
Yield stress (ε/σ^3)	–	–	1.33 ± 0.02	1.3 ± 0.03	1.8 ± 0.04	1.7 ± 0.03
Yield strain	–	–	0.06 ± 0.02	0.05 ± 0.01	0.06 ± 0.01	0.07 ± 0.02
Poisson ratio, ν	0.49 ± 0.01	0.48 ± 0.03	0.41 ± 0.01	0.4 ± 0.02	0.41 ± 0.01	0.38 ± 0.01
Young's modulus E (ε/σ^3)	0.19 ± 0.01	0.21 ± 0.01	39.1 ± 1.7	37.9 ± 1.7	49.1 ± 1.8	48.3 ± 1.5
Triaxial (results are averaged over 6 tests)						
Yield stress (ε/σ^3)	2.16 ± 0.03	2.14 ± 0.07	4.14 ± 0.08	4.15 ± 0.09	5.46 ± 0.01	5.40 ± 0.002
Yield strain	0.091 ± 0.005	0.091 ± 0.005	0.084 ± 0.005	0.086 ± 0.003	0.097 ± 0.001	0.094 ± 0.002
Elastic modulus, E' (ε/σ^3)	33.3 ± 2.2	32.4 ± 1.5	80 ± 1.3	79 ± 1.4	98.62 ± 0.5	97.15 ± 0.8
$E'_p = E(1-\nu)/((1-2\nu)(1+\nu))$	–	–	91 ± 11	80 ± 16	114 ± 14	98 ± 8

TABLE 1.1 – Some mechanical properties measured all stress-strain curves. Uncertainties represent the variations observed for six different samples. *Bound. dri.* : Boundary driven tests, *Homog. def.* : Homogenously deformed tests.

Stress strain curves resulting from each deformation method are nicely superposed as displayed in figure 1.9. Again the agreement is essentially perfect, and the craze development, as shown in the corresponding snapshots, proceeds in a very similar manner. The small differences at the yield point are of purely statistical origin, as they are smaller than the difference between two different samples tested with the same method, with different widening directions.

1.4.2.2 Rubbery state

The rubbery specimen behaves in a very similar manner as the glassy specimen. However, the high temperature favors yield at a lower stress $\sigma_{yield} = 2.15 \pm 0.03\ \varepsilon/\sigma^3$ and the drawing stress falls to $\sigma_{drawing} = 0.15 \pm 0.05\ \varepsilon/\sigma^3$. Despite the high temperature, the specimen exhibits the same behavior as the low temperature one. This is due to applied triaxial stress that prevents any relaxation of stress. Thus, failure start by crazing instead of shearing [Rottler 2001]. The two methods are compared in figure 1.9 (at right). Once again, a nice agreement is observed.

1.5 Conclusions

Table 1.1 summarizes the elastic and yield properties obtained in this work at various temperatures and solicitations, using the homogeneous deformation and the boundary driven methods. In the homogeneous deformation technique, a periodic sample is stretched by deforming the fully periodic simulation box size. In the boundary deformation technique, periodicity is partially cleared and molecular "grips" are introduced to deform the sample by moving its ends apart.

Our main conclusion is that the two techniques yield perfectly consistent results, and that the uniaxial and triaxial tests result in a consistent determination of linear elastic properties.

This similarity between homogeneous and boundary driven methods was not *a priori* expected. In general, boundary effects are important for thermodynamic and dynamic properties of small systems. Bulk properties can be obtained from simulations of such systems through the use of periodic boundary conditions. Our results show that the mechanical testing of glassy or rubbery polymer is not affected by the presence of rigid (in triaxial tests) or "soft" (uniaxial case) grips. Both the elastic and plastic responses are equivalent. The similarity of the plastic response also indicates that the artificial aspect of the homogeneous deformation methods, in which intramolecular bonds are deformed affinely at each step, does not introduce any statistical artefact in the activated events that constitute the plastic flow.

Finite element modeling of complex materials is based on the notion of elementary representative volumes, with local mechanical properties that can be described by stress strain curves determined at the macroscopic level. Our results show that this notion of elementary representative volume can in fact be applied to extremely small systems. Here the glassy polymer constrained between the molecular "grips" behaves exactly in the same way as the "bulk" polymer represented by a sample

with periodic boundary conditions, and could therefore be modeled using the same constitutive equation.

Finally, we conclude that the use of non periodic boundary conditions could be advantageous for the simulation of complex heterogeneous samples. For example, simulating an ABC triblock copolymer in its lamellar phase requires 4 lamellae ($ABCB$ stacking) if periodic boundary conditions are used, while an ABC stack is sufficient in the boundary driven case.

Chapitre 2

Primitive path analysis

Contents

2.1 Introduction

Topological constraints called entanglements are a determining factor in polymer dynamics in both equilibrium and non equilibrium situations. Entanglement results from the overlap between polymer molecules with high molecular weight. Since polymer chains are unable to pass trough each other, entanglements restrict individual chain motions to a curvilinear, tubelike region enclosing each chain. In this context Doi and Edwards [Doi 1986] define the Primitive Path (PP) as the shortest path between the endpoints of the original chain into which its contour can be contracted without crossing any obstacle.

Various algorithms have been developed in order to explicit the primitive paths of coarse grained polymer chains and to identify the entanglement length. The aim of these algorithms is to reduce the polymer chains simultaneously to their primitive paths by minimizing the bond energy [Sukumaran 2005] or the contour length [Kroger 2005, Tzoumanekas 2006] of chains with frozen ends. An analytical expression for the PP of random walks with randomly positioned entanglements has also been recently proposed by Khaliullin and Schieber [Khaliullin 2008].

The entanglement length is an important ingredient for evaluating some rheological properties such as the strain hardening modulus [Hoy 2006] and plateau modulus [Kremer 2005]. Under tensile strain conditions, entanglements behave as physical cross-links that strengthen the mechanical properties of polymer [Riggleman 2009]. But, it is not yet clear how these entanglements evolve under deformation, especially in the uniaxial tensile strain where the strain hardening is expected to depend on the entanglement state.

In this chapter, we present direct observations of the effect of tensile strain on the entanglement network of a glassy polymer model. An energetic version of the

primitive path algorithm was used in deformed polymer samples. In section A.2, we present the model and the tensile conditions, section 2.3 details the method to extract the entanglement length. The results are discussed in the last section.

2.2 Model and Method

The samples that are used in this chapter were provided by the tensile tests performed in chapter 1. Only glassy samples deformed by the homogenous method (uniaxial and triaxial) are considered here. The deformed configuration has been regularly extracted along the deformation trajectory. The storage frequency was chosen to be higher in the elastic part of the constitutive law to better describe this relatively short stage.

2.2.1 Identification method

In order to reduce our polymeric configurations to their primitive paths, the Primitive Path Algorithm (PPA) is performed as in ref [Sukumaran 2005]. The procedure is nearly identical to that of ref [Hoy 2005]. All chain ends are frozen in the space. The bonded interaction FENE potential is switched to a harmonic potential with a higher stiffness.

$$U_{Harm}(r) = -0.5K_{har}(r - r_0)^2 \tag{2.1}$$

$K_{har} = 500\varepsilon$ is the bond stiffness, r_0 is the bond length at equilibrium state. The intra-chain LJ interactions are disabled, while the inter-chain interactions are maintained to prevent chains from crossing each other. The system temperature is reduced to a very low value $k_BT = 0.001\varepsilon$ in order to damp the thermal fluctuations or any parasite vibrations resulting from the changes in FENE bond properties. The equation of motion is integrated and the equilibrium bond length r_0 is continuously shifted to zero (figure 2.1.a).

As a consequence, the polymeric chains minimize their lengths between their fixed ends as the "covalent" bonds contract homogeneously. After the convergence of the procedure (The convergence criterion described in the next section), the resulting chains are tautened between their ends. If no other chains intercept the trajectory, the chain are straight linear between their two frozen ends (first row of figure 2.2).

With this protocol, intra-chain knots are eliminated. Intra-chains knots can be conserved by keeping the intra-chain LJ potential active. As the bonds reduce their equilibrium lengths in the PPA, the intra-chain LJ minimum has to be reduced to a value close to the r_0 minimum but slightly superior (see figure 2.1).

This version of PPA was applied to a single artificial chain forming a conventional "overhand knot". On second row of figure 2.2, it can be observed that the intra-chain knot is retained even after the convergence of the PPA. Sukumaran [Sukumaran 2005] and Hoy [Hoy 2005] have demonstrated that the number of "self entanglements" is negligible for the systems considered here. Therefore, only the first version is used for PPA in the rest of this chapter.

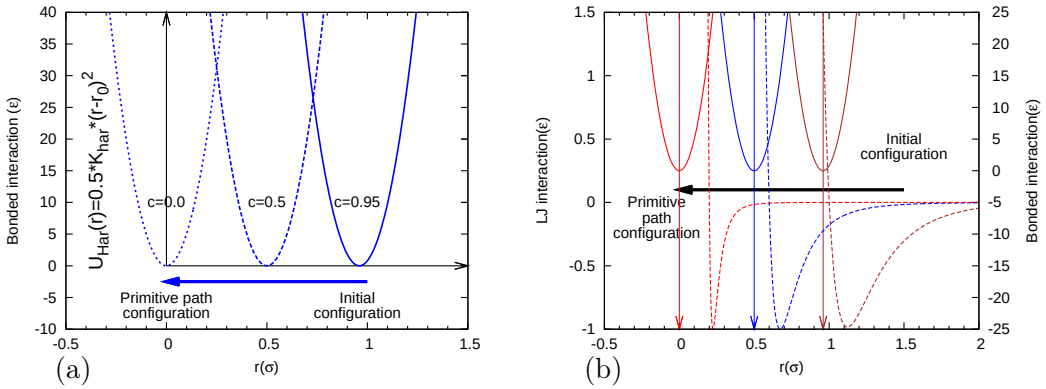

FIGURE 2.1 – (a) Harmonic potential applied to describe the bonded interaction in the PPA (first version : used in the present work). As the bond length decreases continuously, polymer chains will be pulled taut between two ends. (b) Harmonic and LJ potentials applied simultaneously to describe the bonded and non-bonded **intra-chain** interactions in PPA (alternative second version : not used in the present work). The difference between the energy minima prevents the chain self-crossing.

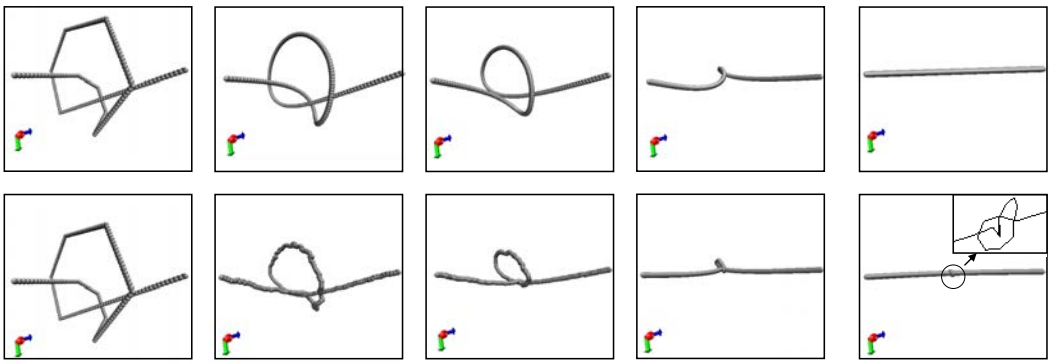

FIGURE 2.2 – PPA applied to a single chain forming a conventional "overhand knot". The top row shows the evolution of the configuration in which any knot involving a single chain is forbidden (first version of the algorithm). The formation of intra-chain knot is allowed with the second PPA, as it shown in the bottom row.

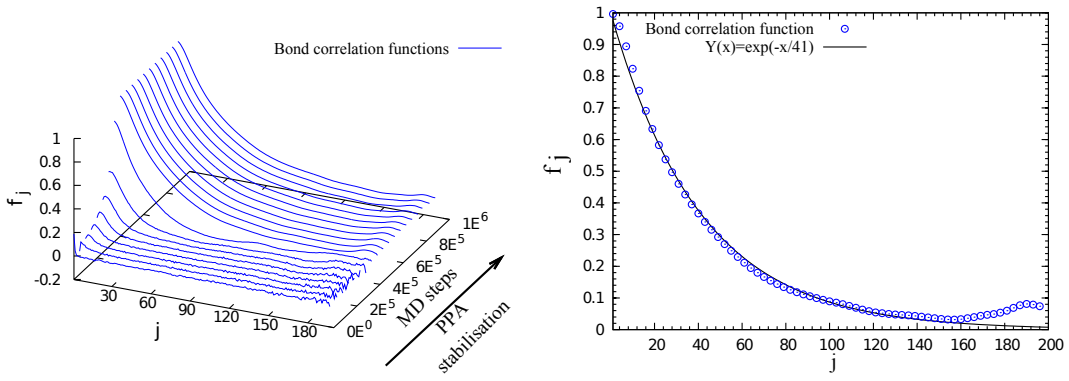

(a) (b)

FIGURE 2.3 – (a) Bond autocorrelation function for an equilibrated polymer sample subjected to PP algorithm. (b) Bond auto correlation function after the PPA.

2.2.2 Entanglement length

The most commonly used method [Hoy 2005] for evaluating the entanglement length N_e after PPA is given by the following equation :

$$N_e = \frac{\langle R_{ee}^2 \rangle}{(M-1)\langle b_{pp} \rangle^2} \tag{2.2}$$

R_{ee} is the end to end distance, M in the molar mass, b_{pp} is the bond length after PPA. $(M-1)\langle b_{pp} \rangle^2$ is the mean square contour length of chains. This equation is valid only if the primitive path strand is a Gaussian random walk. This assumption cannot be retained when chains become out of equilibrium (as in the tensile test, and for lamellar copolymers).

An alternative method is used to quantify the entanglement length from the chains conformations. The bond autocorrelation function was employed to get the entanglement length. In bulk polymeric systems, this function is usually used to evaluate the persistence length of infinite chain, as it done below :

$$L_p = \frac{1}{b_0} \left\langle \sum_{j>i}^{M} \mathbf{b_i} \cdot \mathbf{b_{i+j}} \right\rangle = \frac{1}{M b_0} \sum_{i=0}^{M} \sum_{j>i}^{M} \mathbf{b_i} \cdot \mathbf{b_{i+j}} \tag{2.3}$$

Where $\mathbf{b_i}$ is the bond vector order i, b_0 is the mean bond length $b_0 = \langle b_i \rangle$, and M is the molar mass (200 in our case). The normalized Bond Autocorrelation Function (BACF) f_j is given by the following equation :

$$f_j = \frac{\langle \mathbf{b_i} \cdot \mathbf{b_{i+j}} \rangle}{b_0^2} \tag{2.4}$$

The evolution of f_j for a configuration under PPA is plotted in figure 2.3.a. As the PPA is progressing, the evolution of the BACF exhibits a threshold at $N_{MD} = 5 \times 10^5$ MD steps, whereafter the curves remain stable. This behavior illustrates

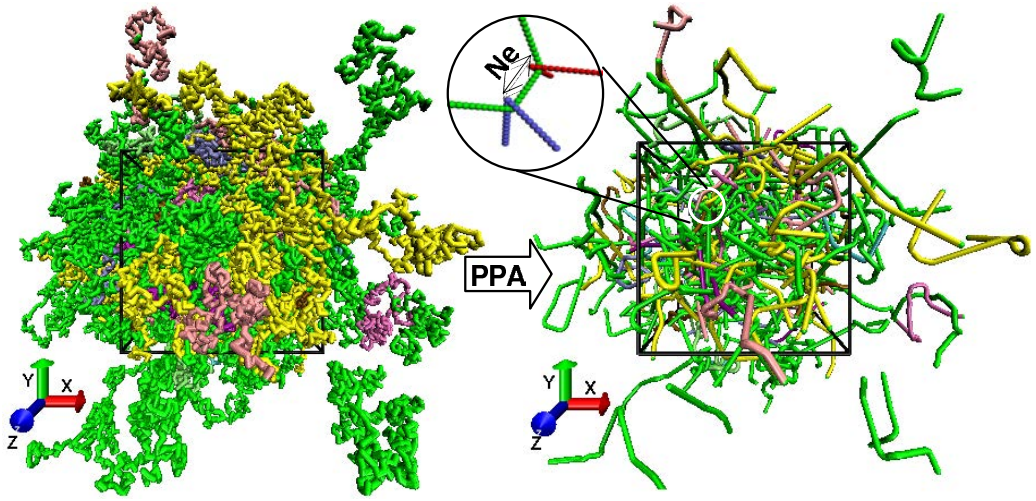

FIGURE 2.4 – Snapshot of polymer chains before and after PPA.

the convergence of the chain shapes to their primitive paths (shown in figure 2.4). Figure 4.b shows the BACF after PPA of the initial undeformed configuration. This function can be accurately fitted by the following exponential function :

$$Y(x) = \exp(-x/\tau) \tag{2.5}$$

Where τ is the fit parameter.

From equations 2.3 and 2.4 one can deduce :

$$L_p = b_0 \times \sum_j f_j \tag{2.6}$$

by using the exponential function of equation 2.5, L_p can be expressed as :

$$L_p = b_0 \int_0^M Y(x)dx = b_0 \int_0^M \exp(-x/\tau)dx \approx \tau b_0 \tag{2.7}$$

In the case of Gaussian primitive path chain with random walks :

$$N_e = L_k = 2L_p - b_0 = b_0(2\tau - 1) \tag{2.8}$$

L_k is the Kuhn length that defines the path length of the random walk (entanglement length in PP configuration). The resulting value of τ that emerges from figure 2.3.b is 41. The corresponding entanglement length is 76.8, thus the PP is broken into 3 to 4 independent strands which is consistent with other works [Sukumaran 2005, Hoy 2005, Schnell 2006].

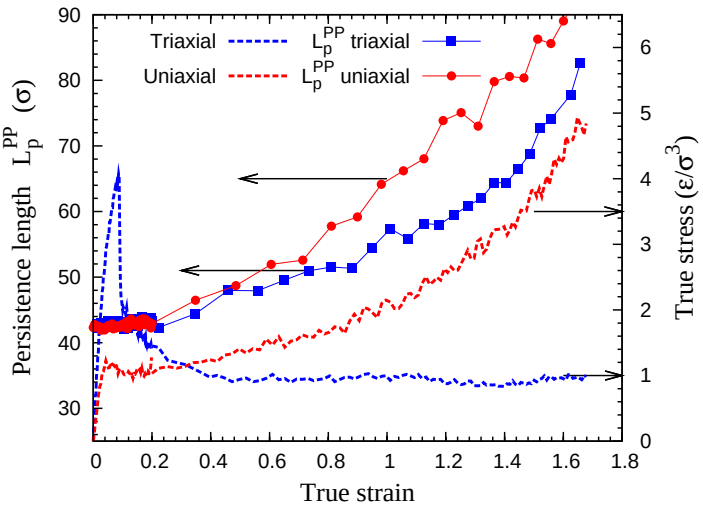

FIGURE 2.5 – Stress (dashed lines) and primitive path persistence length (points) evolutions for a glassy polymer submitted to uniaxial and triaxial load. Chain disentanglement is more pronounced in uniaxial loading where chains tend to align in the loading direction.

2.3 Evolution of entanglement length in tensile strain tests

The mechanical behavior of entangled polymers has been extensively described in previous works (see for example [Schnell 2006, Rottler 2003, Foteinopoulou 2006, Makke 2009]). In uniaxial tensile load (dashed red curve in figure 2.5) three main regimes can be distinguished for our systems : elastic, yielding and strain hardening regimes.

The elastic regime was usually correlated to small shifts of beads from their equilibrium low energy positions.

The yield point limits the linear viscoelastic regime at strain of $\varepsilon_{yy} = 0.05$, where the plastic flow begins. The third part of the stress-strain curve is the strain hardening regime, where the stress rises again with strain. This trend is due to the forced orientation in the conformation of chains and the rate of plastic rearrangements [Hoy 2006, Hoy 2008].

As in uniaxial condition, triaxial loading leads to distinct regimes (dashed blue curve in figure 2.5). The stress first rises to $\sigma_{yy} = 4.2\ \varepsilon/\sigma^3$ where voids nucleate. After cavitation, the stress drops to $\sigma_{yy} = 0.95\ \varepsilon/\sigma^3$, since a part of the stored elastic energy will be converted to a free surface energy of the cavity surface. The stress remains constant in the drawing regime, where the polymer bulk becomes progressively a fibril network.

The evolution of entanglement length (N_e) was measured indirectly by the persistence length (L_p^{PP}) calculated via the equation 2.7 for the primitive path configuration of deformed samples. Figure 2.5 shows the evolution $\langle L_p^{PP} \rangle$ plotted against

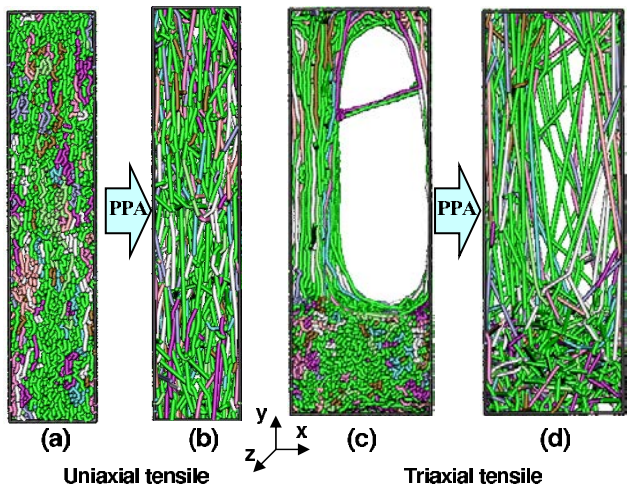

FIGURE 2.6 – Visualization of deformed samples and their corresponding primitive path at strain $\varepsilon_{yy} = 1$. Snapshots of uniaxial (triaxial) tensile is showing at left (right).

the stress-strain curve for both uniaxial and triaxial conditions. The entanglement density is fairly constant at low strain (elastic regime and strain softening). Chain disentanglement becomes significant in strain hardening (uniaxial) or in drawing regime (triaxial). In the following these evolutions will be discussed.

In uniaxial tensile conditions, the entire sample undergoes homogeneous deformation. The new chain conformation is subjected to the plastic flow that promotes the inter-chain sliding events and then disentanglement.

In our simulations, as in experiments, the strain hardening regime is well fitted by the Gaussian strain hardening equation :

$$\sigma_{yy} = \sigma_{flow} + G_R g(\lambda) \tag{2.9}$$

G_R is the hardening modulus, $g(\lambda) = \lambda^2 - 1/\lambda$ and $\lambda = y_t/y_0$ is the elongation in the tensile direction. The fitted values are $\sigma_{flow} = 1.08$ and $G_R = 0.13$ (see chapter 1, figure 1.7).

This equation has been, for a long time, interpreted as resulting from an entropic network model. The glassy polymer is then treated as a cross-linked rubber, the number of monomers between cross-links being equal to the entanglement length N_e.

Despite the success of this Gaussian model in describing experimental and simulation data, there are serious difficulties and inconsistencies with its theoretical motivation. The functional form arises from an entropic network model and reflects the entropic free energy penalty from stretching the network. While such arguments are well justified for rubbery polymer melts, it is not clear how polymer chains in the glassy state can sample configurations sufficiently fast for entropy to contribute significantly to the overall stress [Rottler 2009]. In entropic models, the hardening

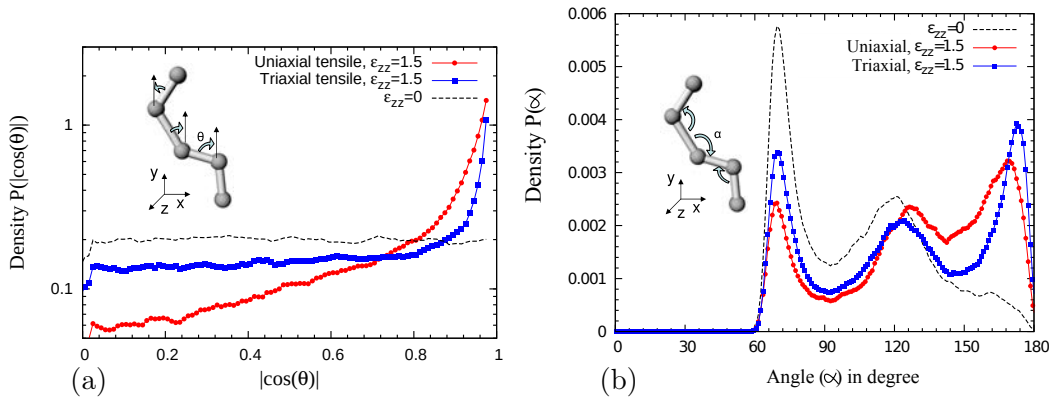

FIGURE 2.7 – (a) shows the distribution of angles between bonds and tensile direction y while the right plot (b) shows the distribution of angles between two subsequent bonds. Both plots were taken at strain $\varepsilon_{yy} = 1.5$

modulus G_R is predicted to vary linearly with temperature and entanglement density ρ_e and $G_R = \rho_e k_B T$.

In contrast to this prediction, the fitted value of the strain hardening modulus G_R seems to be constant, while the entanglement density decreases progressively in the strain hardening regime.

An interpretation of this behavior was provided by Hoy and Robbins [Hoy 2007, Hoy 2008] who demonstrated that the strain hardening, at low strain, is directly related to the rate of plastic rearrangements (breaking and reformation of non specific bonds). This process allows one to interpret also the strain hardening behavior observed in unentangled glassy polymeric systems (where the chain length is less than the entanglement length). A similar interpretation was given by Vorselaars *et al* [Vorselaars 2009], who highlight a rise in the rate of nonaffine monomer displacements in the strain hardening regime of an atomistic model of glassy polycarbonate .

The role of the entanglement in strain hardening process becomes relevant only at relatively high strain, when the chains become well tautened between the entanglements and the strong bonds (FENE) are stretched [Hoy 2008].

Figure 2.7.a shows the orientation of bonds with respect to the tensile direction y for deformed polymer samples at ($\varepsilon_{yy} = 1.5$). The major part of bond orientations is located at low angles.

Furthermore, the distribution of angles between subsequent bonds is also plotted in figure 2.7.b. Before deformation, two peaks are distinguished at angles 70° and 120°. These preferential angles arise from the geometrical restrictions imposed by the inter-atomic potential (bond length and radius of the excluded volume). In the deformed configuration, a third peak rises at the vicinity of 175°, as the chains converge to a straight conformation. Both plots in figure 2.7 show the change of chain conformation, that increases the rate of disentanglement under tensile strain

conditions.

In triaxial tensile tests, the applied deformation becomes localized after cavitation. As the deformation increases, the polymer bulk will be progressively converted into a "fibril" at constant stress. Strain hardening is not observed in this regime while entangled bulk material remains between the "fibril". As it described by figure2.6.c only chains that form fibrils are preferentially oriented in the tensile direction. The rest of the chains conserves bulk random walk conformations. The increase in the average entanglement length results from the progressive conversion of the material from bulk to oriented fibrils.

Figure 2.6.d shows long segments of primitive path in the fibril zone. Therefore, the chain disentanglement is also localized and it seems to be in correlation with the development of crazing. (figure 2.5). The chain disentanglement is more pronounced in uniaxial conditions compared to triaxial ones. This behavior is expected because in the uniaxial conditions, the tensile strain is homogeneously distributed in the sample, which is not the case for triaxial tests, where the deformation is localized in the crazes after cavitation.

2.4 Conclusion

Primitive path analysis were carried out for a glassy polymer system under tensile strain conditions. Bond autocorrelation function is used to evaluate the entanglement length of the primitive path configurations. Two different loading conditions were considered : uniaxial and triaxial. There is no relevant change of entanglement length in the elastic regime in both tests.

In uniaxial tensile test, chain disentanglement occurs in parallel with the growth of stress in the strain hardening regime. In contrast to entropic network model, the results reveals that the strain hardening slope is not affected by the increase of entanglement length. This behavior was interpreted by the fact that the strain hardening, at small strain, results fundamentally from the increase in plastic deformation with strain and is not directly related to the entanglement density ρ_e, as described by Hoy and Robbins.

The evolution of chain conformations under tensile strain was inspected. In uniaxial tensile conditions the chains become oriented in the tensile direction. The reorientation of the chains is accompanied by chain sliding that favors an increase in the entanglement length.

In the triaxial tensile test, the increase of entanglement length is strongly related to the formation of fibrils after cavitation. In the drawing regime, we find that large entanglement lengths are localized in the fibrils, where the chains are more oriented in the tensile direction. However the progressive increase of the entanglement length can not be assigned to the disentanglement of the fibril but instead to the continuous change of chain configuration from the bulk Gaussian configuration to directed crazes.

Chapitre 3

Cavitation in amorphous polymers

Contents

This chapter essentially reproduces the manuscript "Predictors of cavitation in glassy polymers under tensile strain : a coarse grained molecular dynamics investigation" realized in collaboration with prof. Jörg Rottler and submitted to "Macromolecular theory and simulation".

3.1 Introduction

Under hydrostatic stress conditions, failure of amorphous polymers occurs through cavitation, often followed by crazing, *i.e.* the formation of interpenetrating micro-voids [Perez 1998]. Similarly, the plastic deformation of semi-crystalline polymers is strongly correlated to the nucleation of cavities in the amorphous region [Humbert 2010]. Although essential to control deformation and failure of many organic materials, cavitation in glassy polymers under load is poorly understood. To our knowledge, the microstructural causes, or the precursors of cavitation at a microscopic scale, are not clearly identified. Although it is known that impurities or surface defects aid the nucleation of cavities [Herrmann 2002, Argon 1977], it is presently not possible to predict where cavitation will take place in the polymer.

Classical nucleation theory, where elastic energy is balanced by the creation of free surface, was used by Argon to model the cavitation nucleation [Argon 1977]. Estevez *et al.* investigated the fracture toughness in glassy polymers using mechanical approaches with empirical constitutive equations to describe the competition between shear yielding and crazing [Estevez 2000]. They noted that the development of crazes is favored by a fast local deformation.

According to Gent [Gent 1970], crazing in glassy plastics can be attributed to a local stress-activated devitrification. It is generally agreed that large triaxial tensile stresses are needed to induce cavitation, which forms the basis of several macroscopic craze initiation and cavitation criteria [Sternstein 1969, Bowden 1973]. Molecular dynamics simulations of polymer glasses also found a transition from shear yielding, which obeys a pressure-modified von Mises yield criterion [Rottler 2001], to cavitation as the hydrostatic pressure becomes negative, but have not yet investigated the connection between cavitation and local microstructural configuration. More recent simulations explored correlations between the location of failure, higher mobility regions and a higher chain ends density [Sixou 2007] acting then as local defects, or a local, stress-induced disentanglement of chains [Mahajan 2010]. In the latter work a primitive path algorithm was used to monitor the entanglement network in a sample undergoing triaxial deformation, and it was found that regions undergoing crazing were also depleted in terms of entanglements.

The local mechanical properties are a determining factor to understand the response of systems under strain. Yoshimoto et al. [Yoshimoto 2005, Yoshimoto 2004] have calculated the local elastic modulus in a coarse grained polymer glass using a thermodynamic approach based on stress fluctuation . They found that polymers are mechanically heterogenous at local scale. Papakostantopoulos et al. [Papakonstantopoulos 2008] have studied the earliest local plastic events observed in the elastic regime of polymer glass. They found that these irreversible events take place in domains that exhibit a low positive elastic modulus. Analogous results were obtained by Tsamados et al. on Lennard-Jones glasses submitted to a quasistatic shear strain[Tsamados 2009]. They found a correlation between high nonaffine displacements and local low elastic modulus.

It is unclear, however, if these criteria can be used in a predictive manner, in the sense that the cavitation event could be predicted from the configuration of an unstrained system.

In this paper, we will therefore investigate the correlation between the microstructure of a homopolymer at the segmental level and the nucleation of cavities, in an attempt to find a microstructural *predictor* of such events. Section 3.2 will present the methodology and will demonstrate that the non-affine particle displacement (NAD) is a particularly suitable tool for characterizing and locating cavities. Section 3.3 will be devoted to the investigation of possible causes of cavitation, namely (i) local excess of free volume, (ii) local excess of atomic stress, (iii) local density of beads and chain ends, and (iv) local bulk modulus. We will show that while (i)-(iii) bear little correlation to the NAD, the local bulk modulus (iv) has a much better potential to predict the cavitation event.

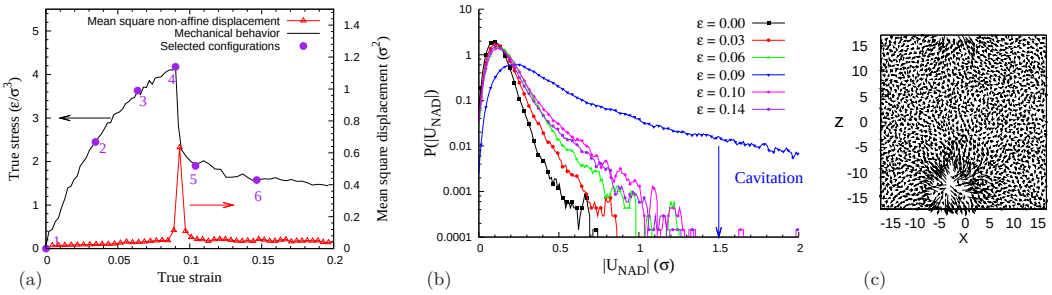

FIGURE 3.1 – (a) Stress-strain curve of a glassy polymer at $T = 0.2$ during a triaxial tensile test. A peak in the mean square non-affine displacement is observed simultaneously with the drop of the stress due to cavitation. Markers 1, 2, 3 and 4 indicate the selected configurations for which distributions of NAD are plotted in (b). These distributions show an exponential tail for configuration 4, due to the large amplitude motions caused by cavitation. (c) Representation of the NAD in a cross-section of the sample containing the cavity, for configuration 4.

3.2 Methods

3.2.1 Molecular dynamics simulations

Molecular dynamics (MD) simulations were carried out for a well established coarse-grained model, in which the polymer is treated as a linear chain of N beads of mass m, which we refer to as monomers, connected by stiff anharmonic springs that prevent chain crossing and breaking [Kremer 1990]. The beads interact through a conventional 6-12 Lennard-Jones potential that is truncated at 2.5 times the particle diameter (The tiny discontinuity of the force at the cutoff distance, less than 1% of the maximal attractive part, has no consequence). All quantities will be reported in units of the Lennard-Jones length scale σ and energy scale ε, and the characteristic time is $\tau_{LJ} = \sqrt{m\sigma^2/\varepsilon}$. Newton's equations of motion are integrated with the velocity Verlet method and a time step $\Delta t = 0.006$. Periodic simulation cells of initial size $L_x(0) = L_y(0) = L_z(0) = 34.2$ containing $M = 215$ chains of size $N = 200$ beads were used with a Nosé-Hoover thermostat, *i.e.* in the NVT ensemble. All samples were generated using the "radical-like" polymerization method [Perez 2008]. The polymerization starts from a Lennard-Jones liquid, where 215 beads are chosen randomly to behave as "radical" sites. Each radical bead is allowed to connect to a free and nearest neighbor with a strong covalent bond. The radical sites are then transferred to the new connected beads, allowing thus the growth of all chains. If no monomers are near the radical, no FENE bond is created. Another attempt will be performed at the next growth stage. Between two growth stages, the entire system is relaxed during 100 MD steps. The polymerization propagates until all chains reach their target length of 200 beads. When the generation is terminated, residual single beads are removed and the system is relaxed for 10^7 MD steps in NPT ensemble at $T = 1$ and $P = 0$ to reach an equilibrium state. The equilibration

leads to a "mean square internal distance" very close to the function given by Auhl et al. [Auhl 2003]. The polymer is then rapidly quenched into the glassy state at a temperature $T = 0.2$ in NPT ensemble (cooling rate : 1ε per 10^6 MD steps). The glass transition temperature is $T_g = 0.43$ [1]. The pressure remains zero and the sample density reaches 1.04 before applying the deformation.

Triaxial tensile test conditions were employed [Makke 2009]. The samples were subjected to a sequence of deformation-relaxation steps, composed of (i) a rescaling of the simulation box in the tensile direction (y in our case so that the true strain $\varepsilon_{yy}(t) = \ln(L_y(t)/L_y(0))$, whereas the two other dimensions remain unchanged, followed by (ii) an MD step in the NVT ensemble. The deformation rate was chosen to be $\dot{L}_y = 0.0025$, so that the initial strain rate is $\dot{\varepsilon}_{yy}(0) = 7.3 \times 10^{-5}$. Over the range of strain investigated, the true strain rate remains essentially constant. Note that the applied deformation trajectory leads to a high level of triaxiality, which is the basic ingredient for cavitation. As the deformation proceeds, configurations were recorded along the trajectory in order to analyze their microstructure.

3.2.2 Non-affine displacement : a tool for characterizing cavitation

The mechanical behavior of our glassy polymers under triaxial tensile conditions is illustrated in Figure 3.1(a). Three main regimes can be distinguished : (i) elastic, (ii) viscoelastic, and (ii) drawing regime, which occurs at constant stress. In the elastic regime, the increase of deformation will slightly shift the bead positions from their local energy minima, resulting in reversible behavior. This regime is limited to a very low strain 0.001 as demonstrated by Schnell [Schnell 2006]. In the viscoelastic regime, stress is relaxed by inter-chain sliding. This stage is limited by a strong drop of stress. When a critical deformation is reached, cavities will nucleate and then part of the stored elastic energy is released as free surfaces open up. Note that the strain hardening regime is not shown in Figure 3.1(a), since it occurs at larger strains when the entanglement network of chains and fibrils becomes stretched [Rottler 2001].

The detection of cavity nucleation could be performed visually on snapshots that are regularly stored during the course of the tensile test. However, small cavities in a three dimensional sample can be delicate to observe. Therefore, a more versatile indicator is needed. The non-affine displacement (NAD) is the perfect candidate for such observation and has been successfully used to monitor local plastic activity in 2D amorphous Lennard-Jones packings under athermal quasistatic deformation [Tsamados 2010]. Note that NAD fluctuations can not find their origin in the thermal motion of atoms since, in the framework of this paper, specimens are maintained well below their glass transition temperature ($T = 0.2 < T_g = 0.43$). Moreover, the NAD can be used as a routine tool and it starts to increase locally, in the early stages of cavity nucleation, even before the cavity could be observed visually on a snapshot of the sample.

The non-affine displacement ($\mathbf{u}^i_{na}$) is defined as the difference between the mean

1. T_g has been determined by the slope change observed when the sample volume is plotted with respect to the temperature during cooling from $T = 1$ to $T = 0.0001$ under the NPT ensemble

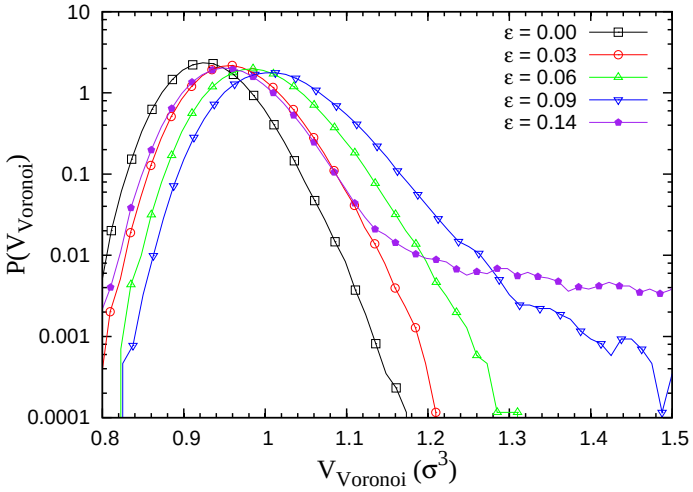

FIGURE 3.2 – Voronoi volume distributions of configurations extracted over the deformation trajectory. Cavitation can be clearly seen in the tail of distribution. After cavitation, the distribution reverts to a narrower shape.

displacement of a bead i during time δt ($\mathbf{r}^i(t+\delta t)-\mathbf{r}^i(t)$), and the mean displacement it would experience if the deformation were perfectly affine, *i.e* homogeneous at all scales,

$$\mathbf{u}^i_{na}(t) = \mathbf{r}^i(t+\delta t) - \mathbf{r}^i(t) - \dot{\varepsilon}_{yy}(t)\delta t \; r^i_y(t)\mathbf{e}_y, \tag{3.1}$$

where $\mathbf{r}^i(t)$ is the position of bead i at time t, $r^i_y(t)$ is the projection of this position along along the y axis and δt is the time elapsed between two configurations where the NAD is evaluated (typically 30τ).

In Figure 3.1(a), the cavity nucleates at $\varepsilon_{yy} = 0.09$. At the same strain, the NAD exhibits a peak. Beads that exhibit the largest NAD are those which belong to the surface of the cavity (see Figure 3.1(c)). Figure 3.1(b) shows the evolution of the NAD distribution for several deformations. Before cavitation, increasing the deformation shifts the distribution tail to larger NAD until the very moment at which the growth of a cavity occurs, which is associated with very large values of NAD (see Figure 3.1(c)). A threshold for NAD magnitude has been defined : if $|\mathbf{u}^i_{na}| > 1.5\sigma$ at the yielding point, the bead i is said to belong to the cavity surface. This threshold is used to identify the "cavity beads" in order to follow some of their local properties. The position of the cavity is defined as the centre of mass of these "cavity beads". After cavitation, the distribution returns to a narrower shape. Note that the NAD distribution broadens even before the stress drop in the stress-strain curve, due to the nucleation of the cavity. In the following sections, NAD will be used as a quantitative tool for investigating the possible correlations with other microstructural or mechanical properties, such as Voronoi volume, hydrostatic stress, local density and local moduli.

3.3 Microstructural causes and precursors of cavitation

In this section, we will attempt to correlate NAD fluctuations with some local properties measured at the scale of a single "atom" (Voronoi volume and stress per atom), and properties averaged on the scale of a few particle diameters (chain end density and bulk modulus).

3.3.1 Voronoï volume fluctuations

The concept of free volume has been extensively used to explain many specific properties of supercooled liquids and glasses. Free volume is defined as the volume in excess compared to an ideal disordered atomic configuration of maximum density. One of the simplest way to compute free volume on a local scale (and to avoid the ambiguity of the above definition) is the Voronoi tessellation, which uniquely assigns a polygonal volume to each bead, formed by intersecting the planes bisecting the lines between different bead centres. In order to determine whether local fluctuations of free volume (or Voronoi volume) favour the nucleation of a cavity, we used the voro++ routine to calculate the volume associated to each bead [2].

Voronoi volume and deformation level. Figure 3.2 shows the effect of the deformation on the Voronoi volume distribution. Increasing the deformation will increase almost homogeneously the free volume until cavitation takes place. During and after cavitation, the Voronoi volume distribution exhibits a significant tail representing the beads belonging to cavity walls. Note that after cavitation, the distribution relaxes to a narrower shape. Therefore, the cavitation process can be seen as an event, which *localizes* or *precipitates* the excess of free volume introduced by deformation.

Voronoi volume and beads functionality. Figure 3.3 compares the mean Voronoi volume evolution of both regular beads and chain ends. It can be seen that chain ends exhibit a larger Voronoi volume, which is not surprising since, by construction, covalent and Lennard-Jones bonds have their energy minimum at 0.9σ and 1.12σ, respectively. Note that when cavitation occurs, the mean Voronoi volume of chain ends becomes very noisy due to statistical limitations. The insets of Figure 3.3 show that the Voronoi volume distributions have a Gaussian shape, which shows the presence of low Voronoi volumes (much lower than the volume of an ideal disordered configuration). This calls into question the very concept of free volume, which is defined as that part of the atomic volume that can be redistributed throughout the system without change in energy [Turnbull 1961, Turnbull 1970], *i.e.* the volume of an ideal disordered configuration. These points of extremely low volume could be related to the *constriction points* introduced by Stachurski [Stachurski 2003] and,

2. See `http://math.lbl.gov/voro++/` and ref. [Rycroft 2006], where a very early version of this code was used.

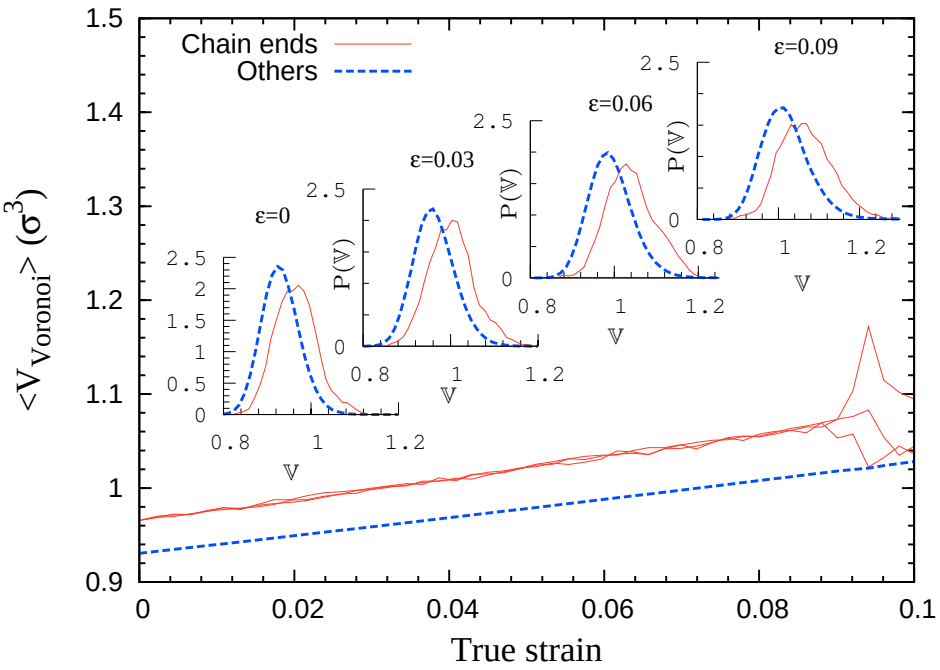

FIGURE 3.3 – Evolution of the mean Voronoi volume of chain ends and other beads. Inset : Voronoi volume distributions during the course of deformation. No correlation can be observed between chain ends and Voronoi volume variation during tensile test.

to a larger extent, to the *quasi-point defects* of Perez [Perez 1998], which represent points of high fluctuation of free energy.

Voronoi volume and non-affine displacement. Within the free volume approach, deformation induced relaxations are supposed to be correlated with the available free volume. Zones of larger free volume will therefore deform, changing the potential energy landscape and providing more free volume to zones of initially larger free volume. This explanation is often proposed to describe the formation of mechanical instabilities such as cavitation or shear bands. Motivated by these ideas, the search for a relationship between the magnitude of the NAD and the Voronoi volume becomes relevant.

Figure 3.4 shows a scatter plot obtained during deformation, where the magnitude of the NAD and the Voronoi volume were taken as variables. This scatter plot does not show a clear tendency for a correlation between NAD and Voronoi volume. Free volume represents the potential space for motion but it can not be seen as being a causal factor of the NAD and cavitation. The "cavity cluster" beads are also shown in this plot. In both cases, the points are distributed randomly and no noticeable trend was found, except during cavitation, where these beads exhibit larger NAD and slightly larger Voronoi volume. This analysis (not shown in this paper) was performed for several other temperatures ($T = 0.01$ and $T = 0.1$) and no correlation was found under these conditions either. Note that before cavitation,

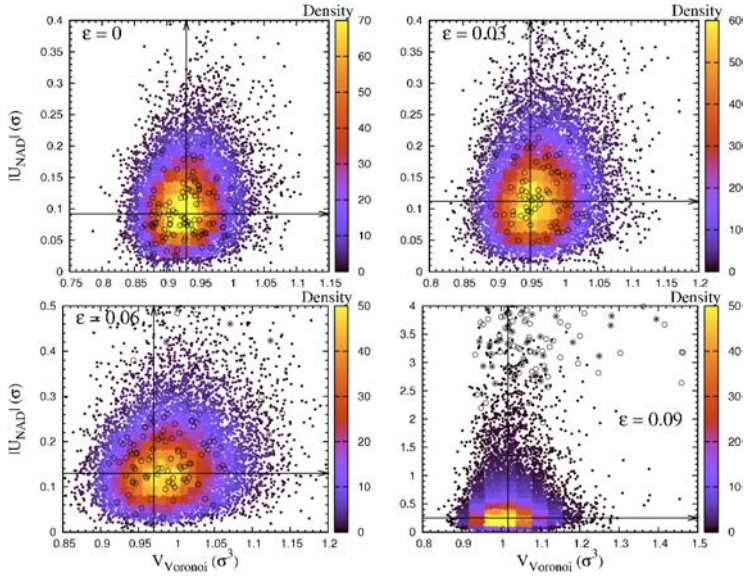

FIGURE 3.4 – (Color online) NAD magnitude of beads plotted against their Voronoi volume at several strains ε=0, 0.03, 0.06 and 0.09 (cavitation). Arrows describe the higher density value of each variable. No correlation was found between these variables for all strains. "Cavity cluster beads" are marked by the symbol ∘ : no remarkable trend can be distinguished, except during cavitation, where they exhibit larger NAD and slightly larger Voronoi volume.

the magnitude of NAD remains much less than inter-atomic distance (σ), in other words, the deformation is purely affine.

3.3.2 Stress fluctuations

The local stress on any given bead can be obtained by dividing the classical expression of the virial stress by the Voronoi volume $\mathbb{V}_m$ of atom m [MacNeill 2010],

$$\sigma_{ij}^m = -\frac{1}{2\mathbb{V}_m}\left(m_m v_i^m v_j^m + \sum_{n\neq m} r_i^{mn}.f_j^{mn}\right), \tag{3.2}$$

where v_i^m is the velocity ith component of atom m ; f_i^{mn} and r_i^{mn} are the ith component of force and distance between two interacting atoms m and n, respectively. The first term of this equation represent the kinetic contribution and the second one is the Cauchy stress. The hydrostatic stress S_{hyd} was calculated by computing the trace of the stress tensor, $S_{hyd} = -(\sigma_{11} + \sigma_{22} + \sigma_{33})/3$

Figure 3.5 compares the distributions of hydrostatic stresses at several strains during deformation. In the initial undeformed configuration, the distribution shows an exponential tail towards negative values. As the deformation increases, the negative values of the hydrostatic stress are progressively relaxed, so that the distribution narrows and becomes more symmetrical just before cavitation takes place. These

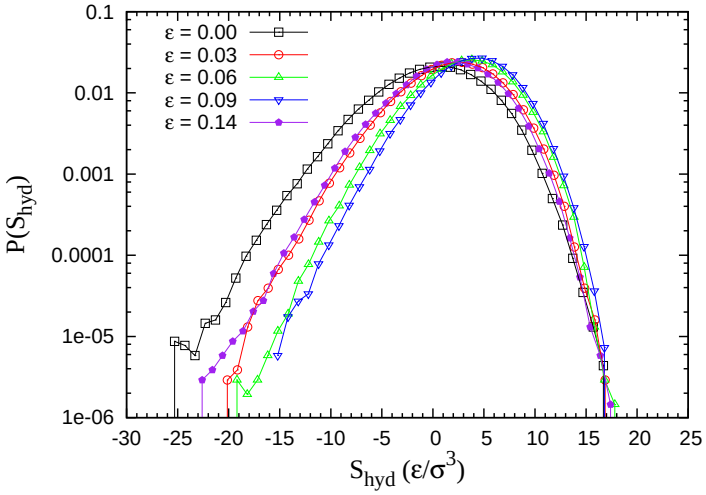

FIGURE 3.5 – Distribution of hydrostatic stress at different deformation levels. The distribution narrows until the cavity opens, then broadens again.

results are consistent with those of ref [MacNeill 2010]. After the cavitation has occurred, large negative values of the stress are again obtained, since the average free space is decreased as shown previously in Figure 3.2.

In order to investigate the correlation between NAD and the atomic hydrostatic stress, a scatter plot of these quantities is displayed in Figure 3.6. Apparently, there is no direct trend for a correlation between NAD and the hydrostatic stress at the scale of individual beads. The hydrostatic stress was also evaluated by considering each contribution separately (pair, bonded) at several strains, and again no correlations were found. When specific beads (chain ends and cavity cluster) values are selected in these scatter plots, the corresponding points appear to be a randomly chosen subset of the total sample. This absence of correlation may appear surprising, as the presence of a high local stress is often expected to result in plastic deformation. Note however that this result is consistent with a recent study [MacNeill 2010] which showed no correlation between atomic stresses and shear yielding in polymers. In an analogous way, a previous study on sheared glasses [Tsamados 2008] also failed to find a direct correlation between local stresses and the relevant local plastic deformation (shear transformations in that case).

It may be, however, that a more coarse grained characterization is necessary to identify such correlations, and that the cavitation events are the result of a local heterogeneity that extends beyond the scale of individual beads. In order to assess this hypothesis, we describe briefly in the next section studies performed on density fields defined at a more coarse grained scale.

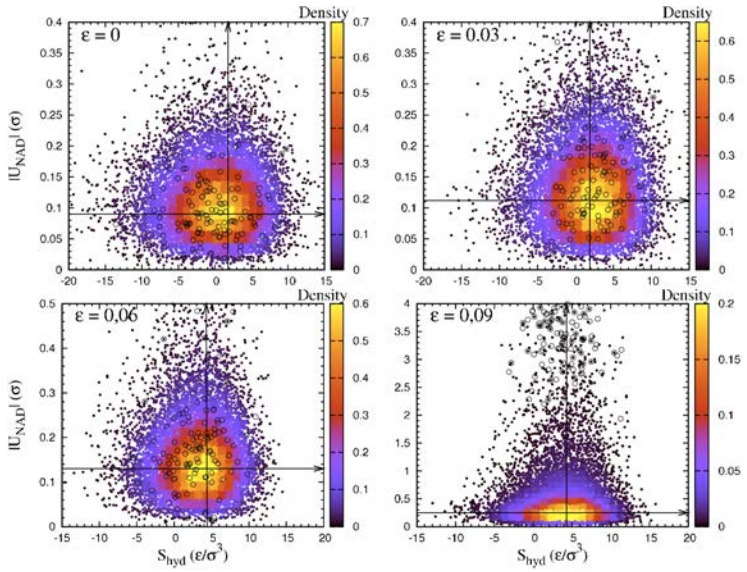

FIGURE 3.6 – (Color online) Scatter plot of the non affine displacement against hydrostatic stress shown at the same deformation as in Figure 3.4. No clear trend for a correlation can be established. The values corresponding to the beads that surround the cavity labeled by the symbol ∘ are randomly dispersed, thus preventing one to identify any specific correlation for these beads.

3.3.3 Coarse grained densities

The opening of a cavity under strain can be seen as a collective event, that involves at least those atoms that will form the cavity "skin" at the end of the process. The corresponding mechanical instability may therefore be the result of some density anomaly that extends over a region larger than a single atom size or Voronoi cell. We therefore have also explored the properties of our polymer system on such a coarse grained scale by defining continuous fields from the atomic positions. Various possibilities are available for such a coarse graining procedure [Goldhirsch 2002, Tsamados 2009, Detcheverry 2010] ; here we choose the simplest one, which consists in computing the densities on a regular grid by assigning to each grid node the atoms that belong to a fixed "voxel" volume around this node. The voxel size is taken in the range 5σ to 7σ, which was shown in similar studies [Wittmer 2002, MacNeill 2010, Papakonstantopoulos 2008] to permit a good description in terms of continuous fields (with about 120 monomers per voxel) while preserving the locality and possible spatial heterogeneity of the variables under consideration.

We have attempted to coarse grain and to correlate with the appearance of cavities two of the densities examined previously at the atomic level, namely the density of chain ends and the density of monomers. The local density field is defined as :

$$\rho_i = \frac{n_i}{\sum_j \mathbb{V}_i^j} \tag{3.3}$$

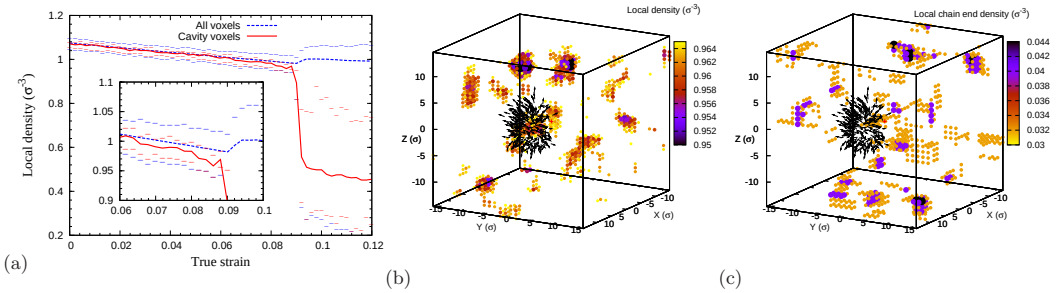

(a) (b) (c)

FIGURE 3.7 – (Color online) Evolution of mean local density calculated within cubic bins of size $5 \times 5 \times 5\ \sigma^3$. The average of the overall voxels (dashed line) is compared with the average of voxels that are associated with the cavity cluster beads (solid line). Symbols (-) denote the upper and lower values for each curve. The spatial distribution of local density taken at $\varepsilon = 0.08$ is shown in (b) and the corresponding map of chain end density in (c). The arrows describe the non affine displacement of the "cavity cluster beads". The dark spots identify the low density vicinities (b) and the high chain end density (c).

where n_i is the number of beads within a voxel i, and $\mathbb{V}_i^j$ is the Voronoi volume of the bead j that is included in the voxel i. Figure 3.7(a) shows the evolution of this local density with strain, and compares the average value with the value observed in the vicinity of the cavity.

These data show that the local density in the vicinity of the cavity follows the mean value until a deformation of $\varepsilon = 0.06$. Although cavitation does not occur until $\varepsilon = 0.09$, the local volume begins to decrease earlier (see inset). This observed trend can be interpreted by the fact that cavitation starts earlier than the drop of stress in the stress-strain-curve. This "pre-cavitation" behavior can be interpreted as resulting from a dynamical equilibrium between the elastic energy and the free surface energy of cavity with relatively small radius. This situation remains stable until the cavity reaches a critical radius (roughly estimated 2σ), beyond which the size of the cavity increases rapidly. The spatial distribution of the local density at $\varepsilon = 0.08$, just before the opening the cavity is shown in part (b) of Figure 3.7. The lowest density spots are far from the expected position of the cavity, but a low density can be noticed in the cavity vicinity. In general, we have checked that a systematic decrease in density prior to cavitation is specific of the points that are located in the vicinity of the emerging cavity. Other points may display fluctuations in their values of the density, but these fluctuations remain uncorrelated with cavitation events. After the cavity nucleation, the low density regions that did not form cavities release their excess free volume introduced by the triaxial deformation condition. Therefore the local density of such regions return to values similar to regions that are not involved in the cavitation. In conclusion, local loss of density should be seen rather as a consequence than as a cause of cavity nucleation.

As was mentioned above (in section 3.3.1), the free volume was found to be

correlated with the bead connectivity. Chain ends exhibit a higher Voronoi volume compared to other monomers, and a lower density of beads could be expected where a higher density of chain ends is present. We therefore define a local density of chain ends $\rho^{C.E.}$ as

$$\rho_i^{C.E.} = \frac{n_i^{C.E.}}{V_i}, \tag{3.4}$$

where $n_i^{C.E.}$ is the number of chain ends within a voxel i, and V_i is the volume of the voxel. Figure 3.7(c) shows that, at this level of coarse graining, the spatial distribution of chain ends is uncorrelated with the local density of beads and also with the cavity position. This indicates that the modification of the packing density by the presence chain ends is insignificant. Summarizing, the coarse grained density of beads exhibits a limited success as a predictor for cavity formation, as its evolution can be correlated with the formation of a cavity only shortly before the event actually takes place. The coarse grained density of chain ends, on the other hand, does not correlate well with the total density or with cavitation.

3.3.4 Local mechanical properties

Our last attempt to identify a microstructural predictor for cavitation events is inspired by previous work on simple glassy systems under shear deformation, in which a low value of the shear moduli was identified as a good indicator for the occurrence of the relevant local plastic events, shear transformation zones [Tsamados 2009, Papakonstantopoulos 2008]. Here the relevant events involve a local dilatation of the material which eventually gives rise to a cavity, and points to the local bulk modulus as a possible predictor.

Local heterogeneity in the elastic properties of glasses is now a well documented feature, with a number of studies having shown that the moduli defined at intermediate scales (of the order of 10 atomic sizes) are those of an isotropic but heterogeneous material. At such scales, a typical glassy sample can be described as a consisting of coexisting “hard” and “soft” regions. This behavior is independent of the precise method which is used to define the coarse grained elastic constant, which may involve either the use of statistical mechanical formulae at a local scale [Yoshimoto 2004, Papakonstantopoulos 2008], or exploiting the linear relationship between coarse grained stress and strain field [Tsamados 2009]. Here we present results for the local bulk modulus obtained from a third approach, originally introduced by P. Sollich *et. al.* [Sollich 2009], which has the advantage of being easily implemented at a reduced computational cost. The method can be summarized as follows : one first defines a coarse graining volume as a fictive shape that encapsulates a number of beads. The shape was chosen spherical in order to reduce any potential boundary effects, and the radius equal to 3.5 particle diameters, consistent with the typical coarse graining scales used in other methods [Tsamados 2009, Papakonstantopoulos 2008]. The entire sample is then deformed affinely (in this case using a uniform dilation of all bead coordinates). After this homogeneous deformation, all beads are kept frozen, except those contained in the

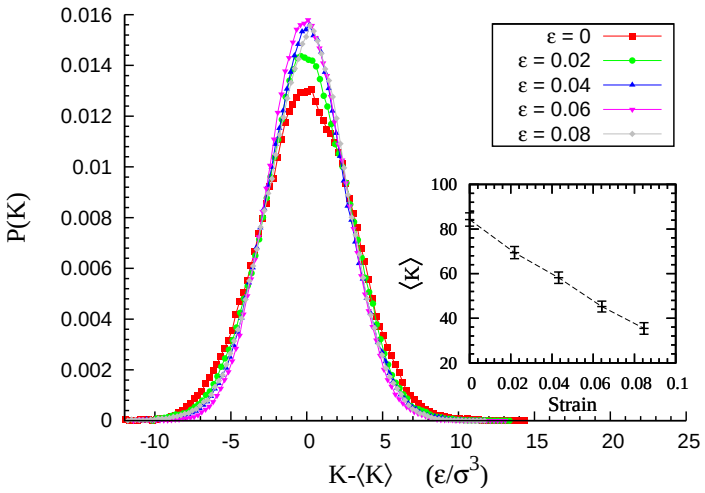

FIGURE 3.8 – Density distribution of local bulk modulus for the same specimen at several deformation levels. Distributions are shifted by their mean values. The inset shows the evolution of the mean values. Error bars are deduced from the standard deviation.

coarse graining volume which are allowed to fluctuate in a constant volume, constant temperature molecular dynamics trajectory (here we perform a trajectory at a rather low temperature, $T = 0.01$). The increase in the hydrostatic stress S^m_{hyd} within the spherical volume m is obtained from the virial stress formula, and the local modulus K^m can be defined by dividing this stress by the imposed increase in volumetric strain ϑ^m :

$$K^m = \frac{d(S^m_{hyd})}{\vartheta^m}. \tag{3.5}$$

In order to improve the accuracy on K^m, it has then been averaged over a dozen expansion tests within the domain $0 < \vartheta^m < 10^{-5}$. A sequence of deformation (isotropic expansion) and relaxation steps is applied over the sample, the gauge volume V^m and S^m_{hyd} are measured after each step. The expansion is limited to a very low deformation amount since the measurement is restricted in the elastic regime only. Substituting the ϑ^m by its definition $\frac{dV^m}{V^m}$ leads to another form of equation (3.5) :

$$K^m \cdot \frac{dV^m}{V^m} = d(S^m_{hyd}) \tag{3.6}$$

or equivalently

$$K^m \cdot \ln(V^m)|^t_0 = S^m_{hyd}|^t_0, \tag{3.7}$$

where V^m and S^m_{hyd} are integrated along the deformation trajectory from 0 to t. This method allows us to obtain an accurate determination of K^m in the linear regime by fitting the data obtained for S^m_{hyd}=f($ln(V^m)$). This procedure was applied along

each tensile deformation trajectory, for positions of the center of the coarse graining volume distributed on a regular grid.

Figure 3.8 compares the statistical distributions of the local bulk modulus at different strain levels. The plotted distributions are shifted by their mean values to facilitate comparison of their shapes. Curves remain symmetrical and Gaussian, whatever the applied strain before cavitation. As the deformation increases, the distribution will become slightly narrower. This behaviour is consistent with the trend described in the previous sections, that the polymeric system tends to homogenize its local stress under an applied deformation. The mean value of the local bulk modulus (see inset) decreases continuously as the deformation increases and more free volume is introduced in the system.

In order to investigate the spatial distribution of the local bulk modulus, two-dimensional slices in a plane perpendicular to the tensile direction were taken at the level at which the cavity is observed. Figure 3.9 shows a sequence of such bulk modulus cartographies that are captured along the deformation trajectory. Each slice corresponds to one of the blue markers on the stress strain curve (first plot in figure 3.9). The nonaffine vectors describing the formation of a cavity are also plotted on each map. As can be seen, the local bulk modulus fluctuates between high and low values at each strain, and the position at which the cavity appears corresponds to one of the low bulk modulus sites identified in the starting configuration. When the deformation increases, an extremely low value of bulk modulus appears in the expected position of cavity, as in slices (4) and (5). The lower value indicated here is not only a local minimum in the plane of the figure, but instead corresponds to the lowest value for the entire sample.

In the light of this strong correlation between NAD and elastic modulus, the cavitation process in glassy polymers can be described in the following manner : The polymeric system exhibits some fluctuations in the local elastic bulk modulus. As the deformation progresses, the statistical distribution of the bulk modulus changes : The mean value decreases, but the contrast of spatial distribution is conserved. At relatively high strain, one of the zones that initially displayed a low bulk modulus will reach an anomalous value, resulting in a favorable location for the subsequent growth of a cavity.

We will now investigate whether this behavior should be described as deterministic (the cavity systematically forms in a particular zone) or rather statistical (the cavity forms randomly in one of the zones with a low modulus) process. To this end, the same system was subjected to three tensile tests with different tensile directions x, y and z. The positions at which cavitation takes place were recorded and compared after each test.

Figure 3.10(a) shows that, for the same initial configuration, cavities nucleate in different zones. The same behaviour was also found for several systems with different temperatures. The cavities systematically nucleate in zones that are characterized by a low modulus in the initial state, however the specific site at which it is observed depends on the deformation path and on the tensile direction.

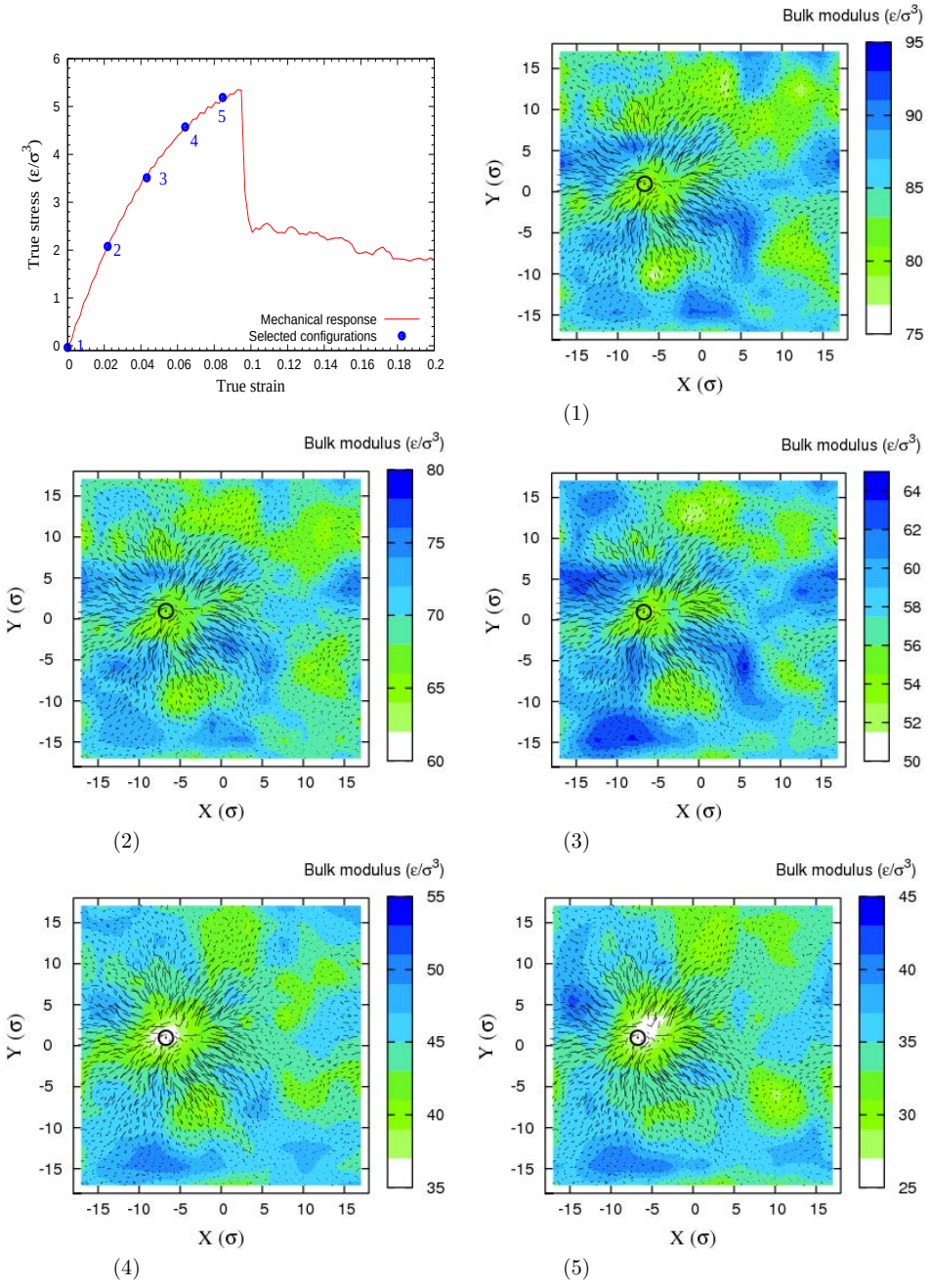

FIGURE 3.9 – (Color online) XY Layers taken from the spatial distribution of the bulk modulus (tensile direction is Z in this case). The Z coordinate of all layers corresponds to the cavity position. Every layer is indexed (bottom left corner) referring to its position in the stress-strain curve on the upper left. Theses maps are superimposed with the nonaffine displacement at $\varepsilon = 0.09$ that shows the formation of the cavity.

3.4 Conclusions

In this work the relationship between a cavitation event in a glassy polymer undergoing a tensile test and the local properties has been investigated with molecular dynamics simulations. Several properties have been analyzed at two different length scales : the elementary scale of the monomer, and a coarse graining scale of 5 to 10 particle diameters. Independent of the scale under consideration, we find that the density of monomers or the density of chain ends do not correlate with the subsequent appearance of a cavity. In contrast, the bulk modulus in the unstrained configuration displays fluctuations that can be directly related, in a statistical sense, to the appearance of a cavity at large deformations. Note that very similar conclusions were reached by Toepperwein and de Pablo in a recent study that considered both homopolymers and composite systems [Toepperwein 2011]. This situation resembles those observed in glassy materials under volume conserving shear, where a weak shear modulus indicates a tendency for plastic rearrangement.

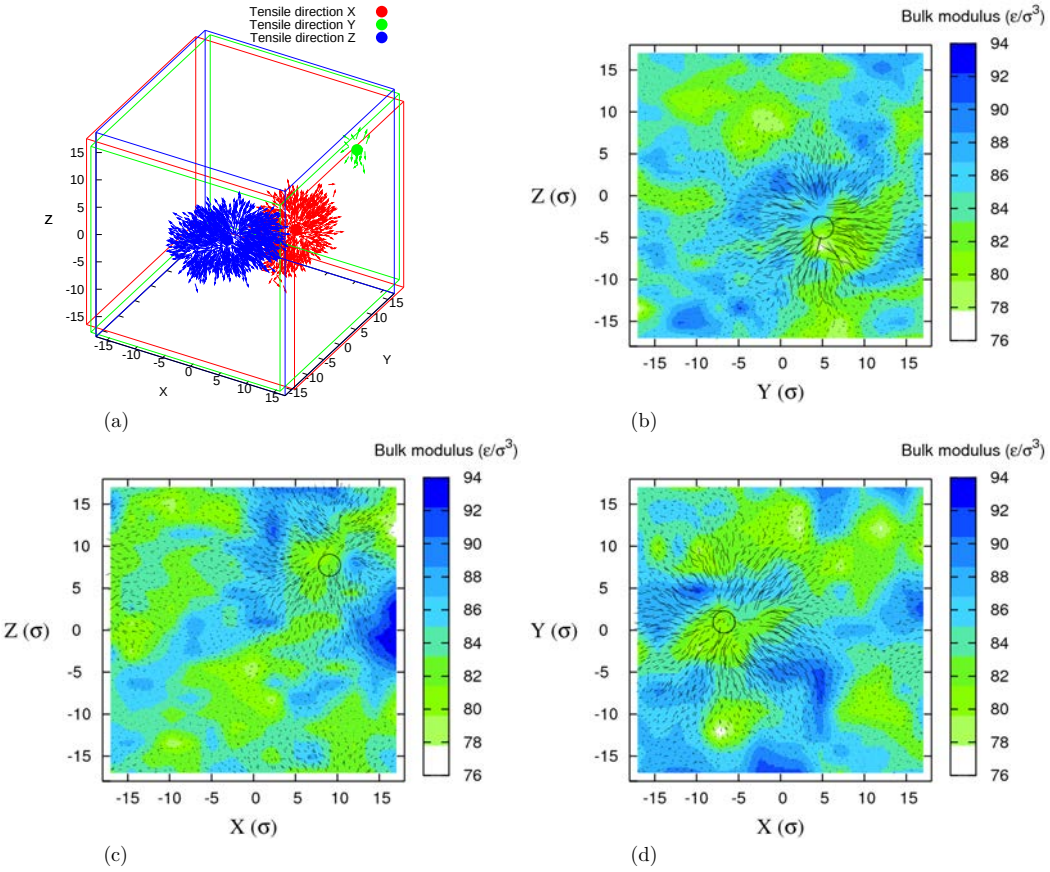

FIGURE 3.10 – (Color online), (a) Positions of cavities in a single sample after tensile tests with different straining directions. The vectors describing the formation of a cavity are superimposed with the corresponding map of local elastic bulk modulus imaged in the initial, undeformed, configuration. Slices (b), (c) and (d) are located in the corresponding position of the cavity nucleation and they are perpendicular to the tensile directions X, Y and Z, respectively.

Chapitre 4

Mechanical properties of nano-structured block copolymers

Contents

4.1 Introduction

Nanostructured polymers have attracted an increasing interest due to their ability of self-organization at nanometer scale. A large family of polymer can be described as nanostructured, including semi-crystalline polymers (e.g. PolyEthylene), block copolymers (SBS,SIS...) [1] and many others. These materials are exploited commercially in several manufactural fields because of their thermoplastic properties coupled with a good mechanical properties. The nano-structured polymers are characterized by local morphologies that depends on several factors especially the temperature, the processing history and also the volume fraction of the hard phase (glassy phase in the study presented below, or crystalline phase in semi crystalline polymers). These local morphologies can be controlled (form and orientation) for copolymers, less so case semi crystalline polymers. Semi crystalline polymers and

1. S denotes Styrene block,B Butadiene,I isoprene

segregated block copolymers reveal somme common micro-structural characteristics. At ambient temperature, both materials have two phases with different mechanical properties : the brittle hard phase (glassy or crystalline) and the ductile soft phase (rubbery). Under tensile strain condition the nano-structured material exhibits a composite mechanical response that depends on the stiffness of each phase and their coupling. Experimental results have shown a strong dependence between the molecular parameters (architecture) and the macroscopic mechanical response, this dependence was interpreted by the ability of molecules to ensure the transmission of stress between hard and soft phases. The mechanism of stress transmission and the coupling between phase at local scale is still not well understood.

The aim of this work is not to reproduce precisely the mechanical behavior observed experimentally but to provide more qualitative insights about the local mechanical response of lamellar nanostructured polymers in relation with the molecular definition of these materials.

In this chapter the mechanical properties of nanostructured polymer will be addressed using a coarse grained molecular dynamics model. We start by a quick review of the experimental and relevant simulation results. Then, we describe the mechanical response of the system in both serial and parallel coupling. The influence of molecular architecture, notably the bridging molecules on the mechanical response, is discussed as well as the influence of the surface tension between phases.

4.2 Quick review of relevant experimental an simulation works

4.2.1 Block copolymers

Block copolymers are a specific class of copolymer (polymers comprising more than one chemically distinct monomer) where the different monomers are not distributed within the polymer chain in random or alternating fashion but instead are localized in discrete homogeneous sections (or blocks) of the chain [Hamley 1998]. Conceptually a block copolymer can be thought of as two or more distinct homopolymers linked end to end through covalent bonds. The number of distinct homopolymer homogeneous sections determines the molecular architecture of block copolymer ; diblock, triblock, and higher multiblock copolymers are possible [Bates 1999].

Diblock copolymers and some triblock copolymers made of two distinct homopolymers are the simplest molecular architecture of block copolymers and have been largely studied. As polymer mixtures separate into different phases, the two blocks of the copolymer tend to demix locally. The covalent bond linking the blocks prevents the macroscopic phase separation observed in binary mixtures of the homopolymers and lead to a nanoscale structural organization of each block. The phase behavior of block-copolymers has been studied extensively from both experimental and theoretical perspectives [Semenov 1986, Larson 1994, Detcheverry 2008].

In short, the propensity for block copolymers to segregate into periodic na-

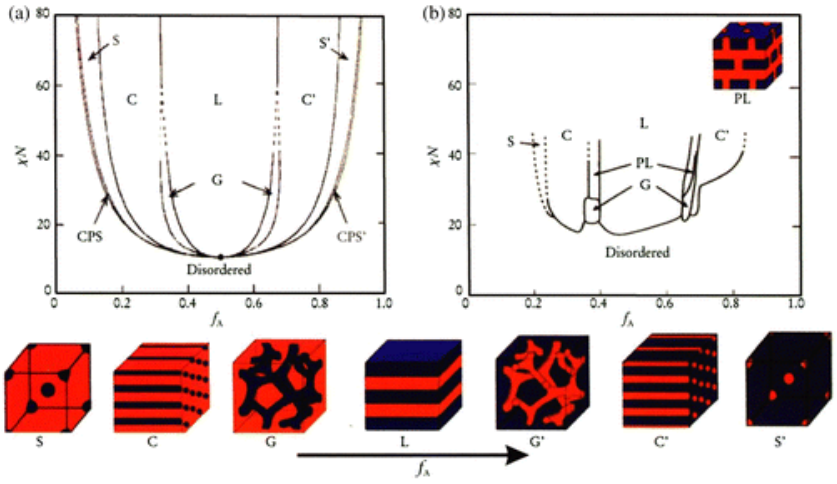

FIGURE 4.1 – Phase diagram for linear AB diblock copolymers. (Left) Equilibrium morphologies predicted by self-consistent mean-field theory : spherical (S), cylindrical (C), gyroid (G), and lamellar (L). (Right) Experimental phase diagram of poly(styrene-b-isoprene) (PS-b-PI) diblock copolymers : perforated layers (PL). (Bottom) A representation of the equilibrium microdomain structures as f_A is increased for fixed $\tilde{\varepsilon}N$. (Reproduced from ref [Bates 1999])

nodomains is determined by the strength of the repulsive interaction as characterized by the product χN, where χN is the Flory-Huggins interaction parameter [Doi 1995, Flory 1953] and N is the number of monomers per copolymer chain. In a lattice model [Doi 1995], χN is defined as :

$$\chi N = \frac{z.N}{2k_bT} * (\varepsilon_{AA} + \varepsilon_{BB} - 2\varepsilon_{AB}) \tag{4.1}$$

A and B are the block labels, z is the lattice coordination, k_b is the Boltzmann constant, T is the sample temperature, ε_{AA}, ε_{BB} and ε_{AB} are the interaction energies between A-A, B-B and A-B monomers respectively. in the following we will use as a rough estimate of the segregation parameter the corresponding combination using the LJ energies $\tilde{\varepsilon}N = \frac{N}{2k_bT} * (\varepsilon_{AA} + \varepsilon_{BB} - 2\varepsilon_{AB})$, which has been shown to be a good approximation of an effective χN [Grest 1996].

Microphase separation occurs when this value exceeds the critical value for the order-disorder transition. At equilibrium, this microphase separation is established by a energy balance between the stretching energy for the polymer chains and the energy of interactions at the interface between A and B microdomains. In block copolymers, the morphology of the microdomains ranges from spheres, cylinders to lamellae depending on the volume fraction of one block. Figure 4.1 presents a theoretical and an experimental phase diagram of a model diblock copolymer, poly(styrene-b-isoprene) (PS-b-PI) [Bates 1999] . As shown in the diagram, the lamellar morphology persists when the amounts of each phase are roughly the same,

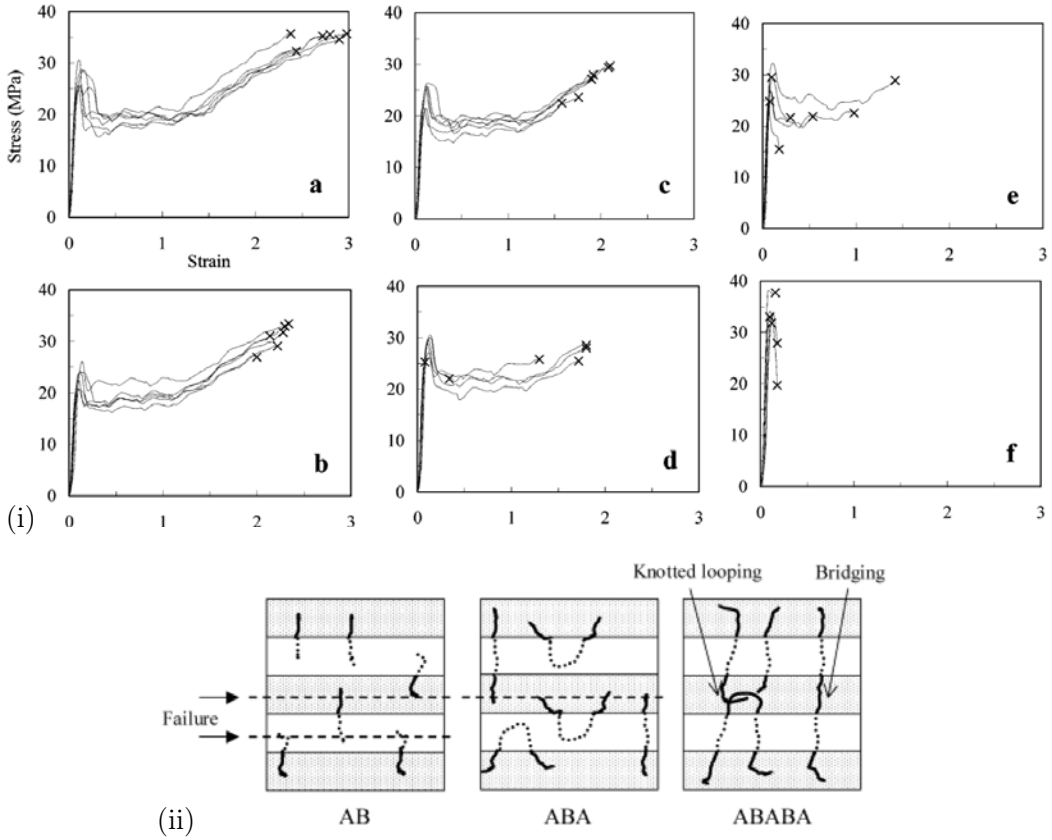

FIGURE 4.2 – Upper panels : tensile properties of an aligned mixture of CECEC (C= Poly-CycloHexylEthylene ; E=PolyEthylene) pentablock copolymers and CEC triblock copolymers : (a) 100% CECEC, (b) 50%, (c) 20%, (d) 10%, (e) 5% and (f) 0% pentablock (100% triblock copolymer CEC). The tensile stress is applied perpendicular to the lamellar orientation, the failure points are shown as "×". Lower panels show the fracture plane of lamella-forming AB, ABA and ABABA block copolymers. The dashed line indicates the fracture planes associated with domains containing unentangled blocks. The last figure from this panel shows the equivalence between the knotted loop and the bridge chains. (both figures are reproduced from [Mori 2003])

this morphology is the most stable at low $\tilde{\varepsilon}N$ (high temperature).

The lamellar morphology can be aligned in a specific direction by applying an oscillating shear. The mechanical properties of aligned block copolymers have been widely studied, the different mechanical responses were correlated with the change of the local morphologies and the molecular architecture of the sample. If the tensile strain is applied perpendicular to the layer orientation then the result is a composite mechanical response caused by the serial coupling of each phases. In parallel coupling, the mechanical response of the sample is dominated by the contri-

bution of the hard phase. Several studies were achieved in serial coupling response [Cohen 2000, Phatak 2006, Read 1999]. The deformation of each phase at local scale was followed by the Small Angle Xray scattering (SAXS) in situ. The evolution of the SAXS patterns shows that the deformation is supported by the soft phase at the low strain level. The concentration of strain in the soft phase leads to a nucleation of cavities in this phase. At high strain (after the necking) the hard layers buckles to a "chevron" like morphology. The evolution of buckling was characterized by the transformation of the SAXS pattern from an arc to a four symmetrical spots (details are provided in the next chapter section 5.2).

The role of the molecular architecture was also studied : a strong transition from brittle to ductile failure was observed when a sufficient amount of pentablock chains is mixed with triblock chains [Mori 2003]. (see figure 4.2(i)). In triblock system the ultimate failure is basically assigned with domains containing unentangled blocks. These blocks become bridged together if they are mixed with pentablock chains. (figure 4.2).(ii)) The bridging function is not only ensured by the tie molecule but also two knotted loop chains can be considered as bridge-like molecules.

4.2.2 Semi-crystalline polymer

Semi crystalline (SC) polymers such as PolyEthylene, PolyButene is another example of nano-structured polymer. Although we have not studied such systems in this thesis, we hope that some of the results obtained for aligned copolymers may have a range of validity that extends to their more complex morphology. At ambient temperature, the local structure of SC polymers is consistent with a rubbery amorphous chains confined between crystalline lamellae. The lamellae in semi crystalline polymers are oriented radially to form an aster-like lamellae arrangement. This aster is so called spherulite. The crystallinity and the lamellae thickness were found to depend on the processing history of such material. Under tensile strain, the spherulite exhibits a non affine response at which the deformation begins in equatorial zones and propagates to the polar zones [Weynant 1980, G'Sell 1994]. Therefore, the local response of semi crystalline system is analog to the response of aligned copolymer, the deformation will be first supported by the rubbery soft phase of the equatorial zone before deforming the crystal lamellae. (as shown figure 4.3).

The experimental constitutive law of semicrystalline polymers is shown in figure 4.4.a., the mechanical response exhibits four main regimes : (i) the elastic regime is correlated with the elastic deformation of the equatorial zone (stretching of amorphous chains). (ii) the yield corresponds to the cavitation, which leads to a progressive destruction of the crystallite network. Macroscopically the yield point is accompanied with the necking and whitening of the sample. (iii) the drawing regime, which occurs at constant stress, corresponds to the propagation of the neck in the sample transforming the local microstructure to fibrils. (iv) the strain hardening regime corresponds to the stretching of chains.

As demonstrated by many experimental studies [Humbert 2009] the transmission of stress between the crystalline phase is ensured by the bridging chains called

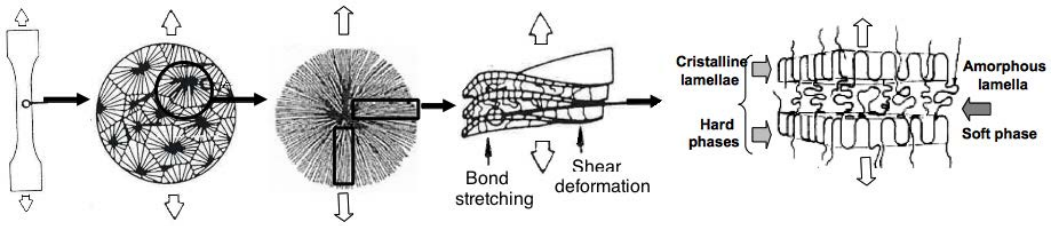

FIGURE 4.3 – Sketch of the deformation of semi crystalline polymer at several scales, the macro-scale deformation will be localized mainly in the equatorial zone of the "spherulite". The local deformation is supported by the amorphous phase confined between two crystalline phases. (reproduced from [David 2002])

also stress transmitters in reference [Humbert 2010]. The role of stress transmitters becomes relevant in the strain hardening regimes because of the entanglements network developed by bridging molecules after breaking the hard phase. According to several studies [Bartczak 2005, Schrauwen 2004, Haward 1993] figure 4.4.b shows the influence of the stress transmitters on the strain hardening modulus (fitted from the equation 1.9), the increase of stress transmitter amount will eventually increase the strain hardening modulus of the sample.

On the other hand, the decrease in the number of stress transmitters between crystalline layers leads to a fast stress concentration in the crystalline lamellae and the damage of the latter begins by chain pullout. (see figures 4.5.a) This influence was observed within an atomistic simulation model of semi crystalline PolEthylene [Monasse 2008]. Similar results were found in reference [Sides 2004], this study was carried on specific coarse grained systems that contains end tethered chains [2]. These systems exhibit different responses with respect to the density δ of end-tethered chains : chain pullout behavior was observed when the brush density is low, such case corresponds to a bad coupling between the grips and the entire system. In the opposite case, sample crazing is observed when the density of end tethered chains is very high (see figure4.5.b).

4.3 Interaction parameters and choice of the temperature for the tensile test

As we will show in appendix A, the building and the relaxation-segregation processes of triblock samples were carried out at relatively high temperature, in order to increase the chain mobility and then to accelerate the relaxation of the system [3]. Therefore, just after the relaxation of the sample, both phases are in a soft

2. Chains that have one of their ends free in the bulk while the other end is tethered to the deformation grips

3. The sample building was proceeded at $T = 2$ and the relaxation-segregation stage is performed at $T = 1$

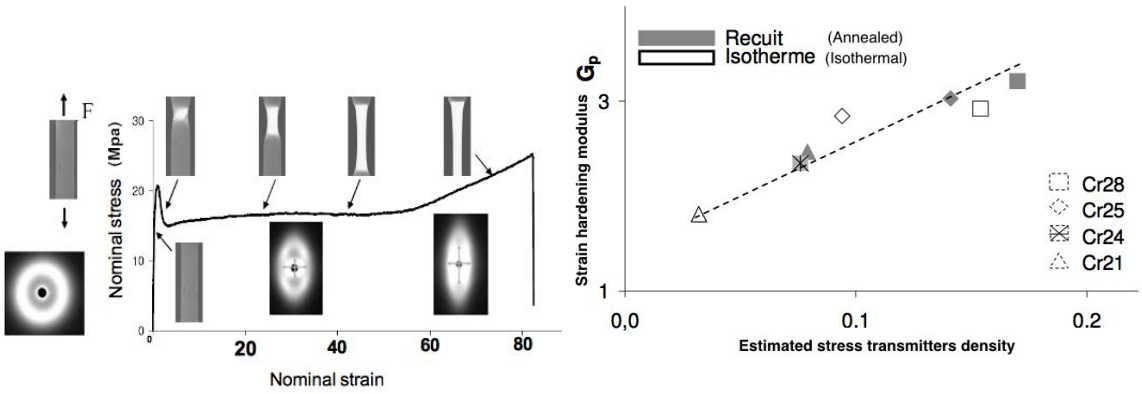

(a) (b)

FIGURE 4.4 – (a) Experimental constitutive law of a typical semi crystalline polymer PE (Polyethylene). (b) The evolution of the strain hardening modulus G_p with respect to the amount of stress transmitters ST (bridging molecules or knotted loop molecules). The amount of ST was modified experimentally by modifying the processing of the sample. Decreasing the stress transmitters leads to a stress concentration in the hard phase which decreases severely the strain hardening modulus [Humbert 2009]).

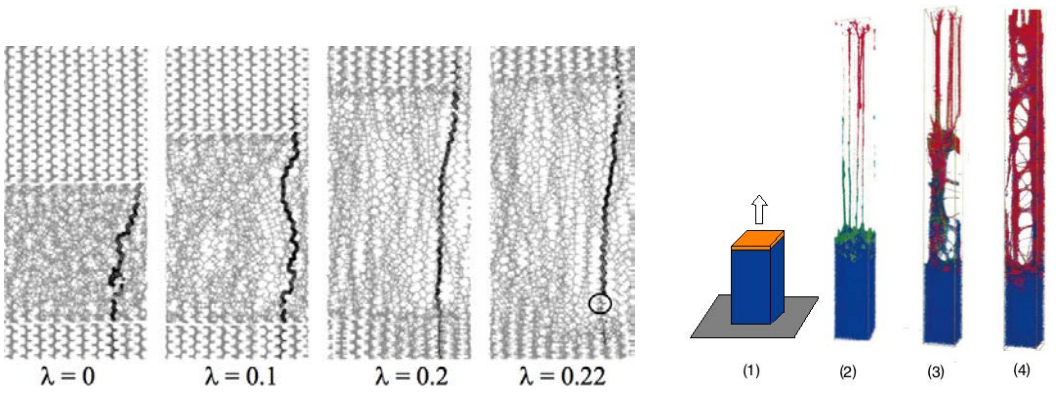

(a) (b)

FIGURE 4.5 – (a) Tensile strain snapshots of an atomistic model of PE chains. The damage of the crystalline phase starts by chain pullout. (the bold chain) λ denotes the corresponding engineering strain. the figure is extracted from [Monasse 2008]. (b) Snapshots of stretched samples with different tethered chains surface density. (1) undeformed sample. The surface density δ in (2) $\delta = 0.02\sigma^{-2}$, in (3) $\delta = 0.05\sigma^{-2}$, in (4) $\delta = 0.1\sigma^{-2}$. All samples were deformed at the same velocity. The presented snapshots are taken at the same strain. The mechanical response change from chain pullout to crazing by increasing the tethered chain density [Sides 2004].

rubbery state, then the system must be cooled to a selected temperature to obtain a nanostructured system with alternating hard and soft phases.

Therefore, the identification of the glass transition temperature T_g of each block in the system is an important step to choose the working temperature range where one of the constituents is a hard glass while the other is a soft rubber.

Effectively, this working temperature range is bounded between the T_g of each phase.The size of this range (the difference between T_g) depends upon the difference of the LJ interaction energies of each phase (ε_{AA} and ε_{BB} in equation A.1). For this reason, the LJ interaction energy of one phase was chosen higher than the other in our system. In this chapter : The phase that has the higher LJ energy (and therefore the higher glass transition temperature) will be called phase A, and the other, softer phase is called phase B.

The difference in LJ interactions was introduced before the relaxation-segregation stage in the sample building process. (see Appendix A for further details) Four different systems were build with different intrablock LJ interactions : (ε_{AA}, ε_{BB}, ε_{AB}) are taken equal to (1, 0.1, 0.3) , (1, 0.2, 0.35) , (1, 0.3, 0.4) and (1, 0.5, 0.5). The inter-block interaction is chosen in such a way that all systems have the same segregation parameter $\frac{k_B T}{N}\tilde{\varepsilon}N = 0.25$. Note that all samples are composed from 320 chains with 200 beads/chain. In order to probe glass transition temperature of each phase, every sample was cooled just after the relaxation process from $T = 1$ to a very low temperature $T = 0.001$. The evolution of the volume in each phase with respect to the temperature was analyzed. The geometric measure of each phase volume in a segregated system is somewhat problematic because of the diffuse boundaries between phases. For this reason, we use an indirect method to evaluate the block volume V^A, which can be written as :

$$V^A = L_x \times L_y \times L_z^A \tag{4.2}$$

where L_x and L_y are the simulation box length in x and y directions, L_z^A is the length of the block A in the z direction. L_x and L_y are given by the simulation output. L_z^A is evaluated by fitting the density profile of phase A with the following function :

$$f(x) = \frac{a}{2}\{\tanh[b.(x - c_1)] - \tanh[b.(x - c_2)]\} \tag{4.3}$$

The variable a fits the density, b fits the interface width. c_1 and c_2 correspond to the inflection points of the density profile. Thus L_z^A will be equal to $c_2 - c_1$.

Figure 4.6.a compares the density profile of block A in z direction (red points) with the fit function mentioned in the equation 4.3 (dashed line). The function (1.2) offers a satisfactory prediction of the density profile which validates the method to measure the block width and to obtain the block volume.

Figure 4.6.b shows the evolution of $\ln(V)$ of both A and B phases with respect to the temperature. Two linear regimes can be distinguished in each curve. The slope of each regime characterizes the volumetric expansion of the material at constant pressure. The change of slope in the same curve indicates the transition of the block from rubbery at high temperature to glassy at lower one [Schnell 2006]. To locate the

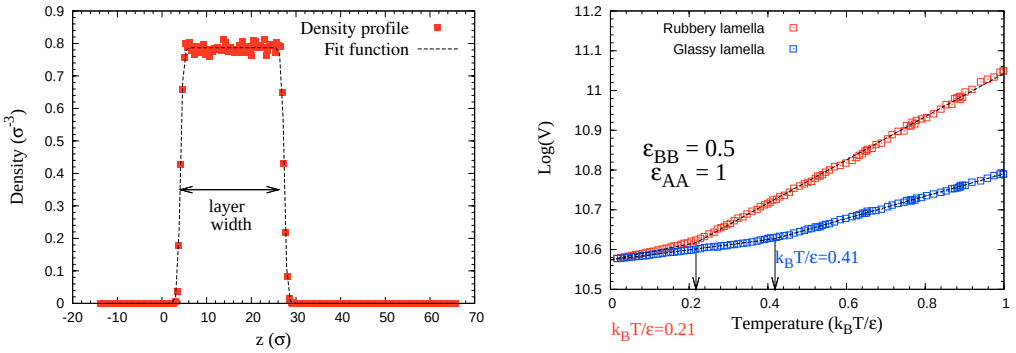

(a) (b)

FIGURE 4.6 – (a) Density profile of a specific block fitted by the function $f(x) = \frac{a}{2}\{\tanh[b.(x-c_1)] - \tanh[b.(x-c_2)]\}$, (b) Glass transition of both phases, the two linear regimes of each curve are fitted, the glass transition temperature T_g of each block corresponds to the change in slope.

glass transition temperature on the curves, the two linear regimes of each curve are fitted independently, and T_g corresponds to the abscise of the intersection point. For a system with $\varepsilon_{AA} = 1$, $\varepsilon_{BB} = \varepsilon_{AB} = 0.5$ we find $T_g^A = 0.41$ and $T_g^B = 0.21$. Note that in figure 4.6.b we show only one specimen as an example, the other samples were analysed in the same manner and their glass transition temperatures are given in figure 4.7.

Choice of the tensile test temperature : To create a nanostructured system behavior with coupled hard and soft phases, the choice of the tensile test temperature is crucial because at this temperature one phase must be glassy while the other must be in the rubbery state. After the identification the glass transition temperature of each phase A and B, the tensile test temperature T_{test} is chosen in the middle of T_g^A and T_g^B. In such case, as $T_g^A < T_{test} < T_g^B$, thus at T_{test} : A is a hard glass and B is a soft rubber.

Figure 4.7.a presents the interval between T_g^A and T_g^B of several samples with different ε_{BB}. As theoretically predicted, T_g^B decreases when ε_{BB} decreases, which leads to a large margin to choose T_{test} for the lower ε_{BB} samples. The tensile test temperature was chosen to 0,3. Therefore all samples are cooled to 0.3, the density profile of the entire sample after cooling is shown in figure 4.7.b. the density alternates between high density for the glass and low density for the rubber. Note that, all samples have 2 lamellae A and 2 lamellae B organized as $A_1B_1A_2B_2$ to ensure periodicity.

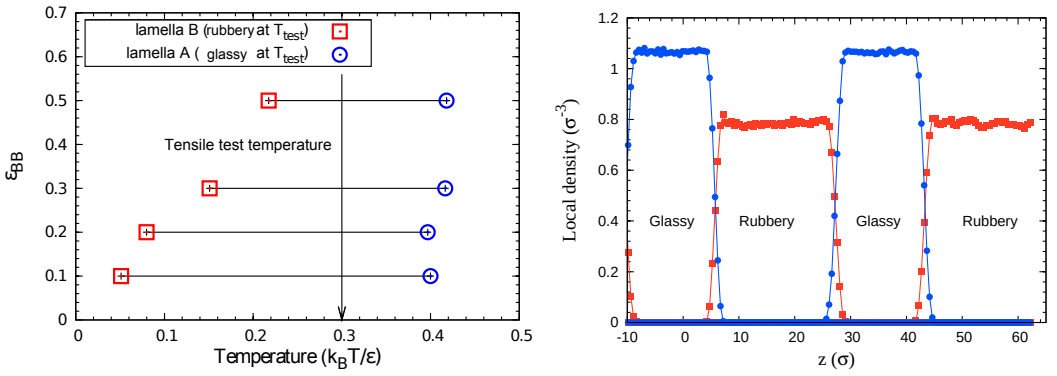

(a) (b)

FIGURE 4.7 – (a) The range between the glass transition temperatures of both system components. Several systems with different ε_{BB}, ε_{AB} are shown. The tensile test temperature T_{test} was chosen in the interval between the two glass transitions, $T_{test} = 0.3$.(b) Density profile of the entire sample (for the energy parameters (1.,0.5,0.5)) taken at the tensile test temperature.

4.4 Mechanical behavior

In order to probe the mechanical response of the prepared samples, these samples were submitted to several tensile tests at the chosen temperature $T_{test} = 0.3$. Two coupling modes are tested. The serial coupling (Reuss) and the parallel coupling (Voigt). Homogenous uniaxial tensile tests are performed to draw the samples at a constant velocity. The process was detailed in chapter 1.

4.4.1 Serial coupling

In serial coupling condition, the tensile direction is perpendicular to the block orientation. The tensile velocity V_z was chosen in a way that the initial strain rate is equal to $\dot{\varepsilon_{zz}} = \frac{V_z}{L_z} = 7.2 \times 10^{-5}$ for all tested samples. Two samples are considered in this section : (1, 0.2, 0.35) and (1, 0.5, 0.5). Both samples have the same $\tilde{\varepsilon}N$ but the soft phase of the first one has a lower LJ energy parameter and therefore a higher mobility than the second one. This difference can be described by the ratio of $\frac{T_{test}}{T_g}$ of the soft phase. This ratio is equal to 3.75 for the first sample and 1.42 for the second sample. The mechanical response of the first sample is shown in figure 4.8. The stress strain curve (first y axis) was superimposed with the local strain in each block (secondary y axis). As shown in the figure the stress strain- strain curve exhibits different regimes :

– The elastic regime : where the growth of the stress is quasi linear with respect to the global strain. As shown in the inset, this regime is correlated with the deformation of the soft phases, The hard phase is undeformed. Therefore, the hard phase in this case behaves as rigid clumps that forbid the deformation of

the soft phase in lateral directions x and y [4](see snapshots in figure 4.9). As the soft phase deformation is constrained laterally by the hard phase, the increase of global deformation will continuously increases the soft phase volume and then the elastic regime is soon interrupted by the nucleation of cavities in one of the soft phase layers. Under these deformation conditions the soft phase will be locally submitted to a triaxial tensile condition then the Young modulus of the entire system is effectively the elastic slope of the soft phase under triaxial tensile conditions. (named E' in chapter 1, section1.4.2).

– The yield and the stress softening after the elastic regime, correlated to the cavitation in the soft phase : indeed, the inset shows two peaks in the stress strain curve. The first one at yield strain corresponds to the cavitation in a one block of the soft phases (B1). The strain will be localized in this block, the deformation of the other soft block (B2) is relaxed and its local strain exhibits a plateau. The occurrence of the first cavitation event relaxes the tensile stress, but as the global deformation continues increasing in the block B1, a strain hardening begins in this block. The stress rises again, the second block B2 starts to deform until a certain strain where the cavitation occurs in this block, thus giving a fast increase in the local strain of block B2. This cavitation event corresponds to the second peak of stress after the yield.
– The strain hardening regime, which occurs in the sample after cavitation. The stress increases slowly between $0.4 < \varepsilon_{zz} < 1$, while the local strain of the hard phase remains nearly equal to zero. Therefore this strain hardening is correlated with the change of chains orientation in the soft phase that becomes more and more stretched in the tensile direction. When the global deformation reaches 100%, the soft portion of the triblock chain is stretched enough to trigger the plastic deformation of the hard phase. The deformation of the glassy phase is correlated with a fast growth of the stress in the strain hardening regime of the stress-strain curve. As the hard phase is not well entangled [5], the deformation of the glassy phase will align the glassy chain portion in the tensile direction an the system begins to disentangle. When the disentanglement of all chains is achieved, the weakest glassy phase breaks. The failure is shown in figure 4.18.a below.

To understand how the applied deformation is distributed in each phase. Figure 4.9.a. highlights the averaged deformation evolution of the hard and the soft blocks when the tensile conditions are applied. The averaged strain of the soft phase shows a continuous increase when the global strain increases, but the glassy layer still undeformed until a global strain of 1. As the chains in the soft phase are clumped by hard blocks, the deformation of the soft phase in the tensile direction is constrained. The stretched FENE bonds transmits the tensile stress from the soft to the hard phase. Under such conditions, the hard phase starts to deform. The deformation of the glassy block is driven by plastic movements and then disentanglement of the

4. These directions are perpendicular to the tensile direction z

5. the glass portion length is equal to 50 while the entanglement length is ~ 78 as depicted in chapter 2, section 2.2.2

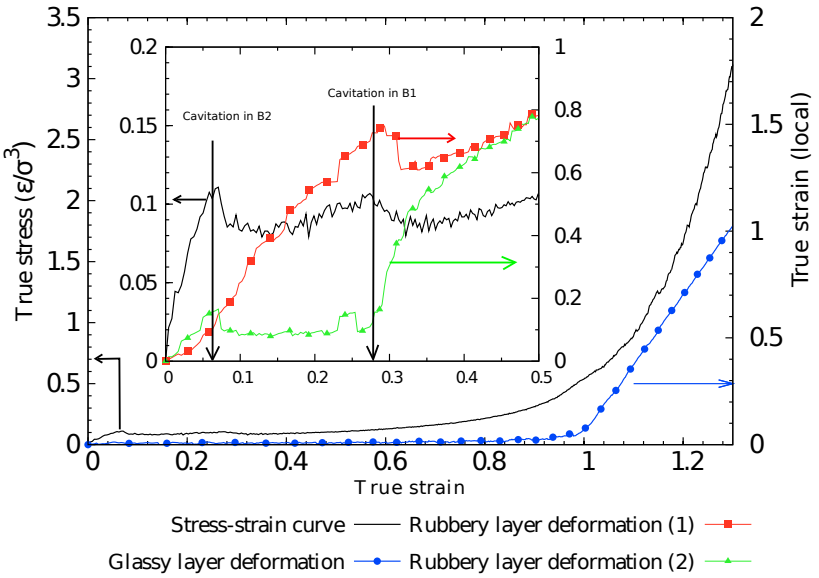

FIGURE 4.8 – Mechanical response of a serial system with a sequence of glassy rubbery blocks. The LJ energies are as follows : $\varepsilon_{AA} = 1$, $\varepsilon_{BB} = 0.2$ and $\varepsilon_{AB} = 0.35$, The corresponding segregation parameter $\tilde{\varepsilon}N$ is equal to 170 at $T = T_{test} = 0.3$. The stress strain curve was superimposed with the local strain of the glassy block (The secondary y axis in the main plot). The local strain of each rubbery block is shown in the inset. The stress drop after the elastic regime corresponds to the cavitation in the soft blocks. Up to a true strain of 1, the deformation is still localized in the soft phase and the glassy phase is undeformed.

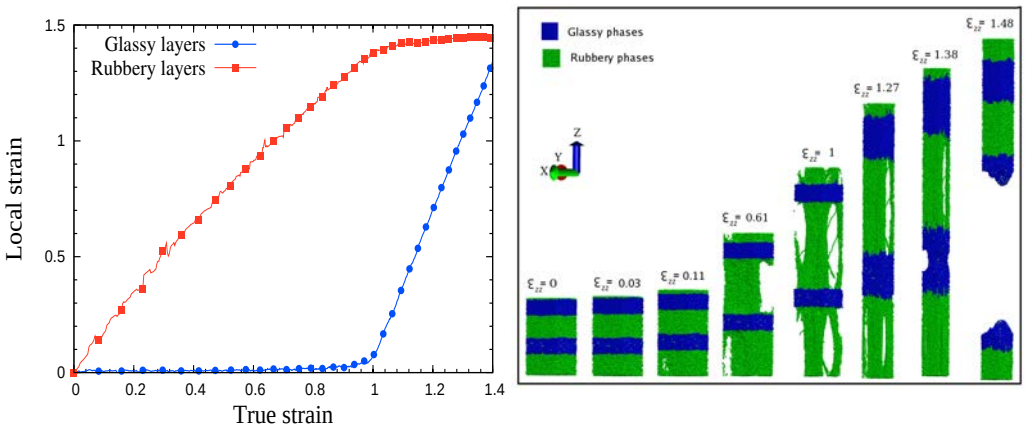

FIGURE 4.9 – (a) Average of the local strain of the two hard and the two soft phases in a serial coupling tensile test (LJ energies are same as in the previous figure).(b) Snapshots showing the deformation and the cavitation in the soft phase.

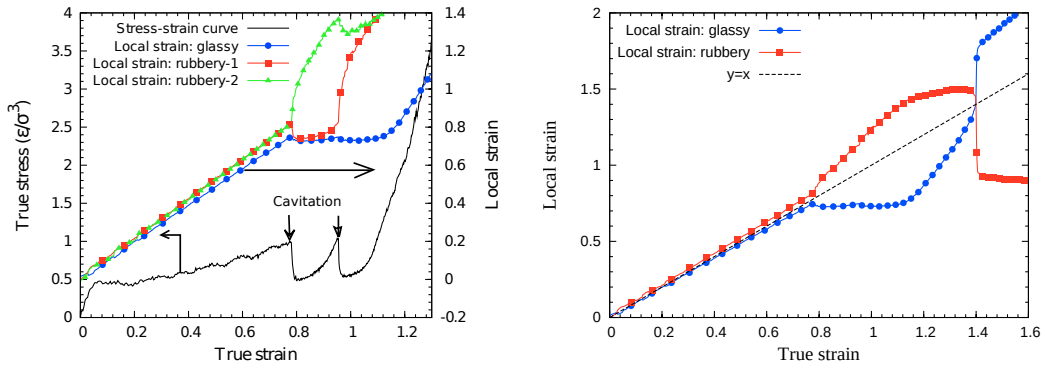

(a) (b)

FIGURE 4.10 – (a) Stress-strain curve of a serial coupled triblock system.The LJ energies are as follows : $\varepsilon_{AA} = 1$, $\varepsilon_{BB} = 0.5$ and $\varepsilon_{AB} = 0.5$, The corresponding segregation parameter $\tilde{\varepsilon}N = 170$ at $T = T_{test} = 0.3$. (b) The avraged strain of the hard and soft phases.

glassy chains.

The second sample (1, 0.5, 0.5) was also submitted to a uniaxial tensile strain condition at the same initial strain strain rate as the previous (1,0.2,0.35) sample. The tensile test temperature is again $T_{test} = 0.3$.

As shown in figure 4.10, the stress strain curve of the sample exhibits a completely different mechanical response from the previous sample. The stress-strain curve displays several regimes : the linear elastic regime that corresponds to a homogenous increase of strain in both hard and soft phases. In contrast to the previous case, the deformation is not localized in the soft phase. Both glassy and rubbery phases respond with the same behavior to the applied deformation. This behavior is also observed in figure 4.10.b where the average local strains of the glassy and the rubbery blocks are identical to the applied strain. Since the soft phase is confined between two hard phases, then the soft phase is submitted to triaxial tensile stress. We have shown previously in chapter 1 table 1.1, that triaxial elastic slope of such a rubber (E') may have the order of magnitude as the Young modulus of the glassy sample. When the deformation is applied, the stress state is triaxial. Under such conditions and as the LJ interaction in the rubber is strong, ($\varepsilon_{BB} > k_B.T_{test}$) the bulk elastic modulus of the glassy and the rubbery phase are nearly the same and therefore the sample deforms homogeneously (see the snapshots of figure 4.11). Note that in sample 1 (1,0.2,0.35) the soft phase B is a very weak rubber since $\varepsilon_{BB} < k_B.T_{test}$.

The stress growth of the elastic regime is limited by the yield that corresponds to the onset of the plastic events in the glassy phase, rather than by a cavitation in the rubber which would manifest itself by a faster increase of the deformation in the rubber. After the yield, the strain hardening begins, the stress rises slowly and the glassy phase hardens progressively. At $\varepsilon_{zz} = 0.77$ a drop in the tensile stress

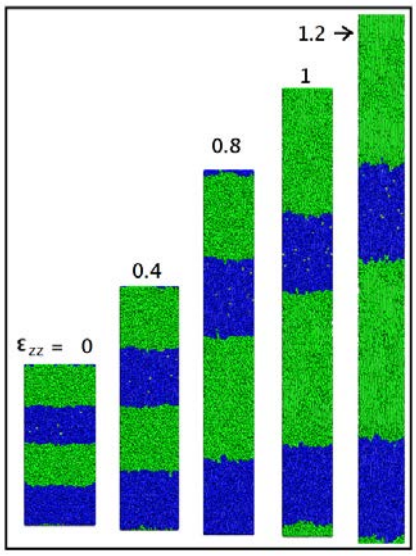

FIGURE 4.11 – Snapshots showing the hard (in blue) and the soft (in green) phase deformation. The constitutive law and the local strain of the system are shown in the previous plot.

occurs, this drop is correlated with the cavitation in one rubber phase B2. The strain becomes localized in B2. another drop of stress occurs also at $\varepsilon_{zz} = 0.95$ this drop corresponds to the cavitation in the second rubbery block. The cavitation relaxes the hard phase strain, but finally the failure of the hard phase occurs due to chain disentanglement. (The complete curve is shown in figure 4.21).

4.4.2 Parallel coupling

The first sample (1,0.2,0.35) was also submitted to a uniaxial tensile strain where the lamellae are parallel to the tensile direction (y direction). This sample with a strong elastic contrast between phases has been chosen, as a strong difference is expected in comparison with serial coupling. Indeed, we have shown that the local deformations of hard and soft phases are strongly different during a serial coupling tensile test. In a parallel coupling test, both phases are submitted to the same tensile deformation simultaneously (Parallel coupling called also Voigt coupling). The mechanical response of the parallel coupling test is compared to the serial coupling one in figure 4.12. First, the elastic regime results from the deformation of both hard and soft phase. The mixing law defines the resulting elastic slope as :

$$E_{\parallel} = f_{hard}.E_{hard} + f_{soft}.E_{soft}. \tag{4.4}$$

where $E_{\parallel}$, E_{hard} and E_{soft} are, respectively, the Young modulus of the entire sample, of the hard phase and of the soft phase. f_{hard} and f_{soft} are the corresponding volume fractions.

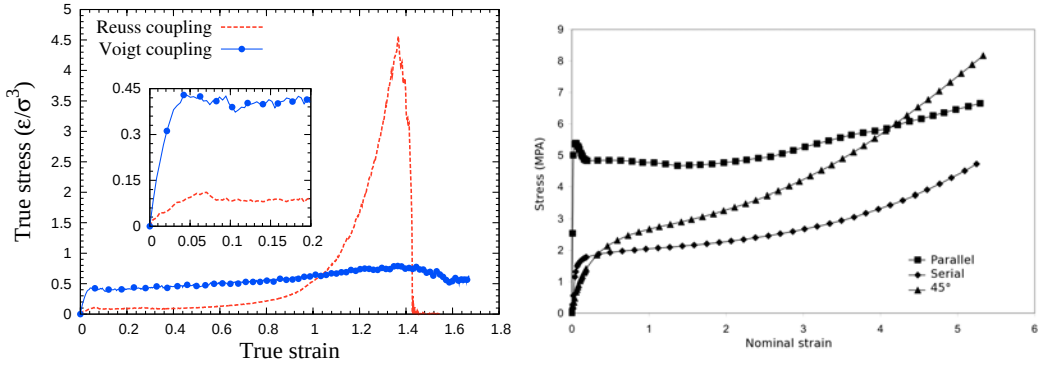

(a) (b)

FIGURE 4.12 – (a) Comparison of the stress strain curves between serial (Reuss coupling) and parallel coupling (Voigt coupling). (b) Similar results are found by experimental works on shear aligned SBS block copolymers (reproduced from [Gonzalez 2006]).

In contrast with the serial coupling case, the lateral deformation of the soft phase (and the entire system) is allowed in parallel coupling. Therefore, the system can relax the increase of volume by the Poisson effect and then each phase will be submitted to uniaxial tensile conditions. This condition is fundamental to justify the equation 4.4. In parallel coupling, the value of $E_{\parallel}$ is dominated by the contribution of the hard phase Young modulus, which is not the case in serial where the elastic slope $E_{\perp}$ of the system is determined the triaxial elastic slope of the soft phase E'_{soft}.

The elastic regime is limited by the beginning of the plastic events (shear yielding) in the hard phase. As the tensile strain is uniaxial, cavities do not form in any of the phases. The yield is followed by the strain hardening regime that takes place in the glassy blocks. As the chains in the glassy phase are relatively short and not well entangled, chain disentanglement progresses in the glassy block. The disentanglement of chains becomes more pronounced in specific weak points. A slight necking appears in these points, the necking progresses until the fracture of the glassy block occurs. Figure 4.13 shows the evolution of the deformed configuration and the ruptured glassy layer at a true strain of 1.5. The rupture of the glassy phase leads to a cavity between the glassy phase fragments. The latter can not be filled with the soft phase chains.

Figure 4.12.b compares the experimental stress strain curves of a lamellar triblock SBS (Styrene-Butadienne-Styrene) copolymer. This triblock exhibits some similarities with the tested model (same morphology, same alternation of soft-hard phases...). The simulation results capture the the influence of the system orientation on the mechanical response. Note that the experimental samples buckle under

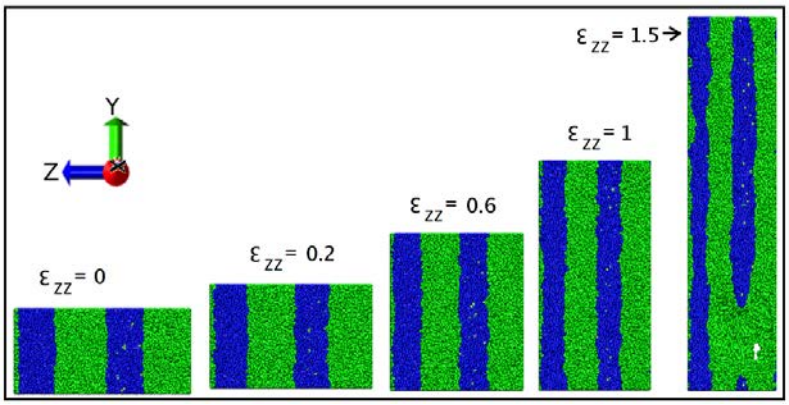

FIGURE 4.13 – Snapshots showing the evolution of the sample submitted to a parallel coupling tensile test. A rupture induced by chain disentanglement is obseved in the hard phase at high strain, the latter is followed by the cavitation in the soft phase.

a perpendicular tensile strain but this phenomenon is not observed in the simulation works of this chapter because of the small size of used samples. However, the buckling of triblock samples are observed by simulation for larger samples, as will be detailed in the next chapter.

4.5 Influence of chain architecture and conformation

The composite behavior of the nanostructured systems is ensured by mechanical coupling of their components. In the previous section we have shown the influence of the the tensile direction on the mechanical response of block copolymer samples. In parallel coupling, the material exhibits a strong stiffness as the sample response is governed by the hard phase behavior. in serial coupling (when $\varepsilon_{BB} = 0.2$), the deformation was mainly localized in soft phase at low strain, the hard blocks start to deform only at relatively high strain. Therefore, the system in serial coupling combines the ductility of the soft phase and the stiffness of the hard phase. Indeed, this desired property is provided by the transmission of stress between phases that is basically ensured by two kind of coupling : (i) the strong bonds that bridge the segregated phases together and (ii) the weak LJ interaction at the interface. the first kind of coupling is relevant at high strain, when the chains become stretched, while the second kind is effective at low strain.

As described in the introduction, various chain architectures and conformations can be found in nano-structured systems (multi-block copolymer, semi crystalline polymer) : (i) cut chains, also called cilia molecules, (ii) loop chains and (ii) bridging chains, also called tie molecules in some references. Depending on phase components (molar mass) and the elaboration process, a nano-structured system may enclose several of these architectures. (*e.g.* the high frequency low amplitude oscillatory shear

favors the formation of loop conformations in shear aligned pentablock system.) It has also been demonstrated that the formation of tie molecules in semi crystalline polymers such as PolyEthylene is enhanced by a high crystallization speed (during a quench for example). In appendix A we have shown how the chain architecture can be modified and tuned within the building and post processing procedure. The resulting samples were presented in figure A.7.

Again, we study here the simplest case of triblocks with alternating glassy and rubber layer. We expect however that the results may be relevant for other systems with an alternating hard and soft phases : semi crystalline polymers [6], semi crystalline triblocks [7].

4.5.1 Influence of cilia molecules :

Several samples with different amounts of chains cut in their middle (cilia molecules) were built as detailed in appendix A. Two kinds of chains are present in these samples : cut chains and bridging chains. The proprotion of cut chains are the following : 100%, 90%, 80%, 60%, 40%, 20% and 0%. Note that when a chain is not cut, it is a bridging chain (There are no loop chains in the samples). To refer to a specific sample we use the nomenclature S^c_x for the sample with x% of cut chains and S^l_x, for the sample with x% loop chains (next section). *e.g* S^c_{60} designates the 60% cut chain sample. Note that the LJ energies in these tests were chosen as $(1, 0.2, 0.35)$.

Uniaxial tensile tests are applied on the samples in serial coupling conditions at $T = 0.3$. To compare the results, the tensile velocity was adjusted for each sample in a way that all samples will be submitted to the same initial strain rate ($\dot{\varepsilon}_{zz} = 7.2 \times 10^{-5}$). The mechanical responses were plotted and compared as shown in figure 4.14 The correlation between the mechanical and the evolution of local structure was already presented in section 4.4. In the elastic regime all samples have roughly the same elastic modulus. The yield stress increases as the proportion of bridging molecules increases. In this case the nucleation and the development of cavities in the rubber are constrained by the entanglements that make the cavitation energetically expensive. This is also consistent with the fast stress drops at cavitation occurring in the soft phases of weakly bridged samples (see the log scale curves in figure 4.14.b). compared to a smooth stress softening in well connected samples.

After the cavitation the sample exhibits a strain hardening regime. It was experimentally demonstrated that the growth of stress in the strain hardening regime depends on the entanglement density and then the rate of bridging molecule. This behavior is shown by the stress-strain curve. Note that the behavior in log scale shows two strain hardening that are distinguished by two different stress growth rates. The transition between the two regimes is located at true strain $\varepsilon_{zz} = 1$. Indeed the first growth of stress in assigned to the strain hardening in the rub-

6. In semi crystalline polymer such like PolyEthylene the same material is present in two forms : hard crystal and soft rubber. the rubbery phase is confined between the crystalline phase [Humbert 2009]. The equatorial part of the spherulite is close to serial coupling behavior.

7. with glassy, rubbery and semi crystalline phase

ber where the deformation takes place at low strain. At a strain equal to 100% we have shown that the soft phase becomes stretched enough to activate the plastic deformation of the glassy phase. When the number of bridging chains decreases, the stress transmission between phases becomes localized in the vicinity of the bridging chains at the interface. This stress concentration weakens the sample and the stress at which the hard phase begins to deform is reduced. As the deformation of the rubber is saturated at $\varepsilon_{zz} = 1$, the second strain hardening regime depends on the deformation of the glassy phase.

Note that the decrease of stress growth in the second strain hardening regime, is more pronounced in weakly bridged samples. This phenomenon can be assigned to the glassy chain pullout that becomes effective in the glassy block of weakly bridged samples. Indeed, the stress is localised only on few bridging chains. Therefore, the pullout events are favored. The consequence is the relaxation of the bridging chain, which reduces the local deformation of the glassy layer (figure 4.15) and the stress growth is then reduced.

For the sample S^c_{100}, all chains are cut there are no bridging chains in the soft phase [8], therefore the sample in this case can be considered as two diblock samples that join each other in the soft phase. In the tensile test the sample breaks in two parts just after the first cavitation in the soft block. This behavior is obviously expected as the soft phase is already weak and unentangled. The failure in all other samples still occurs in the hard glassy block.

We can relate these observations with the work of reference [Monasse 2008]. In this work an atomistic description of a semi crystalline polymer was used to simulate its mechanical response. The onset of the crystalline phase damage begins where the chain in the amorphous phase becomes stretched. In this model, the chain lengths are distributed, and the stretching starts effectively when the shortest chains becomes stretched. In our work, a statistical distribution of effective chain lengths [9] is created indirectly and is modified by the proportion of cut chains. Even though all bridging chains have the same length, they are not all stretched simultaneously, since the path of each bridge in the soft phase is different due to entanglements and anchoring positions in the glassy phases. The decrease of the entanglement density in weakly bridged samples increases the effective chain length and therefore delays the onset of the hard phase deformation. (see the inset of the figure 4.15 for more details).

The influence of the rate of bridging molecule on the deformation of the hard phase was also studied. The deformation of the hard blocks was probed for all samples using the density profile (equation 4.3). The results are plotted and compared as shown in figure 4.15.

The growth of glassy block strain is more pronounced in the well bridged samples. This behavior results from the homogenous distribution of stress in the hard block. In weakly bridged samples the deformation of the hard phase starts by chain pull

8. all chains have 50 beads in both glassy and the rubbery phase.

9. The effective length is the length between the bridging chain ends of the soft phase measured in stretched chains.

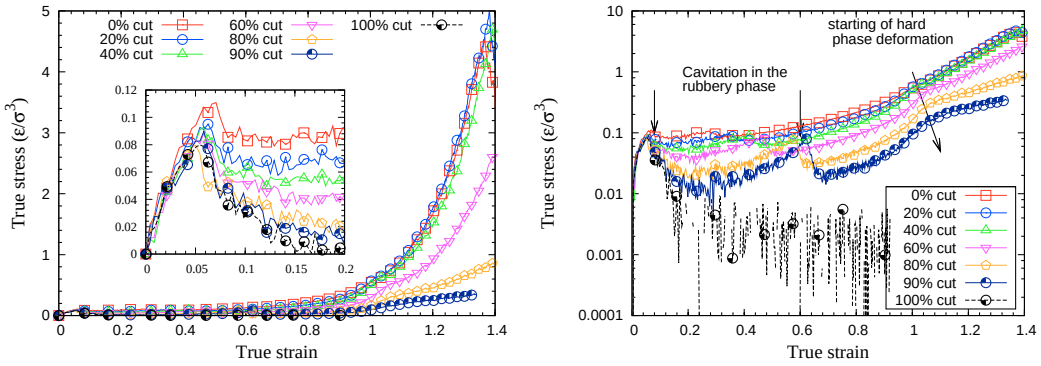

(a) (b)

FIGURE 4.14 – (a) Comparison between the mechanical response of several samples with different rates of cilia molecules, the other chains are bridging molecules. The LJ energies are as follows : $\varepsilon_{AA} = 1$, $\varepsilon_{BB} = 0.2$ and $\varepsilon_{AB} = 0.35$. Inset : zoom on the elastic an the yield part of the curves. (b) Log scale plot (same as in (a)) to emphasize the influence of the cilia chain on the strain hardening regime.

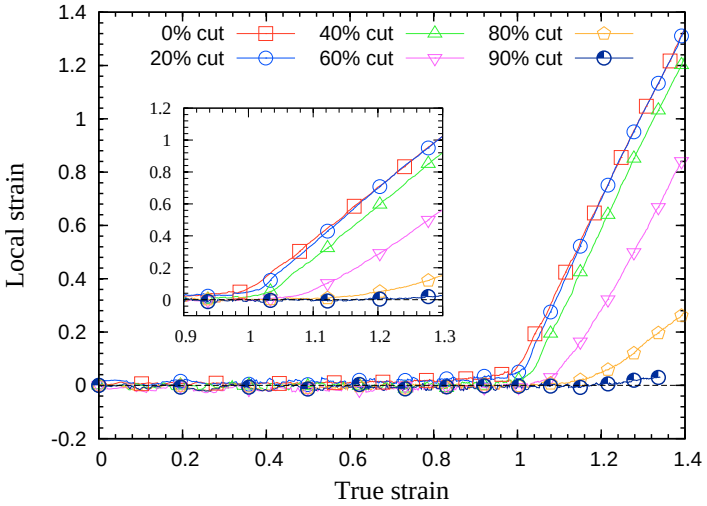

FIGURE 4.15 – Hard phase deformation of several samples with different proportions of cut chains.

out as described previously, which reduces notably the deformation of the hard block. As the number of bridging molecules decreases the strain at which the glassy phase starts to deform increases. This trend is interpreted by the increase of the effective length of the bridging chains that results from the loss of entanglement in low bridged sample.

In fact, the deformation of the glassy block in a well bridged sample exhibits a "ductile-like" behavior. The glassy phase is well deformed before the ultimate damage (basically caused by chain disentanglement). On the other hand, the weakly bridged sample shows a completely different behavior, the fracture occurs in the glass phase even if the latter is not strongly deformed. This behavior is closer to a brittle behavior. The influence of the bridging molecules on the copolymer mechanical response was studied in the experimental work of Hermel *et al.* [Hermel 2003]. The amount of bridging molecules was experimentally varied by mixing the a CEC triblock with CECEC pentablock copolymer. A ductile-brittle behavior transition was evidenced when the rate of bridging molecules becomes less than 15%.

4.5.2 Influence of loop molecules

As suggested by Wu *et al.* [Wu 2004], the formation of the loop chains in block copolymer is favored by the processing factors that are used to align the triblock systems : low shear rate and large strain amplitude favors layer by layer sliding, which drivse predominantly looping conformation. In this section, we study the influence of loop chain conformations on the mechanical response of lamellar systems. Several samples with different amounts of loop chains were build as described in the Appendix A. (S_0^l, S_{40}^l, S_{80}^l and S_{100}^l). The other chains are bridging chains. All samples have the same interaction energy (1,0.2,0.35). Uniaxial tensile tests were applied, the test conditions are the same as in section 4.4.The same initial strain rate is used for all samples.

The stress-strain curves are plotted and compared in figure 4.16. All samples exhibit similar mechanical regimes and the stress-strain curves superimpose rather well, especially before the onset of the hard phase deformation regime. (triggered at $\varepsilon_{zz} \approx 1$). The inset in figure 4.16 magnifies the elastic regime of the curves. all samples have the same elastic slope and roughly the same cavitation strain (except of S_0^l). In the second strain hardening regime, the growth of stress seems to be affected by the amount of loop chains. The increase in the number of loop chains number slightly decreases the stress growth. Therefore, the samples are less affected by the change of the bridging chain amount in the loop chain samples than in the cut chain sample. (The difference on the behavior can be clearly distinguished by comparing the extreme cases of cut and loop samples : S_{100}^l and S_{100}^c both sample have 0% bridging molecules but the behavior of the two samples are very different). This behavior is interpreted by the fact that the loop chains grafted in the first hard block have enough length to entangle with other loop chains coming from the second hard block. For this reason, two knotted loop chain are effectively equivalent to two bridging chains. Therefore, the decrease of bridging molecules to give loop molecules

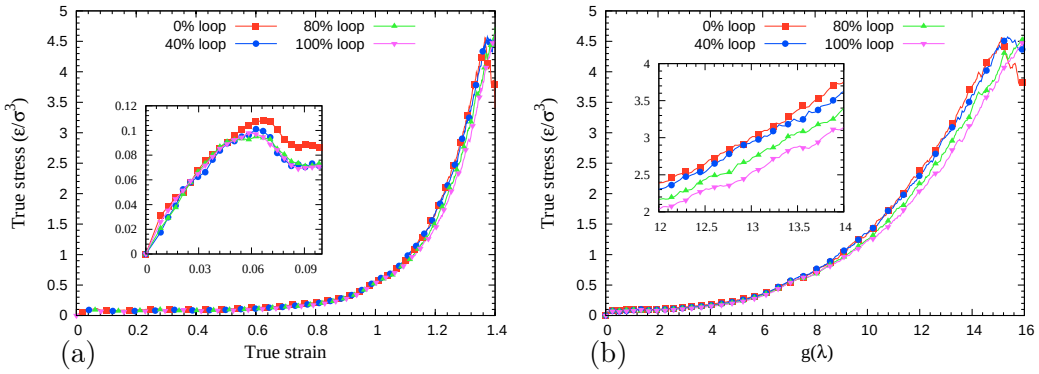

FIGURE 4.16 – (a) Comparison between the mechanical response of different samples with different number of loop chains. The inset shows a zoom in the elastic regime and yield point region. (b) Stress with respect to the strain hardening function $g(\lambda) = \lambda^2 - 1/\lambda$. A zoom to clarify the order of the curves in the strain hardening is shown in the inset.

does not affect the mechanical behavior of the sample, as the cut chains do. This phenomenon was reported in the work of Mori *et al.* [Mori 2003], who demonstrate the presence of knotted loop chains that ensure the bridging of CECEC pentablock copolymer.

4.5.3 PPA of the rubbery phase in 100% loop chain sample

The equivalence between knotted loop chain and bridging chain architecture was verified. Primitive Path Algorithm (PPA) was applied on the soft phase of S^l_{100} in order to explicit the chain entanglements. The algorithm has been detailed in section 2.2.1. Note that all the hard blocks are treated as the chain end in this case. The glassy portions of the chains are frozen during the algorithm and only the soft phase is submitted to the length reduction process. If a loop chain is not entangled with any other chains, after the PPA this chain will be a straight segment. In the other case, the entangled chain will be segmented into $n+1$ straight fragment for n entanglements. After the convergence of the PPA, the configuration was inspected. As shown in figure 4.17, nearly all of the loop chains that are implanted in the first glassy block form at least one entanglement with another loop chain coming from the second glassy block.

A negligible number of loop chains are still unentangled ($\approx$ 20 loop chains from the entire 320 chains). This observation confirms the previous assumption about the bridging role of the loop chains in the tensile test experiment. This behavior is obtained only when the loop length is sufficiently long to entangle the other loop chains. This is not necessarily the case for the semi crystalline PolyEthylene where the loops in the rubbery phase are extremely short [10]. In such cases the presence of

10. the length of the loop chain in PE do not exceed the straight jump from a chain to another

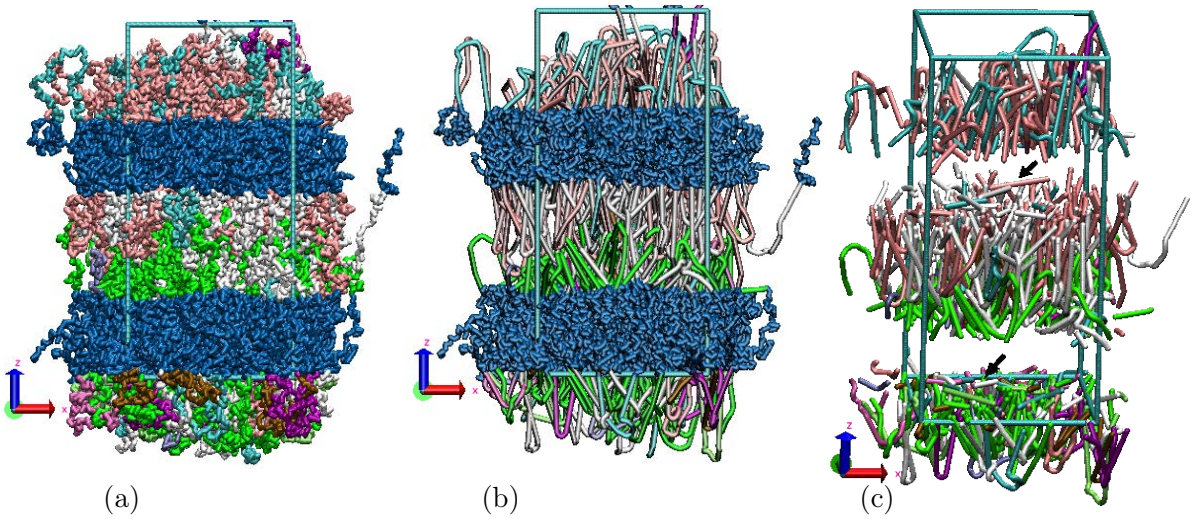

(a) (b) (c)

FIGURE 4.17 – (a) Triblock sample with 100% loop chains before PPA chains are unwrapped over the periodic boundary conditions. (b) the same sample after the convergence of the PPA in the soft phase (the hard phase -colorized blue- still frozen in the PPA process). The loop chains are well entangled in a way that bridges the hard blocks together. Only a negligible number of loop chain are still unentangled as shown in figure (c) (The hard blocks were hidden in this figure).

the loop conformation weakens the sample by suppressing some stress transmitters between phases in the same way as the influence of cut chains. Consistent results were found in reference [Léonforte 2010] who performed the same analysis on similar systems. However, in the latter work the mechanical response was found to display a stronger dependence on the proportion of loop chains than in our simulations. This difference comes probably from the LJ potential energies chosen to drive the segregation, which are (1,0.5,0.01) in reference [Léonforte 2010] compared to (1,0.2,0.35) used in our work. A strong difference in the AB interaction energy can sensitively modify the mechanical behavior, as illustrated in the next section.

4.6 Influence of surface energy

In the previous sections we have shown the influence of coupling that results from the bridging between phases. This bridging is ensured by two kinds of chain conformations : the knotted loop chains, and the bridging chains. At high strain, the role of these chains becomes significant in the transmission of stress between phases. At low strain the process is completely different, the transmission of the stress between phases is ensured by the LJ interaction between phases. Therefore, a good coupling is ensured by a strong adhesion between phases in contrast a weak coupling leads to weak interface. In this section, the role of the wetting energy on the mechanical response is investigated. Three samples with different ε_{AB} were submit-

in the crystal

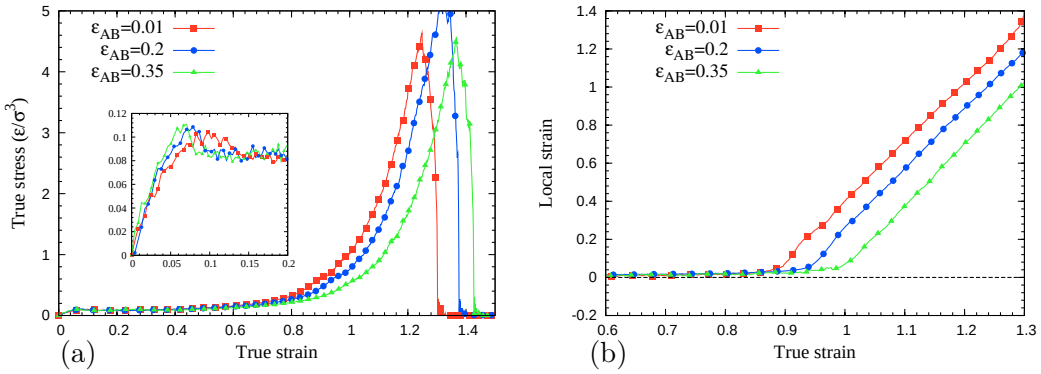

FIGURE 4.18 – (a) stress strain curve showing the influence of the surface tension between the hard and the soft phases. The intrablock interaction $\varepsilon_{AA} = 1$, $\varepsilon_{BB} = 0.2$ are fixed, only the inter-block interaction ε_{BB} is modified.(b) Hard phase strain of the same systems.

ted to uniaxial tensile strain conditions perpendicular to the block orientation. The LJ of the hard and the soft phases are kept the same for all sample, which leads to a change on the segregation parameter $\tilde{\varepsilon}N$. The LJ energies $(\varepsilon_{AA}, \varepsilon_{BB}, \varepsilon_{AB})$ of the samples are (1,0.2,0.35) , (1,0.2,0.2) and (1,0.2,0.01). for the first kind of tests, which corresponds to a $\tilde{\varepsilon}N$ of 166, 400, respectively. The second kind of tests is performed on the samples of (1,0.5,0.5) , (1,0.5,0.25) and (1,0.5,0.01). The corresponding $\tilde{\varepsilon}N$ are 166, 333, 490.

These two values of the LJ energy were selected to describe the high segregation limits where $\tilde{\varepsilon}N \gg 20$ [Perez 2008] with two different deformation states : (i) the localized deformation for the first one and (ii) the homogenous deformation for the second one.

The mechanical responses of the first kind of sample are shown in figure 4.18. A small change in the elastic slope is remarked in the first quasi linear regime. The decrease of ε_{AB} will soften the elastic response of the sample. This trend can be explained as the decrease of adhesion strength leads to an interface that behaves as an additional weak phase (called also interphase) in serial coupling.

The density at the interface were probed using the Voronoi volume of beads as shown in figure 4.20. The interface is located between the bead numbers 50-51 and 150-151 [11]. At the interface, the mean Voronoi volume becomes remarkably high for the lowest ε_{AB} sample. This local decrease of density should favor the nucleation of cavities at the interface, which reduces the strength of the system. In the inset of figure 4.18 the cavitation stresses and strains seems to be affected by the change of ε_{AB} since the soft phase ((1,0.2,0.35) sample at (T=0.3)) is a very weak rubber. The influence of interface on the cavitation is much clearer in the second range of tests (discussed below). Note that in the previous analysis, we have used the Voronoi

11. A triblock chain is composed as follows : 50 beads glassy, 100 beads rubbery, 50 beads glassy.

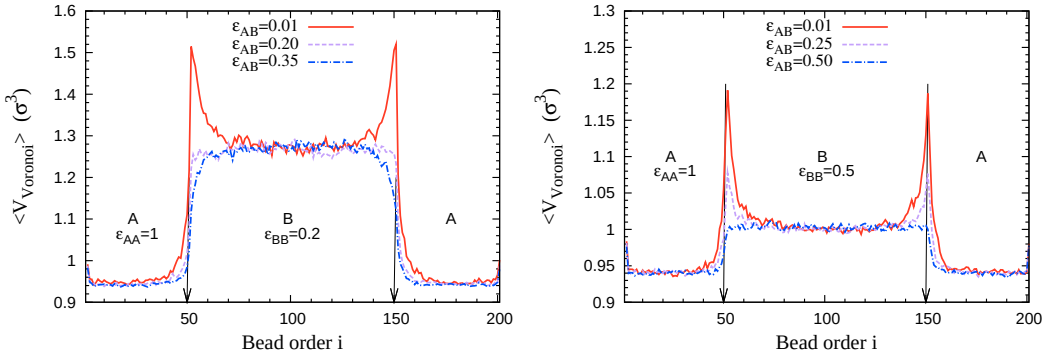

(a) (b)

FIGURE 4.19 – Mean Voronoi volume of chain beads presented with respect to the bead order in the chain. A triblock is split as follows : 50 beads glassy (labeled A) followed by 100 beads rubbery (or soft labeled B) and the rest is 50 beads glassy. The total number of beads per chain is 200. $i = 1$ and $i = 200$ present consecutively the first and the last beads in the chain (chain ends), the glass-rubber interface is located between the bead couple indexed by 51-52 and 150-151.

volume to measure the interface density, because it is more precise than the density profile evaluated by the scanning probe method. Additionally, the Voronoi method can be applied to a non planar interface, which in not the case for the second method.

Surprisingly, the strain hardening regime is significantly affected by the change of the interface properties. The decrease of ε_{AB} increases the stress growth in the second strain hardening regime that corresponds the deformation of the hard phase. In addition, The decrease of ε_{AB} also decreases the onset of the hard phase deformation. Both observations correlate with the segregation state determined by the choice of ε_{AB}. The smallest value of ε_{AB} leads to a strongly segregated phase. The LJ interactions in such case, tend to minimize the interface between the hard and soft phases, a consequence is the increase the soft phase length [12]. The chain conformation in the rubber becomes more oriented in this case, which leads to a pre-aligned bridging chain in the soft phase. When tensile strain is applied, the orientation of soft block chains is partially achieved by segregation state, therefore the required strain to trigger the hard phase deformation in the pre-oriented sample is lower than the one for other samples. In other words, a typical sample needs more strain to achieve the full deformation of the soft phase in the normal direction compared to pre-oriented sample. For this reason the onset of the hard phase deformation is delayed as well as the strain hardening for the higher ε_{AB} samples.

For the second kind of tests (1,0.5,0.5) , (1,0.5,0.25) and (1,0.5,0.01) samples, we have shown in section 4.4.1 that at this value of ε_{BB} both hard and soft phases deform homogeneously when the sample is submitted to a uniaxial tensile strain condition. The role of the interface on the mechanical behavior of these samples

12. the spacing between two hard phases.

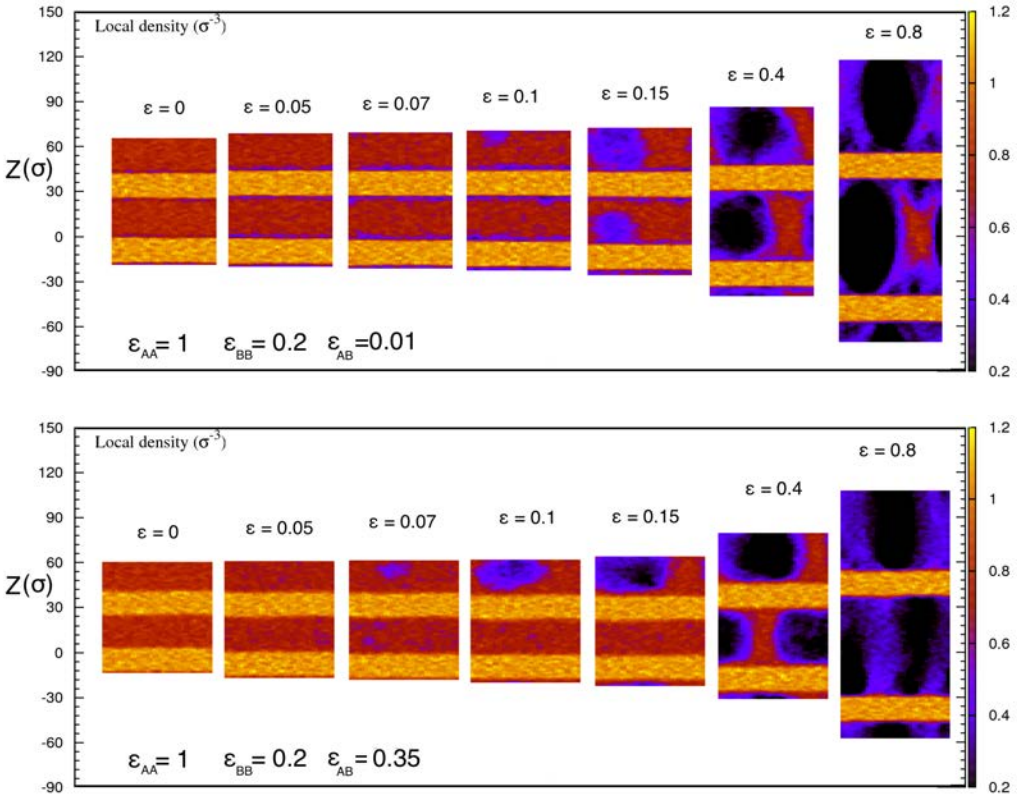

FIGURE 4.20 – Color maps showing the evolution of the local density in two samples with two different surface tension energies. The cavities nucleate preferentially at the interface when the adhesion between phases is very low (upper panels). The cavitation at the interface is avoided when ε_{AB} is high as shown in the lower panels .

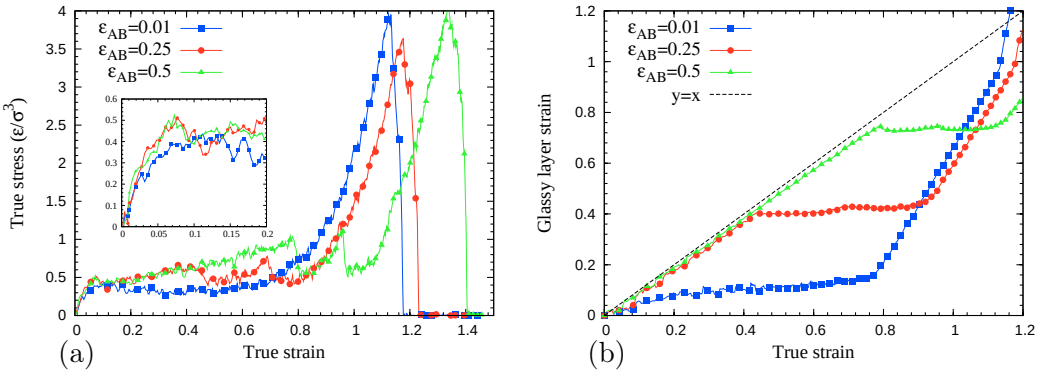

FIGURE 4.21 – Stress/strain curves with ε_{BB} taken equal to 0.5, (a) the stress strain curves with various ε_{AB}.(b) the strain of the hard phase.

has been investigated in the same manner. The mechanical response are displayed in figure 4.21. These observations of the stress-strain response is coupled with the measure of the hard phase deformation (plotted in 4.21.b). The mechanical response of the first sample was detailed in section 4.4.1. The second sample (1,0.5,0.25) exhibits approximately the same behavior until a true strain of $\varepsilon_{zz} = 0.4$ where the drop of stress marks the nucleation of the cavities in the rubber. The evolution of the hard phase deformation shows that the first two samples deform homogeneously before the cavitation. Therefore the stress softening after the elastic regimes corresponds to the yielding in the hard phase. The behavior of the third sample with the smallest ε_{AB} is completely different. There are no stress drops in the stress-strain curve except at yield. The evolution of the hard phase deformation indicates the localization of strain in the soft phase (The deformation of the hard phase is very small). Therefore the stress softening corresponds in this case to the cavitation in the rubber. Referring to the distribution of Voronoi volume on the chain 4.20, the Voronoi volume of the interface beads increases with decreasing ε_{AB}. Therefore the local density at the interface is very low for the smallest ε_{AB} sample, thus the cavities nucleates preferentially at the interface in this case. Note that in second kind of tests, the cavitation strain of the soft phase decreases as the ε_{AB} increases. The results in this section depend on the strain rate used to drive the tensile test. This point is not yet investigated, and further tests are planned for this purpose.

4.7 Conclusions

In this chapter, the mechanical response of a layered block copolymer was investigated using a generic coarse grained model. Radical like polymerization method was used to generate a nano-structured system. After the generation the systems were submitted to a long equilibration-segregation stage. To obtain a nano-structured system with an alternate glassy-rubbery phase, the samples are cooled to a conve-

nient temperature at which the tensile tests are performed. These samples were submitted to uniaxial tensile strain condition in two directions : normal to the block and parallel to the block. In the perpendicular direction the constitutive blocks are coupled in serial. Depending on the choice of the LJ interaction of the soft phase, two deformation modes were distinguished in this case. (i) The localized deformation : at low ε_{BB} the global deformation will be localized in the soft phase, the hard phase remains undeformed. The yield in this case corresponds to the cavitation in the rubber. At hight strain the hard phase starts to deform since the soft phase becomes stretched enough. (ii) The homogenous deformation appears at high ε_{BB}. The two blocks hard and soft deforms homogeneously in this case, and the yield corresponds to the deformation of the glassy phase. In parallel coupling the mechanical response of the system is governed by the behavior of the hard phase. The impact of the chain architectures and conformations on the mechanical response of triblock has been approached. Several samples with different amounts of cut and loop chain were tested. The presence of the cut chains in the samples reduces their mechanical properties. The elastic slope and the strain hardening of the samples decrease remarkably as the proportion of cut chains increases. This behavior is correlated with the loss of entanglement, and stress concentrations that weaken the hard phase at high strain. In contrast, loop chains in the sample were found to be equivalent to bridging molecules. Indeed, a loop chain originating from one hard block is sufficiently long to entangle with other loop chains coming from the second block. Therefore the knotted loop chains ensure the stress transmission between blocks in the same manner as the bridging molecule. This observation was also verified by doing the PPA on the soft phase of loop chains system.

The role of the interface strength on the mechanical response of triblock was also investigated by tuning the surface tension ε_{AB}. The two previous cases : localized and homogenous deformations were considered. For the first case, we find that the influence of ε_{AB} is not significant on the elastic properties and the cavitation strain. The onset of hard phase deformation decreases as ε_{AB} decrease. This trend was correlated to the pre-oriented chain conformation that will become more pronounced as the segregation becomes strong.

For the second case (homogenous deformation), reducing the surface energy for the interface will reduce the cavitation strain, at extremely weak interface the nucleation of cavities becomes localized at the interface, which decrease remarkably the deformation of the hard phase.

The influence of strain rate on the mechanical response is not yet investigated. The question about the role of the strain rate becomes relevant since the local behavior rubbery phase is a strain rate dependent. The homogenous deformation of (1,0.5,0.5) sample in serial coupling is well interpreted by the homogeneity of the local elastic response of each phase but is this behavior still observed at low strain rate ? This remains an open question that needs more investigations.

Chapitre 5

Buckling instability in lamellar block copolymer

Contents

5.1 Introduction

Multiblock copolymers exhibit a composite mechanical response that depends sensitively upon their constituent homopolymers segments, molecular architecture and chain topology. Triblock copolymer have become an attractive material for their use as thermoplastic elastomers that could be integrated in several technical and manufactural fields. (*e.g* : copolymer styrene butadiene rubber is commercially exploited in footwear, in pressure sensitive adhesive (K-Resine), in paving and roofing compounds.) Depending on the amount of each phase the segregated block copolymers may present several morphologies : spherical,cylindrical, gyroidal and lamellar. The lamellar morphologies have attracted much interest for several reasons : (i) well

aligned specimen can be experimentally generated by shearing, (ii) structure - property correlation is simplified due to the one dimensional structural geometry, and (iii) lamellae reveal the mechanical contribution from each component while other classical morphologies (cylinders, spheres) tend to be dominated by the majority (matrix) phase. In these copolymer systems one of the constituent polymers (typically the minority component) is glassy and the other one is rubbery. [1] A single copolymer chain can be shared between two different glassy lamellae, forming a rubber bridge that provides a strong coupling between phases. The resulting system combines the stiffness of the hard glassy phase and the ductility of the soft rubbery phase.

When a lamellar copolymer sample is submitted to a tensile strain perpendicular to the plate (layers), the glassy layer eventually buckles into a "chevron" morphology. With increasing strain the normal to the lamellae tilts away from the stretching direction, whereas the lamellar spacing remains almost constant. This behavior was demonstrated experimentally in triblocks by Small Angle Xray Scattering (SAXS) under deformation, and by micrographs of strongly deformed samples. In SAXS, the evolution of the morphology under tensile strain condition has been extensively studied. it is characterized by the evolution from a pattern with two symmetrical spots for a perfectly aligned sample towards a four-point pattern that characterize the chevron morphology and starts appearing at the yield point.

This buckling instability under strain, which is observed in many layered materials from smectic liquid crystals to geological layers, was frequently described in a qualitative way by a preference to shear compared to an extension in the direction normal to the layers, in order to preserve the lamellar spacing. A different cause for buckling is the existence of a Poisson effect, with the soft phase taking most of the imposed deformation, and exerting a compressive stress in the transverse direction that causes the buckling of the hard phase. In this chapter, we will use the ability of molecular dynamics simulations to give information on the local values of stresses and strains to explore the causes of the instability in triblock copolymers with alternating glassy and rubbery layers, without introducing an a priori description of the mechanism, as would be the case in Self consistent field or finite element modeling. To our knowledge, this is the first observation and study of this instability in molecular dynamics simulations. In order to achieve this study, several challenges had to be addressed. Large samples will have to be used, and the parameters must be optimized to allow the observation of buckling within the conditions of a molecular dynamics simulation.

We begin the discussion with a fast review of existing literature. Next we discuss qualitatively the observations made in MD simulations. Section 4 describes the modeling of buckling developed by Read *et al* [Read 1999] using elasticity theory. We then explore the influence of several factors such as sample size and strain rate. The results are analyzed and discussed in relation to the elastic theory of Read *et*

1. Another possibility which will not be examined here is a glassy phase coupled with a semi crystalline phase.

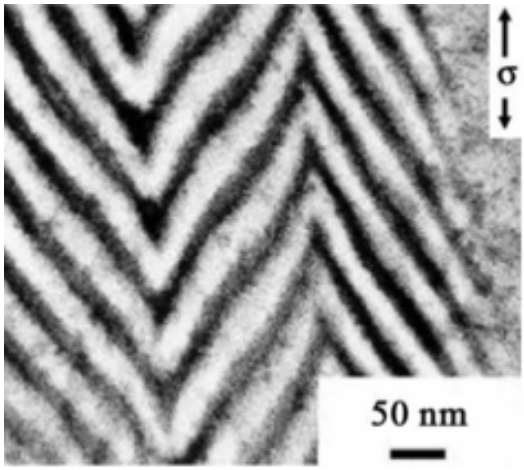

FIGURE 5.1 – A Transmission Electron Microscopy (TEM) image showing the morphology of the buckled state of SBS (Styrene-Butadiene-Styrene) rubber, the tensile direction is shown in the small top right inset. figure reproduced from [Adhikari 2004].

al in the last part of this chapter.

5.2 A short review of experimental results

The response of lamellar block copolymers has been extensively studied in the past few decades in order correlate their mechanical properties with the local morphology and the micro-structural characteristics of the sample. To obtain a regular layered morphology over large sizes in experimental studies, the block copolymer is submitted to an oscillating shear applied during the casting process [Cohen 2001]. Cohen *et. al* [Cohen 2000] has reported a detailed study of the micro-structural transitions during deformation of highly ordered lamellar SBS films at different angles of the applied force with respect to the lamellae. In particular force applied parallel to the lamellar normal was shown to cause folding of the layer into a "chevron" morphology (figure 5.1).

Many other layered systems are found to exhibit a similar behavior, these systems range from the smectic phase of liquid crystal [de Gennes 1993], to micron scale stripped pattern in magnetic films [Seul 1992] and to macroscopic geological formations [Ramsay 1987]. An extensive finite element simulation study was made by Read *et al* [Read 1999] has predicted the buckling strain based on the elastic properties of the layered structure. In such approach, the buckling is expected when the gain in elastic energy overwhelms the bending energy penalty of the hard phase.

The evolution of the local morphology of lamellar block copolymer under perpendicular tensile strain experiment was inspected by *in situ* Small Angle X-ray Scattering (SAXS) technique in [Thomas 2001].

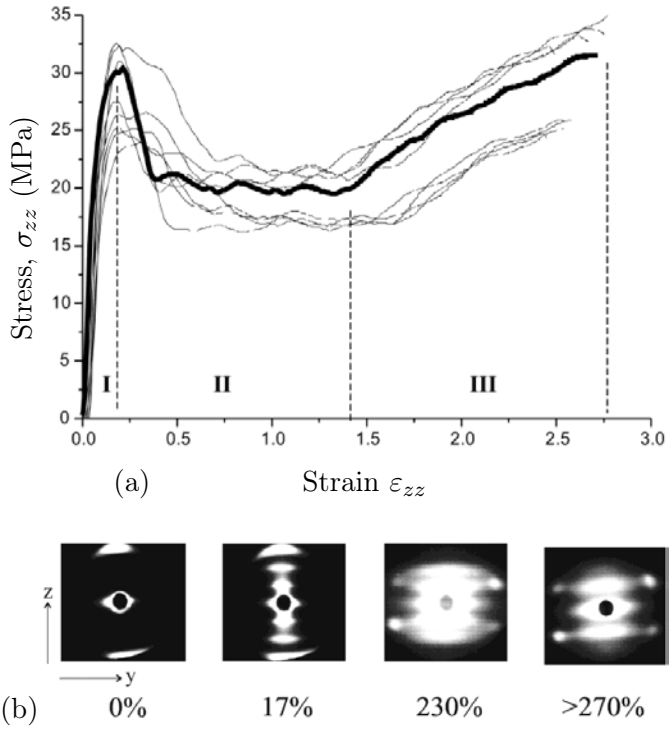

FIGURE 5.2 – (a) Stress strain curve of an aligned CECEC pentablock copolymer, the uniaxial strain was applied perpendicular to the block orientation. (b) SAXS pattern taken with X-ray beam directed perpendicular to the tensile direction during the tensile extension test. (figure reproduced from [Hermel 2003])

The evolution of the SAXS pattern was related to the mechanical response as shown in figure 5.2 for glassy/semi crystalline block copolymer (C and E denote respectively Poly-CycloHexylEthylene and PolyEthylene).The corresponding data, reproduced from [Hermel 2003], is shown in figure 5.2 . The mechanical response shows several regimes, (i) the linear elastic regime, (ii) the necking and (iii) is the strain hardening regime. The first SAXS pattern for the unstrained state shows two reflections that result from the periodic aligned lamellae morphology with lattice spacing d_0. The small bending of the SAXS reflections in the initial undeformed sample was attributed to the small morphological defects such as layer tilting with respect to the main alignment direction [Thomas 2001]. The application of the reversible strain in in the elastic regime (i) leads to two pairs of additional reflections, consistent with a new spacing at $d = 2.9d_0$. Necking (ii) and strain hardening (iii) transforms the SAXS pattern creating considerable low angle scattering intensity and four new reflections. This irreversible transition persists through failure. The new spacing signature observed in the elastic regime results from the localization of strain in some lamellae (preferentially in some SC lamellae), which leads to cavitation and drawing within a subset of PolyEthylene (E) domains. In the necking and the strain hardening regimes the buckling of lamella can be distinguished by the four spots of the SAXS patterns. The proposed failure mechanism is shown in figure 5.3.b . Note that several studies in glassy/semi-crystalline lamellar block copolymer indicate the development of the cavitation in parallel to the buckling [Hermel 2003, Mori 2003]. This observation deduced from the whitening of the SAXS spots was verified by the Transmission Electron Microscopy TEM images, as shown in figure 5.3.a .

A similar but not identical behavior was found in aligned the S-B-S triblock where the structure is consistent with an alternating is glassy-rubbery blocks. When the tensile is applied perpendicular to the lamellar direction, the elastic response results from the dilatation of the soft phase [Cohen 2000] (see figure 5.4). The smooth decrease of stress growth at yield is correlated with the onset of lamella buckling, detected by the bending of SAXS pattern.The development of buckling from an undulation to "chevron" morphology leads to four symmetrical spots in the SAXS reflection. The evolution lamellae tilting after the buckling can be followed *in situ* by measuring the Azimuthal angle of the SAXS pattern as it done several works [Wu 2004, Phatak 2006, Mahanthappa 2008]. The development of buckling is achieved in the drawing regime before the ultimate failure. Cohen and Thomas have compared the apparent elongation estimated from the azimuthal angle and the total elongation of SBS sample submitted to a perpendicular tensile stain. A large difference was found at low strain. This difference was interpreted by the role of pre-existing defects that nucleate tilt grain boundaries at low strain. [Cohen 2003].

The influence of the processing variable on the chain architecture of lamellar block copolymer has been studied : Wu et al have demonstrated that the phase orientation and molecular architecture (the amount of the loop molecules against the bridge chains) depends severely upon the amplitude and the frequency of the applied oscillatory shear (the study was performed on a Styrene Isoprene copoly-

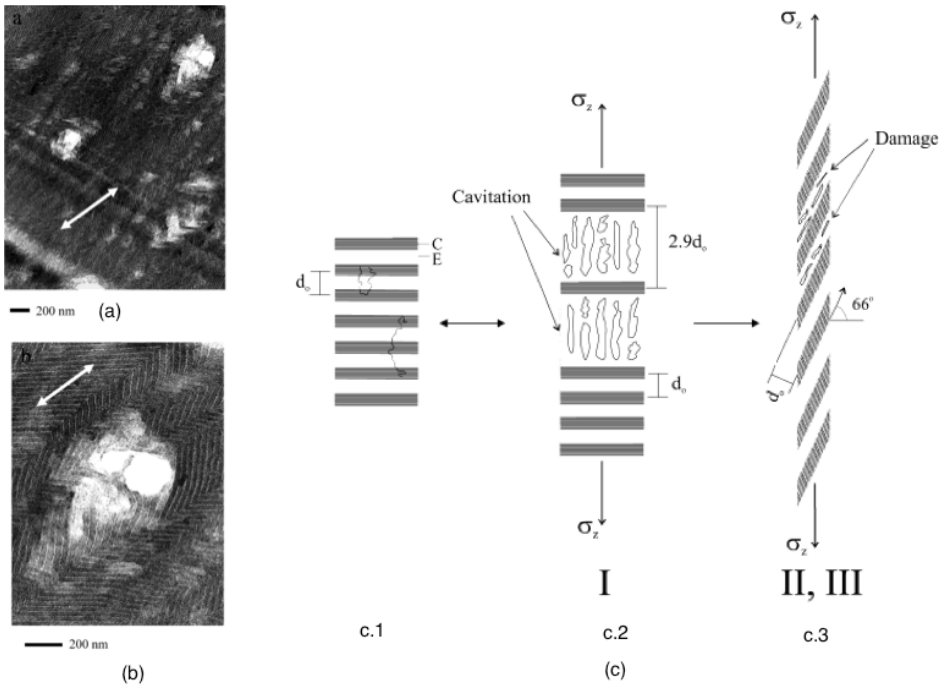

FIGURE 5.3 – (a) and (b)TEM images obtained from the section of a mixture of triblock CEC and pentablock CECEC, taken after the failure under tensile strain. The tensile direction is indicated by the white arrows. The white spots are attributed to the formation of voids during necking and drawing. (reproduced from [Mori 2003]) (c) proposed pentablock failure mechanism (c1) tensile deformation of an aligned monodomain lamellae specimen results in cavitation and drawing (c2) within the softer domain. Additional strain leads to a buckling instability in (c3) [Hermel 2003].

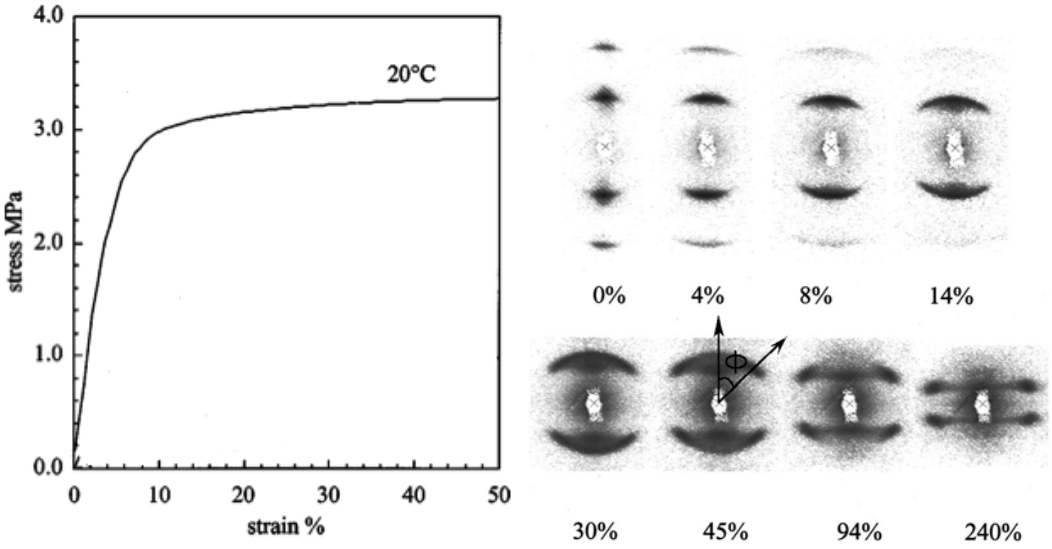

(a) (b)

FIGURE 5.4 – (a) stress-strain curves (engineering units) of oriented SBS lamellar sample undergoing perpendicular deformation at ambient temperature. The evolution of SAXS patterns during the test is shown in (b), the "Chevron" angle is correlated with the azimuthal angle Φ. (figure reproduced from [Cohen 2001].)

mer). [Wu 2004]. This observation was verified later by a molecular dynamic study [Guo 2006]. The role of the molecular architecture in the mechanical response of oriented lamellar copolymer has been studied. A fast transition from ductile to brittle behavior was observed by Bates and coworkers [Mori 2003]. This transition is achieved when the bridging chains (pentablock CECEC chains) reach 15% of the total amount of chains (the other chains are triblock CEC chains). A similar result was found in references [Phatak 2006, Lim 2005] in which the tensile strength and the toughness of aligned copolymer sample are directly correlated with the amount of bridging chains.

5.3 Overview of observations made in MD simulations

5.3.1 Microscopic analysis of the mechanical response in a small system

When a multilayered system is stretched perpendicularly to the layer direction, each component of the system will deform according to its own stiffness. Then locally, the deformation will be distributed between phases in a way that ensures the continuity of the stress. The resulting macroscale deformation is the sum of the local strain response of each phase and the composite stiffness will be dominated by the response of the soft phase. The multiblock copolymers exhibit a similar mechanical response when the a tensile strain is applied in the perpendicular direction. Due to the serial coupling between the glassy and rubbery phases the tensile strain will

be mainly localized in the rubbery lamellae. As we have shown in the first chapter, the Poisson ratio of the rubbery phase is relatively high compared to the one of the glassy phase (at $T = 0.5$ and $\varepsilon_{AA} = 1$ $\nu_{rubbery} \simeq 0.5$ while at $T = 0..2$ $\nu_{glassy} \simeq 0.4$ for the same interatomic interaction). Then at the same strain, the rubbery phase contracts more than the glassy phase in the lateral direction if no coupling exists.

In multiblock copolymers, the coupling between phases is ensured by two interactions : (i) the bonded interaction that bridges the two phases together (ii) the non specific bond interaction that controls the wetting and the segregation state of phases. At low strain the stress transmission between phases will be ensured by the non specific bonds ; however, the bonds are more effective at high strain.

Due to the Poisson effect, the perpendicular tensile in layered copolymer will be converted locally to a contraction in the lateral dimension. The lateral contraction is more pronounced in the rubbery phase, due to the larger deformation and the higher Poisson ratio. As the two phases glassy and rubbery are strongly coupled by both interactions, the lateral contraction of the rubbery phase will be transmitted to the glassy one via the interface. The glassy phase becomes submitted to a tensile stress in the perpendicular direction and a compressive stress laterally. Under these conditions, and for a sufficiently large system, a buckling instability takes place to relax the lateral compressive stress.

This scenario can be checked qualitatively by monitoring the local stress in a sample strained perpendicularly to the lamellae. Figure 5.5.a shows the lateral stress ($\frac{\sigma_{xx}+\sigma_{yy}}{2}$) profile (along the z direction) of a stretched copolymer sample at a true strain $\varepsilon_{zz} = 0.04$. The average pressure in these directions (x and y) was set to zero, as uniaxial tensile conditions are imposed globally. In order to distinguish each phase the density profile is also plotted (secondary vertical axis). The glassy phase is characterized by the higher density, compared to the rubbery phase. As shown the lateral stress is positive in the rubbery phase while it is negative in the glassy phase, indicating a local compression parallel to the glassy lamellae.

The spatial distribution of the lateral stress is also shown in figure 5.5.b. As in figure 5.5.a the negative stress corresponds to glassy regions. The stress in these figures was probed in a relatively small sample ($L_x = 34.5\sigma \times L_y = 102.3\sigma \times L_z = 34.5\sigma$) in which buckling is not observed, however the analysis of the stress profile clearly shows the importance of the Poisson effect. The influence of sample dimension is discussed below.

Lateral force and segregation state : The evolution of the lateral compressive force acting upon the glassy layer is shown in figure 5.6 where the sample is submitted to a uniaxial tensile test at constant strain rate ($\dot{\varepsilon}_{zz} = 7.3 \times 10^{-5}$). Several segregation parameters were tested, all of them are chosen to have one of the constituents glassy and the other rubbery at the temperature of the test, $k_BT = 0.3\varepsilon$. As discussed below, the simulation of the buckling necessitates a very large specimen which increases massively the computation time. so that the choice of interaction parameters that favor buckling is important. A convenient situation is one in which

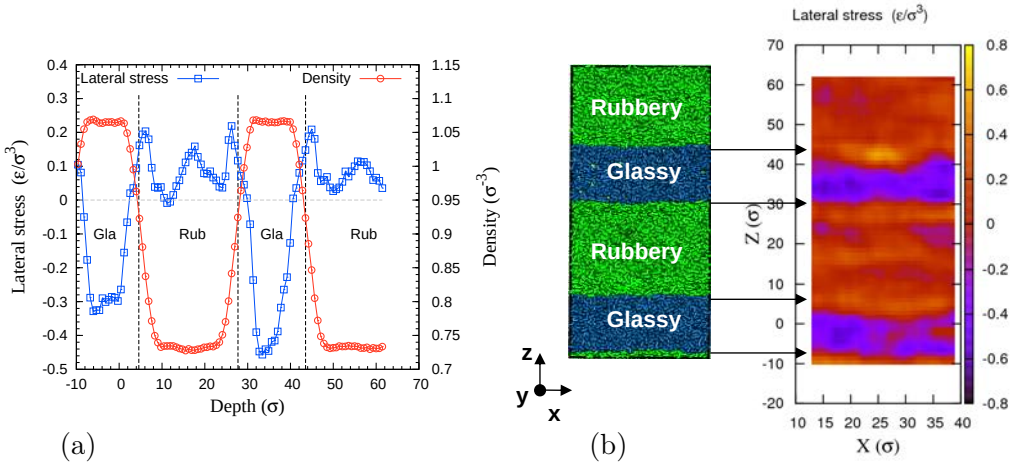

FIGURE 5.5 – (a) Profile of the lateral stress $(\sigma_{xx} + \sigma_{yy})/2$ (blue line labelled by □) along the z direction. The density profile is also plotted to identify the glassy (Gla) and rubbery (Rub) phases. The negative stress level of glassy layers denotes the compression state imposed by the deformation conditions of rubbery layers. (b) Lateral stress cartography. Snapshots were taken at a $\varepsilon_{zz} = 0.04$ (the same sample is used for the plots shown in figure 5.5). The lateral stress is not perfectly homogenous within each phase. The local stress is computed within a box of size $5\sigma \times 5\sigma \times L_y = 102\sigma$.

buckling takes place at small strains, and therefore within a small computation time. Assuming that the compressive stress in the glassy phase is the driving force for buckling, one should therefore choose the parameters that correspond to a large value of this stress. All curves in figure 5.6 correspond to samples that have the same segregation parameter $\frac{k_B T}{N}\tilde{\varepsilon}N = 0.25$. The Lennard Jones energy of the glassy phase (ε_{AA}) is unchanged but the two other LJ interactions ($\varepsilon_{BB}, \varepsilon_{AB}$) are tuned. As shown in this figure the lateral force increases as ε_{BB} increases. In view of this trend the better choice of the segregation state seems to be $(\varepsilon_{AA} = 1.0, \varepsilon_{BB} = 0.5, \varepsilon_{AB} = 0.5)$, however we found in the first simulations at high strain rate that this system deforms homogeneously (see section 5.6 for a discussion of strain rate effects). In this case, the elastic contrast between the two phases is too small to observe buckling at small strains. Another interesting choice is $(\varepsilon_{AA} = 1.0, \varepsilon_{BB} = 0.3, \varepsilon_{AB} = 0.4)$, this sample shows a localized strain in the rubbery phase and relatively high increase of the compressive force before the cavitation strain $\varepsilon_{zz} = 0.08$. In the following, we have chosen this set of parameters for carrying out our numerical studies of buckling.

Lateral force and cavitation : It may be important to note here the influence of the cavitation upon the lateral force. It was reported in the previous chapter that cavities nucleate in the rubbery phase at yield point. The cavitation is followed by a marked relaxation of stress and a drop in the lateral force. If the buckling was

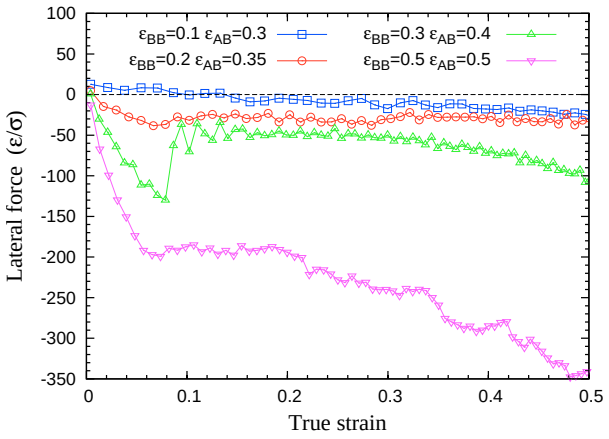

FIGURE 5.6 – Influence of interblock and intrablock interaction energies on the lateral force applied to the glassy layer. In all specimens ε_{AA} was taken equal to 1ε which leads to the same segregation parameter for all samples $\frac{k_BT}{N}\tilde{\varepsilon}N = \frac{1}{2}(\varepsilon_{AA} + \varepsilon_{BB}) - \varepsilon_{AB} = 0.25$.

not triggered before the cavitation, it will be difficult to start after the cavitation since the lateral force is relaxed and damped. Therefore, the observation of buckling requires that this instability takes place before the nucleation of cavities. This point is also detailed in the next section.

5.3.2 Construction of a "large" system

It is well know from the theory of elastic plates or rods that, for a given force, buckling will be observed only above a threshold dimension (and conversely only above a threshold force for a given dimension). In triblock systems, the glassy layers in the samples must have a sufficiently small bending energy compared to the tensile strain energy. This condition can be fulfilled in two ways : (i) reducing the hard phase thickness and (ii) increasing the sample width. The first possibility leads to some problems, since the thickness of the hard phase (glassy) is imposed by the segregation parameters, chain length and temperature. having chosen the segregation state, any change in other variables may alter the morphology, and the properties of each layer. Therefore, the second possibility, i.e. an increase of the lateral size, was retained for our studies.

After the generation and the segregation-relaxation process, (detailed in the appendix), the basic sample was replicated several times (at least six times) in the Y direction. The initial sample is composed from 432 chain of 200 beads per chain, the dimensions of the simulation box are $L_X \times L_Y \times L_Z = 35.8 \times 32.9 \times 75.2$.

The replication is carried out before cooling the sample, at $k_bT = \varepsilon$, the two phases are rubbery in this case. Since the replication conserves the periodicity of bead positions and velocities, the bead velocities are then rescaled and an additional

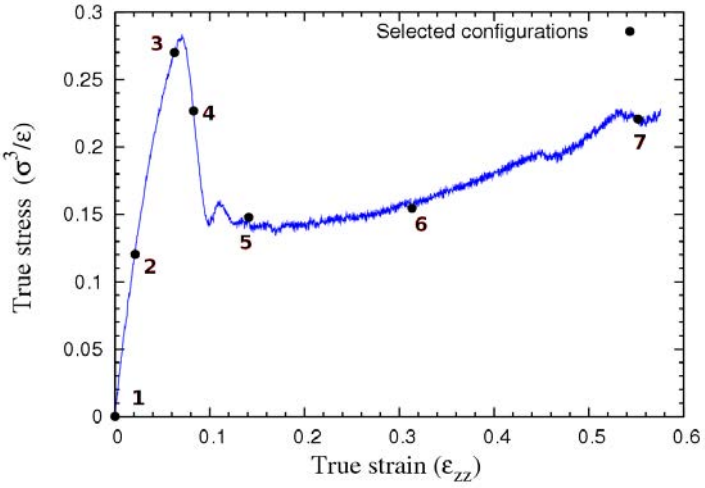

FIGURE 5.7 – Mechanical response of the initial sample replicated 12 times under uniaxial strain conditions. The black points denote the selected configurations that are shown in figure 5.9. The drop of stress is correlated with the nucleation and growth of cavities in the rubbery phase.

MD steps (10^6) are performed to remove this periodicity. After the relaxation stage, the specimen is cooled to the temperature $k_BT = 0.3\varepsilon$ by 7×10^5 MD steps and relaxed again (10^6) MD. note that the pressure remains zero in all of these steps. The sample is now ready for the tensile test.

5.3.3 Mechanical behaviour of the large sample

A homogenous uniaxial tensile test is performed in order to probe the mechanical response of the specimen. The tensile strain was applied in the direction Z (perpendicular to the lamellae) at a constant velocity $V_z = \dot{L}_z$. In this first set of results, the strain rate is $\varepsilon_{zz} = 7.3 \times 10^{-5}$. The pressure is fixed to zero in the X and Y directions by a Nose-Hoover barostat. The pressure in the Z direction was averaged over short deformation intervals, of $\delta\varepsilon_{zz} = 0.002$. The stress-strain curve is plotted in figure 5.7 and the corresponding snapshots are shown in figure5.9. For clarity, the snapshots of the specimen are replaced with snapshots of the local density map, which allows one to distinguish each phase and to detect any anomalous change in the local density (mainly by cavitation). The constitutive law displays three main regimes.

The elastic regime : at small strain, the stress grows linearly with the imposed deformation. This regime is limited to a very small deformation amount (less than 2%). The total Young modulus can be fitted from this curve, we find $E_t = 5.6$. This value of E_t results from the combination of the elastic behavior of each phase. The density maps show very little change in this regime.

Buckling : Beyond the elastic regime, a progressive softening is observed. This

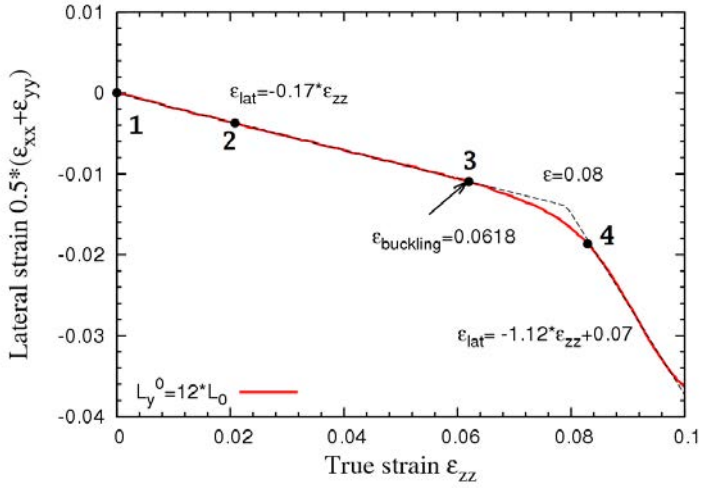

FIGURE 5.8 – Evolution of the lateral strain $0.5(\varepsilon_{xx} + \varepsilon_{zz})$ under uniaxial tensile conditions. The local slope defines the Poisson ratio, and buckling is correlated to a strong change in this slope. The corresponding snapshots of the marked points are shown in figure 5.9.

slight deviation from the elastic linear behavior is commonly interpreted as resulting from the changes in molecular conformations (especially in the rubbery phase). The buckling of the glassy phase starts at $\varepsilon_{zz} = 0.06$. The buckling strain was detected by the change of Poisson ratio. Figure 5.8 shows the mean perpendicular strain ($\varepsilon_{\perp} = \frac{\varepsilon_{xx}+\varepsilon_{yy}}{2}$) with respect to the applied strain ε_{zz}. As in figure (5.7), the indexed points on the curve correspond to the snapshots of figure 5.9.

Within the selected range of deformation, the curve displays two linear segments with two different slopes. The first one fits the Poisson ratio of the sample. The next segment, with a larger slope results from the rapid change in lateral dimensions after buckling. In other words, before the buckling the contraction strains in the lateral directions (ε_{xx} and ε_{yy}) results from the Poisson effect but after the buckling, the imposed deformation will be compensated by the lamella rotation rather than the lamella stretching, the sample deforming in an "accordion" like manner.

In this regime, the strain components (ε_{xx} and ε_{yy}) become dependent on the lamellae orientation . The break of slope in figure 5.8 can then be considered as the signature of buckling. WIth this definition, the value $\varepsilon_{Buck} = 0.06$ at point 3 corresponds very well with the onset of the buckling, as observed visually in the third snapshot of figure 5.9.

Cavitation : After buckling, a strong drop of stress occurs at $\varepsilon_{zz} = 0.008$. This drop can be correlated with the nucleation of cavities in the rubbery phase, as illustrated by the fourth density map in figure 5.9. The low density spots in figure 5.9 correspond to the cavitation in the rubbery layers. Indeed, due to the buckling, the local deformation of the rubbery phase is not homogenous. The sample progressively adopts a chevron morphology, with different deformation states : at large strains the

the buckling is confined to a localized region in space, developing into a hinge. At the hinges of the chevron the deformation is essentially tensile, while the tilted part undergoes a simple shear deformation. The latter deformation is caused by the rotation and sliding of the hard lamellae. A gradient of displacement results within the rubbery phase confined between two glassy layers in the tilted part of the chevron. At the hinges of the chevron the deformation, on the other hand, is essentially triaxial, and favors nucleation of cavities. As a result the cavities in the rubber that initially appear randomly tend to heal in the sheared zones and nucleate preferentially where triaxial stress persists, as illustrated by the sequence of snapshots (from 4 to 7) in figure 5.9.).

Cavitation and strain hardening : The last part of the stress strain curve (points 5 to 6 in figure 5.7) of the buckled sample reveals a short drawing regime at constant stress, followed by a strain hardening region. The drawing regime is very short compared to the homogenous polymer behaviour after the cavitation, but in both cases this regime results from the balance between the elastic energy and the surface free energy of the cavity. As the cavities in the rubber will be located in the hinge of the chevron structure, the development of free surfaces by cavitation becomes constrained by two factors : (i) The spacing between glassy lamellae and (ii) the 'chevron' morphology of the sample. The first factor controls the propagation of cavities in the strain direction (longitudinal direction) while the second one limits the propagation in other directions (lateral directions). Due to these factors, the mentioned balance of energies is rapidly exhausted, and the stress rises again. The link between the strain hardening (SH) and the change in chain conformations is less well understood than in the homogenous polymer case, as the strain state of the sample is a complex combination of triaxial deformation at the extremity of the chevrons and of shear deformation in other parts. A detailed analysis of strain hardening under various simple deformations would be necessary to understand fully this behavior and relate it to local chain conformations.

5.3.4 Evolution of diffraction patterns

Small Angle X Ray Scattering (SAXS) has been frequently used in experimental works in order to probe the microstructural evolution of the sample undergoing uniaxial deformation. The onset of the buckling was generally related to the arching of the SAXS spots which evolves into a four points pattern at high strain. The chevron angle and the local nominal elongation λ can be also measured via the tilt angle ϕ (see figure 5.10b) : $\lambda = 1/cos(\phi)$. Note that in the initial, undeformed samples, may display a slight arching of their SAXS spots due to the presence of some morphological orientation defects . Figure 5.10 displays the intensity plot of the Discrete Fourier Transform (DFT) of the local density at several values of the total deformation. These plots are equivalent to the experimental SAXS reflections. The DFT was realized in the YZ plane, as the density maps of figure (5.9). The first Fourier transform, for the undeformed sample, displays two symmetrical spots that indicate the presence of one lamellar orientation. This pattern remains unchanged

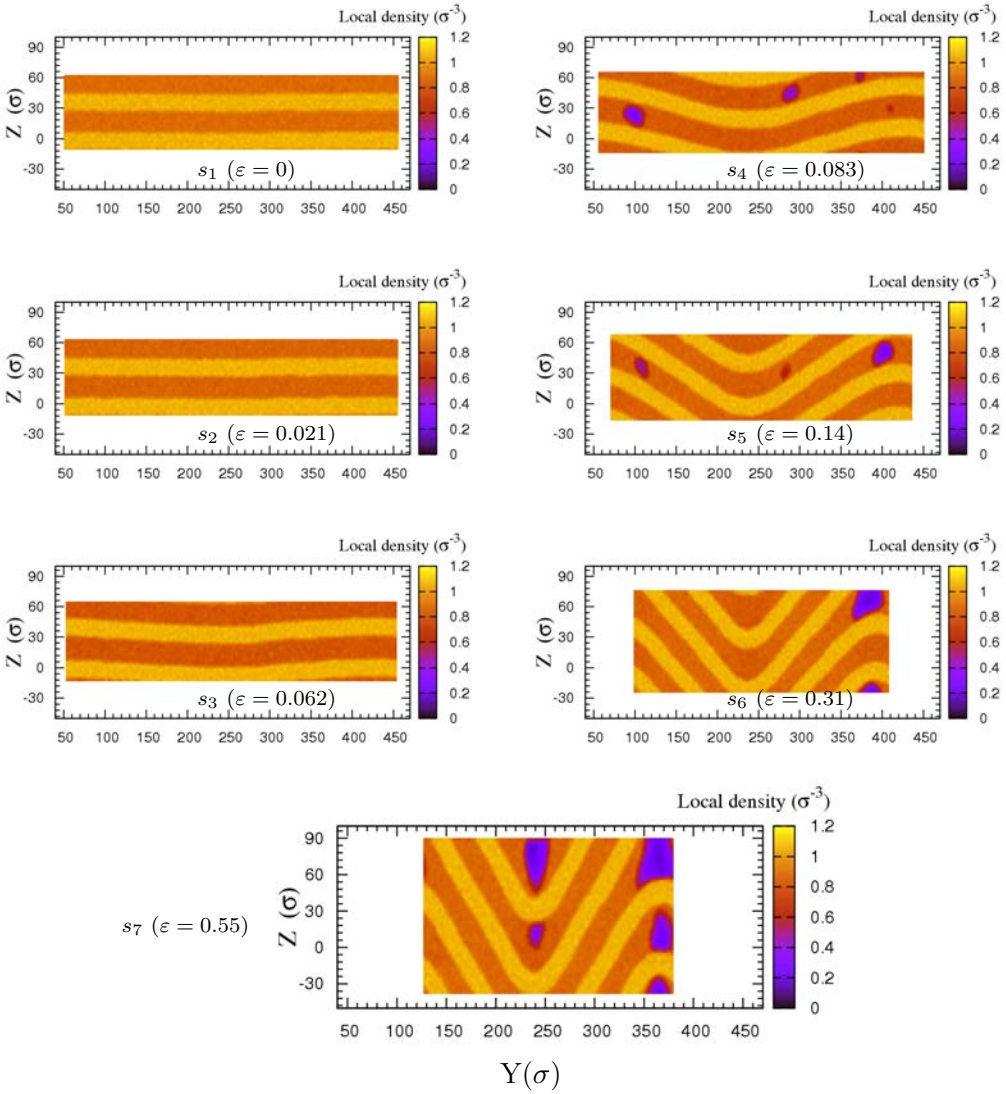

FIGURE 5.9 – Local density maps at several strains. The high (low) density phase corresponds to the glassy (rubbery) lamellae. The phase buckling starts before cavitation. As the deformation progresses, cavities will nucleate randomly in the rubbery phase. Cavities that are located in the tilted part of the chevron disappear rapidly ; however, only cavities that are located in the hinges will survive to a high strain.

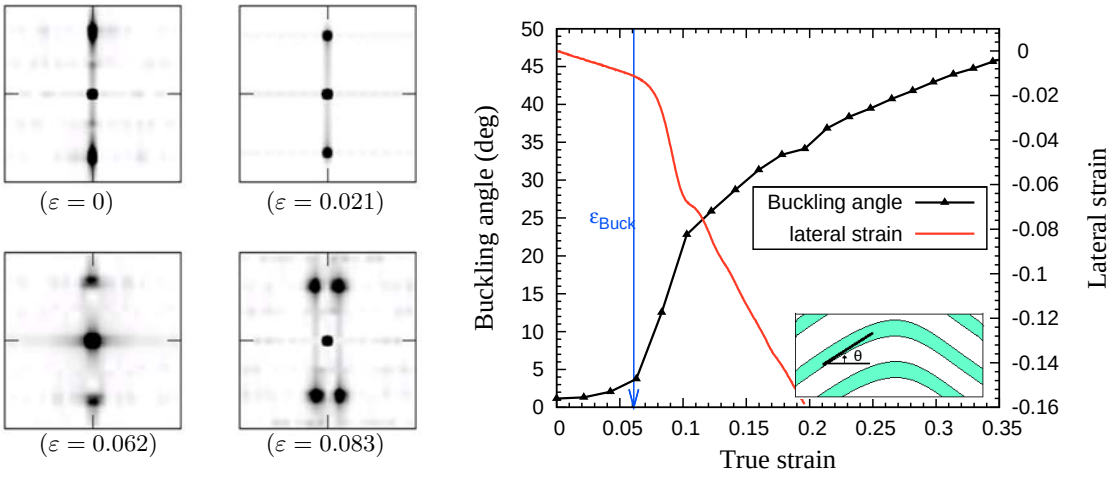

FIGURE 5.10 – (a) Discrete Fourier Transform of local density for several samples with different strain levels. (corresponding to the images shown in figure 5.9). The perfect undulation of the lamellar structure leads to a fourfold symmetry of the dark spots in the pattern. Similar results were found for real triblock samples under strain using small angle X ray scattering. (b) Angle ϕ between the buckling fragments and the horizontal axis Y (see inset).

in the elastic regime since the sample conserves its lamellar morphology but only the spacing between lamellae changes. The onset of buckling is marked by the arching of the pattern (third image) which rapidly becomes four symmetrical spots (2 plane orientations of the chevron). As the deformation progress the azimuthal angle increases since the chevron angle decreases.

Note that the DFT was applied on binary images that distinguish each phase by a specific label : glassy (label 1) and rubbery (label 0). The loss of local density due to the cavitation is not taken into account, so that no signature of cavitation is apparent. To illustrate the evolution of the buckling angle with respect to the deformation, the latter is also plotted in figure 5.10.b. The angle was evaluated by a direct measurement. The tilted parts of the chevron were fitted by straight lines, and the angle is deduced from their slopes. As shown, The curve is initially stable at zero, at buckling strain a rapid increases of angle takes place.

5.4 Elastic modeling of the buckling instability

As mentioned in the introduction, two different theoretical descriptions of buckling of lamellae under stress are available in the literature. One approach is based on writing a free energy function of the order parameter that describes the lamellar order, and explains the instability by the fact that a strained state will try to maintain the wavelength that minimizes this free energy. This approach would be appropriate

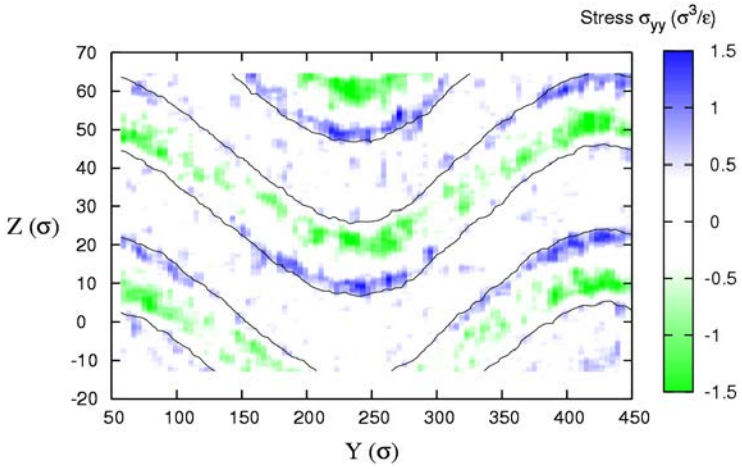

FIGURE 5.11 – Spatial distribution of lateral stress σ_{yy} in a buckled sample at a true strain $\varepsilon_{zz} = 0.083$. The boundaries of each phase are estimated from the local density. The lateral stress exhibits a noticeable gradient localized at the hinges of the chevrons of glassy phases, however ; the stress vanishes in the rubbery phases except for some some small fluctuations.

for copolymers in which both phases are at equilibrium, so that the order parameter can respond to the deformation. Here one of the phases is glassy, and the explanation for the buckling instability must be searched in a different direction, involving the minimization of the total elastic energy. This description (which for some aspects goes back to early works of Biot and Ramberg [Biot 1961, Ramberg 1964]) has been detailed in an important paper by Read *et al* [Read 1999]. In this section, we reproduce the main steps of this calculation. The calculation will be presented first in two dimensions.

The model aims at describing the balance of energies that results from : (i) the macro-scale deformation of the sample (the elastic energy), (ii) the hard phase bending and (iii) the polarization between phases. The elastic energy of 2D sample under small strain can be written as :

$$U_{macro} = \frac{1}{2}(C_{11}\varepsilon_{11}^2 + 2C_{13}\varepsilon_{11}\varepsilon_{33} + C_{33}\varepsilon_{33}^2 + G\varepsilon_{13}^2) \tag{5.1}$$

where C_{ij} are the components of a symmetric 2×2 stiffness matrix of *the entire system*, G is the shear modulus parallel to the layer. In this equation the material is considered as homogeneous and anisotropic. The C_{ij} matrix can be determined by mechanical tests that are applied in different directions, or deduced from the elastic properties of each lamella.

The phase bending energy results from the variation of lamellar rotation angle θ (the angle between the tangent on layer and the horizontal axis X). The energy density associated with the bending can be written as

$$U_{bend} = \frac{1}{2}K(\nabla_x\theta)^2 \tag{5.2}$$

K is the bending modulus of the sample. Indeed, due to the serial coupling between phases the bending modulus will be dominated by the contribution bending the hard phase. (see the magnitude and the distribution of stress in each phase in figure 5.11) The bending modulus can then be estimated from simple beam bending theory as follows :

$$K_{est} = \frac{\phi_h^3 E_h d^2}{12(1-\nu_h^2)} \tag{5.3}$$

where ϕ_h is the volume fraction of the hard phase, E_h is the Young modulus of the hard phase, ν_h is its Poisson ratio and d is the lamellar spacing.

The polarization phenomenon occurs when the layer is alternatively compressed and dilated along its length. In such a case the rubbery phase relieves some of the compression or dilatation energy by moving from the compressed regions to the dilated regions. As the constitutive phase are bridged together by strong FENE bond, the polarization costs shear energy. The occurrence of polarization is observed where a change in buckling amplitude subsists between two successive hard layers. Fortunately, this phenomenon is not pronounced in our systems : first, because of the periodic boundary conditions in the tensile direction and second, there are only two glassy phases and two rubbery phases per system. Thus, the contribution of the polarization energy can be neglected in our system.

The total energy density results from the addition of the bulk elastic energy and the bending energy, which yields :

$$\begin{aligned} U_{2D} &= U_{bend} + U_{macro} \\ &= \frac{1}{2}(C_{11}\varepsilon_{11}^2 + 2C_{13}\varepsilon_{11}\varepsilon_{33} + C_{33}\varepsilon_{33}^2 + G\varepsilon_{13}^2 + K(\nabla_x\theta)^2) \end{aligned} \tag{5.4}$$

All the strain terms in the previous equation are defined with respect to a local reference frame defined by the lamellar direction. The general deformation of the system can also be described by the displacement vector in the laboratory $(x-z)$ coordinate system. In order to describe the formation of chevrons, the global energy must be written in terms of the laboratory coordinates, and the local variables must be related to these coordinates. Let us suppose $\delta x'$ and $\delta z'$ are the transformed coordinates of a vector with coordinates δx and δz taken in the initial configuration. the transformation include three steps (i) stretching ε_{11} and ε_{33} in the local 1-3 frame. (ii) the shear ε_{13} and finally (iii) a rigid body rotation of the frame. The relation between an initial vector and the one in the deformed configuration can be written as follows :

$$\begin{pmatrix} \delta x' \\ \delta z' \end{pmatrix} = \begin{bmatrix} \cos\theta & -\sin\theta \\ \sin\theta & \cos\theta \end{bmatrix} \begin{bmatrix} 1+\varepsilon_{11} & \varepsilon_{13} \\ 0 & 1+\varepsilon_{33} \end{bmatrix} \begin{pmatrix} \delta x \\ \delta z \end{pmatrix} \tag{5.5}$$

The variation of the displacement field $\vec{v}(x,z)$ along the vector $(\delta x, \delta z)$ is $(\delta v_x, \delta v_z)$ where $\delta v_x = \delta x' - \delta x$ and $\delta v_z = \delta z' - \delta z$ Therefore the displacement gradient is obtained as :

$$\begin{bmatrix} \nabla_x v_x & \nabla_z v_x \\ \nabla_x v_z & \nabla_z v_z \end{bmatrix} = \begin{bmatrix} \frac{\delta v_x}{\delta x} & \frac{\delta v_x}{\delta z} \\ \frac{\delta v_z}{\delta x} & \frac{\delta v_z}{\delta z} \end{bmatrix} = \begin{bmatrix} \cos\theta & -\sin\theta \\ \sin\theta & \cos\theta \end{bmatrix} \begin{bmatrix} 1+\varepsilon_{11} & \varepsilon_{13} \\ 0 & 1+\varepsilon_{33} \end{bmatrix} - \mathbf{I} \tag{5.6}$$

By inverting this system one obtains the local strains and rotation angle in terms of the gradients of the displacement field $v(x,z)$, then we obtain :

$$\sin\theta = \frac{\nabla_x v_z}{\beta} \tag{5.7}$$

$$\varepsilon_{11} = \beta - 1 \tag{5.8}$$

$$\varepsilon_{33} = \frac{1}{\beta}((1+\nabla_z v_z)(1+\nabla_x v_x) - (\nabla_z v_x)(\nabla_x v_z)) - 1 \tag{5.9}$$

$$\varepsilon_{13} = \frac{1}{\beta}((\nabla_z v_x)(1+\nabla_x v_x) - (\nabla_x v_z)(1+\nabla_z v_z)) \tag{5.10}$$

where $\beta = \sqrt{(\nabla_x v_z)^2 + (1+\nabla_x v_x)^2}$. The displacement can be expressed in terms of the global deformation ε_{xx}, ε_{xz} and ε_{zz} by distinguishing an affine displacement proportional to the global deformation and a non affine one, $\vec{u}(x,z)$:

$$v_x = \varepsilon_{xx} x + \varepsilon_{xz} z + u_x \tag{5.11}$$

$$v_z = \varepsilon_{zz} z + u_z \tag{5.12}$$

Substituting back into the equations (5.7)-(5.10) one obtains an expression of the energy density which can be expanded in small powers of $\vec{u}(x,z)$ and averaged over the volume of the system. The averaging denoted by the angular brackets $\langle \cdots \rangle$ eliminates linear terms such as $\langle \nabla_x u_x \rangle = \langle \nabla_z u_x \rangle = \langle \nabla_z u_z \rangle = 0$ due to the boundary conditions

Finally the expression (5.4) of the energy becomes :

$$\begin{aligned} 2\langle U_{2d} \rangle &= \langle U_{macro} + U_{bend} \rangle + G\langle (\nabla_z u_x)^2 \rangle \\ &= C_{11}\varepsilon_{xx}^2 + 2C_{13}\varepsilon_{xx}\varepsilon_{zz} + C_{33}\varepsilon_{zz}^2 \\ &+ C_{11}\langle (\nabla_x u_x)^2 \rangle + 2C_{13}\langle (\nabla_z u_x)(\nabla_x u_z) \rangle + C_{33}\langle (\nabla_z u_z)^2 \rangle \\ &+ \tfrac{\langle (\nabla_x u_z)^2 \rangle}{(1+\varepsilon_{xx})^2}[G - \varepsilon_{zz}(C_{33} - C_{13} - 2G) - \varepsilon_{zz}^2(C_{33} - G) + \varepsilon_{xx}(C_{11}(1+\varepsilon_{xx}) - C_{13})] \\ &+ 2\tfrac{\langle (\nabla_z u_x)(\nabla_x u_z) \rangle}{(1+\varepsilon_{xx})}[G - \varepsilon_{zz}(C_{33} - G) - \varepsilon_{xx} C_{13}] \\ &+ K\langle (\nabla_x^2 u_z)^2 \rangle + O(u^4) \end{aligned} \tag{5.13}$$

The system becomes linearly unstable against buckling when there exists a deformation mode $\vec{u}$ with a negative coefficient in the expansion. In the rest of calculation,

we discuss the linear stability with respect to a sinusoidal perturbation of the form observed in our simulations, namely

$$u_z(x,z) = U_0 sin(kx) \quad ; \quad u_x(x,z) = 0 \tag{5.14}$$

with k is a wave vector compatible with the boundary conditions, $k = \frac{2n\pi}{L}$. S Substituting in equation 5.14 in 5.13 gives :

$$\begin{aligned} 2\langle U_{2d}\rangle &= C_{11}\varepsilon_{xx}^2 + 2C_{13}\varepsilon_{xx}\varepsilon_{zz} + C_{33}\varepsilon_{zz}^2 \\ &+\tfrac{U_0^2}{4}\{f_1(\varepsilon_{xx},\varepsilon_{zz})k^2 + Kk^4\} + O(U_0^4) \end{aligned} \tag{5.15}$$

where

$$\begin{aligned} f_1(\varepsilon_{xx},\varepsilon_{zz}) &= \tfrac{1}{(1+\varepsilon_{xx})^2}[G - \varepsilon_{zz}(C_{33} - C_{13} - 2G) \\ &-\varepsilon_{zz}^2(C_{33} - G) + \varepsilon_{xx}(C_{11}(1+\varepsilon_{xx}) - C_{13})] \end{aligned} \tag{5.16}$$

The buckling instability occurs upon increasing strain when the coefficient of U_0^2 becomes negative, meaning that the global gain in elastic energy overwhelms the bending energy penalty. To close the system, one assumes that before the buckling begins (i.e. in the elastic regime) ε_{xx} can be substituted by $\nu\varepsilon_{zz}$ where ν is a global Poisson ratio. Under this assumption, $f_1(\varepsilon_{xx},\varepsilon_{zz})$ becomes a function of ε_{zz} only.

A three dimensional version of the equation was developed also by Read at al. The resulting energy equation give a coefficient of U_0 similar to equation 5.15 with only a slight change in $f_1(\varepsilon_{xx},\varepsilon_{zz})$ which becomes :

$$\begin{aligned} f_1^{3D}(\varepsilon_{xx},\varepsilon_{yy},\varepsilon_{zz}) &= \tfrac{1}{(1+\varepsilon_{xx})^2}[G - \varepsilon_{zz}(C_{33} - C_{13} - 2G) \\ &-\varepsilon_{zz}^2(C_{33} - G) + \varepsilon_{xx}(C_{11}(1+\varepsilon_{xx}) - C_{13}) - C_{23}\varepsilon_{yy}] \end{aligned} \tag{5.17}$$

Note that due to the lamellar morphology of our system the mechanical properties are isotropic in the plane of the lamellae. Thus, $C_{23} = C_{13}$ and $\varepsilon_{xx} = \varepsilon_{yy} = \nu\varepsilon_{zz}$, so that $f_1^{3D}(\varepsilon_{xx},\varepsilon_{yy},\varepsilon_{zz})$ can be simplified as follow :

$$\begin{aligned} &f_1^{3D}(\varepsilon_{xx},\varepsilon_{yy},\varepsilon_{zz}) = f_1^{3D}(\nu\varepsilon_{zz},\nu\varepsilon_{zz},\varepsilon_{zz}) = f_2^{3D}(\varepsilon_{zz}) = \\ &\tfrac{1}{(1+\varepsilon_{xx})^2}[G - \varepsilon_{zz}(C_{33} - C_{13} - 2G) \\ &-\varepsilon_{zz}^2(C_{33} - G) + \nu\varepsilon_{zz}(C_{11}(1+\nu\varepsilon_{zz}) - 2C_{13})] \end{aligned} \tag{5.18}$$

The buckling strain ε_{buck}^* can be estimated by solving this equation for a fixed wavevector $k_n = 2n\pi/L$:

$$f_2^{3D}(\varepsilon_{buck}^*)k_n^2 + Kk_n^4 = 0 \tag{5.19}$$

For a given wavevector k_n, buckling will become possible above a certain strain ε_n^* such that $f_2^{3D}(\varepsilon_n^*) = -Kk_n^2$. As $|f_2^{3D}|$ is an increasing function of the strain, the

wavevector corresponding to the largest wavelength, i.e. the size of the box, will become unstable at the smallest strain according to this analysis. This also implies that for a smaller box size, a larger strain would be needed to observe buckling ; as noted above, cavitation then tends to take place before the critical strain for buckling is reached, and the elastic analysis becomes irrelevant above the cavitation threshold.

In the following, numerical comparison between simulations and this theory will be made by using for the elastic constants C_{ij} values determined from simple linear deformations of a small sample that does not exhibit the buckling instability. These values are, for the interaction parameters and temperature mentioned above, $C_{11} = 24.17$, $C_{33} = 7.61$, $C_{13} = 6.5$, and $G = 0.07$. The Poisson ratio is $\nu = -0.178$.

5.5 Effect of sample size

The discussion in the previous section shows that the periodic boundary conditions have an important influence on the buckling instability. As shown in figure 5.13, the instability takes place for a different mode for a system with free or with periodic boundary conditions, the first one undergoing a 'half wave' instability which is prohibited in the second case. Also, the buckling in the small samples is impossible since the bending energy of the glassy phase is very big compared to the deformation energy of the bulk. Therefore, a critical length of sample can be defined as L_y^*. L_y^*, the minimal length from which the sample will be able to buckle under tensile strain. This was already shown qualitatively in sections 5.3 and 5.3.3, where it was shown that a large sample replicating 12 times our initial simulation cell along the Y direction was needed to observe the buckling instability. According to the elastic theory, the instability wavelength will take place at smaller and smaller strains for bigger and bigger samples, and always at the largest possible wavelength allowed by the boundary conditions. This, however, contradicts a number of experimental observations in which a rather well defined wavelength of the chevron structure is observed. In [Read 1999], this discrepancy is assigned to preexisting defects in the microstructure. Simulation provides an ideal benchmark of this hypothesis, as we deal here with an ideal microstructure. We have therefore studied replicated samples of various sizes, by replicating the **same** elementary cell n times along the Y direction, where n = 3,6,12,15 and 24.

Figure 5.13 compares the mechanical response of all tested samples, at the same strain rate. In terms of stress-strain relation (5.13.a), all samples have roughly the same mechanical up to the yield point. The drawing regimes exhibits important differences between smaller and larger samples. The stress softening in long samples is sharper than in the small ones. This stress drop (or softening) is related to the intensity of plastic activity. Indeed, in our case the release of stress can be assigned to a one or both events : (i) Cavitation and (ii) buckling instability. (i) For the cavitation, the nucleation of free surface transforms a portion of the stored elastic energy to a free surface energy, which induces a stress drop. (ii) In the buckling

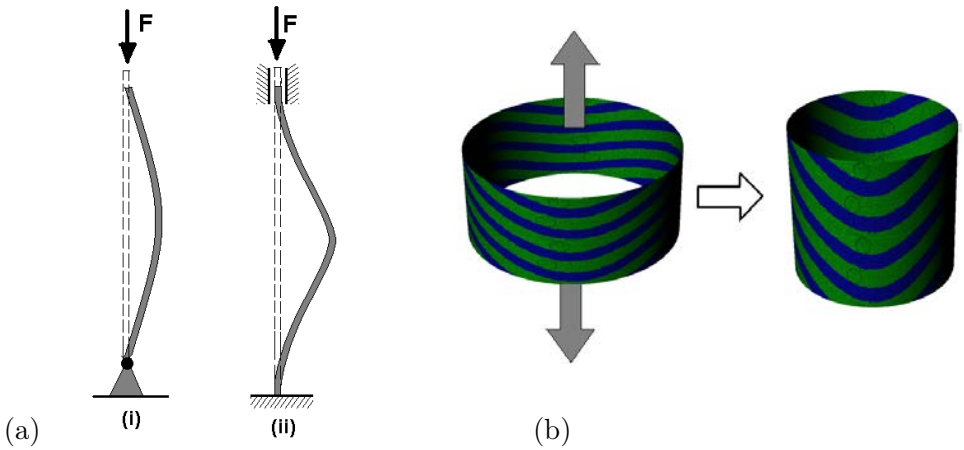

FIGURE 5.12 – (a) sketch image shows the difference in buckling response for two different boundary conditions. The first configuration corresponds to a free boundary condition while the second case describes the buckled configuration with constrained boundaries. (b) representation of the periodic boundary influence in the buckled configuration. The sample can be assimilated to a pipe section, the deformation will decrease the pipe radius and increase the section length.

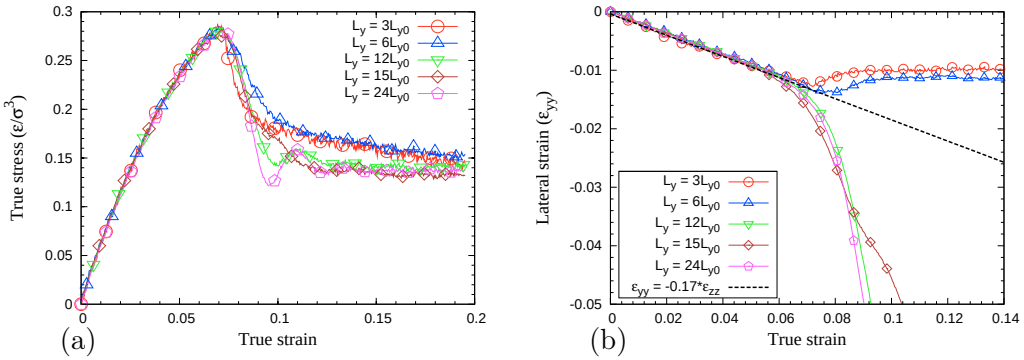

FIGURE 5.13 – (a) Stress strain curves of several samples with different sizes. All curves have the same shape and collapse perfectly in the elastic-viscoelastic regimes. The small difference in the stress softening regime can be attributed to the occurrence of buckling in long samples. (b) Comparison between the lateral deformations of the same samples. For the shorter samples ($L_y \leq 6L_{y0}$), the nucleation of cavities relaxes the lateral deformation and no buckling occurs. The deformed configuration snapshots of each sample are shown in figure 5.14.

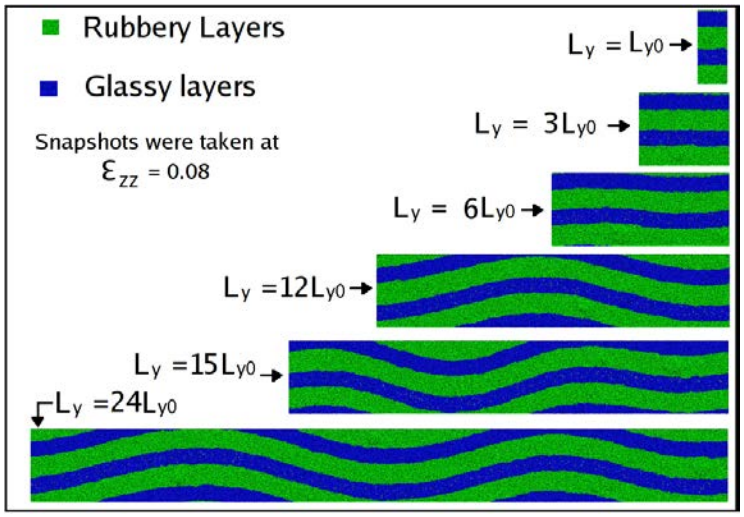

FIGURE 5.14 – Snapshots of several samples with different sizes. All configurations are taken at a true strain $\varepsilon_{zz} = 0.08$. The phase buckling is only authorized for the longer samples with $L_y \geq 12L_{y0}$). The buckling wave length seems to be size independent.

case, the change of the intrinsic deformation mechanism from tensile strain to shear-rotation strain releases the local deformation of some zones and as a consequence the elastic energy will also be relaxed. For long samples, both events participate in the stress softening, thus the drop of stress will be accelerated compared to the short sample case where only cavitation is present.

Figure 5.13.b shows the lateral strain in the different samples. All curves are well fitted by a straight line with the same Poisson ratio in the first linear part (dashed line), but after the yield strain, strong deviations can be observed : the lateral strain decreases for long samples ($L \geq 12L_{y0}$) while it increases for the shorter ones ($L \leq 6L_{y0}$). The decrease in lateral strain is related to buckling instability, as discussed in section 5.3.3. For short samples, the increase of lateral strain after the yield is strongly correlated with the nucleation of cavities in the rubbery phase. The buckling in such samples is completely absent or irrelevant, as shown in the snapshots of figure (5.14).

Examining the behaviour of the different samples, one concludes that the minimal length for observing buckling before cavitation is between $6 \leq L_y^*/L_{y0} \leq 12$. For samples larger than $12L_{y0}$, the onset of buckling occurs always at the same strain ($\varepsilon_{buck} = 0.06$), in contradiction with the expectation from the elastic description of the previous section. An explanation of this behavior will be provided below, when we study strain rate effects. Another surprising observation, illustrated in figure 5.14, is that the wavelength of the instability does not appear to increase with the size of the system. In the 12 times replicated samples (S_{12}) (the smallest sample that exhibits buckling) the undulation wave length is equal to the sample size as expected. However for the 15 times replicated sample (S_{15}), the wave length is half

Sample	L_y	Buckling	Cavitation	ε_{zz}^{yield}	σ_{zz}^{yield} (ε/σ^3)	ε_{zz}^{buck} me.	ε_{zz}^{buck} pr. $k = 2\pi/L$	ε_{zz}^{buck} pr. $k = 4\pi/L$	σ_{zz}^{buck} (ε/σ^3)
S_3	$3L_{y0}$	no	yes	0.07	0.287	-	0.104	0.27	-
S_6	$6L_{y0}$	no	yes	0.07	0.284	-	0.044	0.106	-
S_{12}	$12L_{y0}$	yes	yes	0.071	0.282	0.054	0.026	0.043	0.248
S_{15}	$15L_{y0}$	yes	yes	0.07	0.276	0.048	0.023	0.035	0.228
S_{24}	$24L_{y0}$	yes	yes	0.072	0.28	0.053	0.021	0.026	0.240

TABLE 5.1 – Strain and stress that correspond to the buckling and yield. These values were averaged over a short time interval (t=6τ that corresponds to a strain range of 4.5×10^{-4}). All simulations are done at a strain rate of 7.3×10^{-5}. The first mode buckling strains predicted ("pr." in the table) from equation 5.19 are less than the measured values ("me." in the table)

the sample size, and the same is observed in the sample with 24 replications (S_{24}). Therefore it appears that the instability selects a preferred wavelength in the range $6 \leq L_y^*/L_{y0} \leq 12$.

Table 5.5 summarizes the buckling and the yield properties obtained at a strain rate of 7.3×10^{-5}. For each sample, the theoretical value of the buckling strain was calculated from equation 5.19, assuming an instability wavevector $k = 2\pi/L$. As shown in the table, the predicted values of ε_{zz}^{buck} is always less than the measured one. This difference will be interpreted below as a direct consequence of kinetic factors that are not taken into account in the elastic calculation. Indeed the strain rate in this series of tests can be considered as fast compared to the buckling kinetics ; thus, long samples don't have the required time to adopt the lowest energetic mode for buckling. This will also explain why the sample S_{24} has two undulations rather than one. Note finally that the yield strain and stress are roughly the same for all samples. The yield is mainly correlated with the cavitation in the rubbery phase, which is essentially in the same deformation state for all sizes.

5.6 Influence of strain rate

In section 5.5 we have shown that the buckled configurations of S12,S15 and S24 samples have the same undulation wavelength and the same buckling strain. In addition, the S15 and S24 samples display two wavelengths per configuration which is completely unexpected as the lowest energy configuration would have only one undulation per sample. In this section, we will show that the the lowest energy buckling mode indeed develops when the strain rate conditions are gentle enough. In the next subsections we first describe the mechanical response of S12 sample at low strain rate and after we show how the buckling cavitation are influenced by both factors : strain rate and sample size.

5.6.1 Response of the S12 sample at low strain rate

In the 12 times replicated sample S12, the observations from the previous section are that the sample develops an instability along the lowest energy mode. However, the strain at which the instability is observed is higher than predicted by elasticity theory. In figure 5.26, we show the results of a tensile test performed under the same conditions as in section 5.3.3, except for the strain rate which is 5 times smaller, $\dot{\varepsilon}_{yy} = 1.4 \times 10^{-5}$. The resulting stress-strain curve superimposed with the evolution of lateral strain are shown in the first panel. The linear part of both curves corresponds to the elastic regime (the stress strain curve fits the Young modulus in this regime and the lateral strain curve fits the Poisson ratio). The end of this regime is marked by the yield, followed by a stress softening in stress-strain curve. The yield point corresponds very well to the onset of buckling, indicated by the change of slope (Poisson ratio) in the curve for the lateral strain. The absence of cavities was proven by inspecting the local density of the sample at different strain levels. Therefore, the yield and the stress softening in this case is correlated to the onset and the development of the buckling in the sample. The last part of the stress-strain curve is the drawing regime that corresponds to the development of the buckling undulation in an accordion mechanism. Note that the range of strain studied is relatively small so that the strain hardening regime is not attained. The absence of cavities in the buckled sample at low strain rate does not mean that there is no cavitation at all, but instead the cavitation appears at much higher strain in the hinge of the chevrons where the stretching is maximal. The major difference between the present situation and the one at higher strain rate is that the buckling instability appears at a much lower strain,$\varepsilon_{zz}^{buck} \simeq 0.04$ instead of 0.054.

5.6.2 Response as a function of sample size and strain rate

In order to understand better the role of strain rate, we have submitted the same samples of section 5.5 to a uniaxial tensile strain test driven at the low strain rate ($\dot{\varepsilon}_{yy} = 1.4 \times 10^{-5}$). The stress strain curves of the tested samples (S_6, S_{12}, S_{15} and S_{24}), compared with the same curves obtained at high strain rate, are shown in figure 5.16. The curves show that (i) the change in the Young modulus is negligibly small for all samples, (ii) the yield stress and strain decrease as the strain rate decreases and finally (iii) the stress softening exhibits a smooth transition (from yield to the drawing regime) at low strain rate compared to a large drop at high strain rate. Depending on sample size, the yield stress and strain are more or less affected. For the smallest sample S_6 the decrease of the yield stress and strain is small compared to other samples. In general, the decrease of the yield threshold is strongly correlated with the change of the plastic mode from cavitation to buckling. [2]. Both cavitation and buckling result in a yield behavior, however the yielding associated with buckling is much more progressive and smooth than the one associated with cavitation.

The influence of the sample size on the mechanical response is shown in figure

2. The occurrence of buckling for all samples at low strain rate is illustrated in figure 5.17

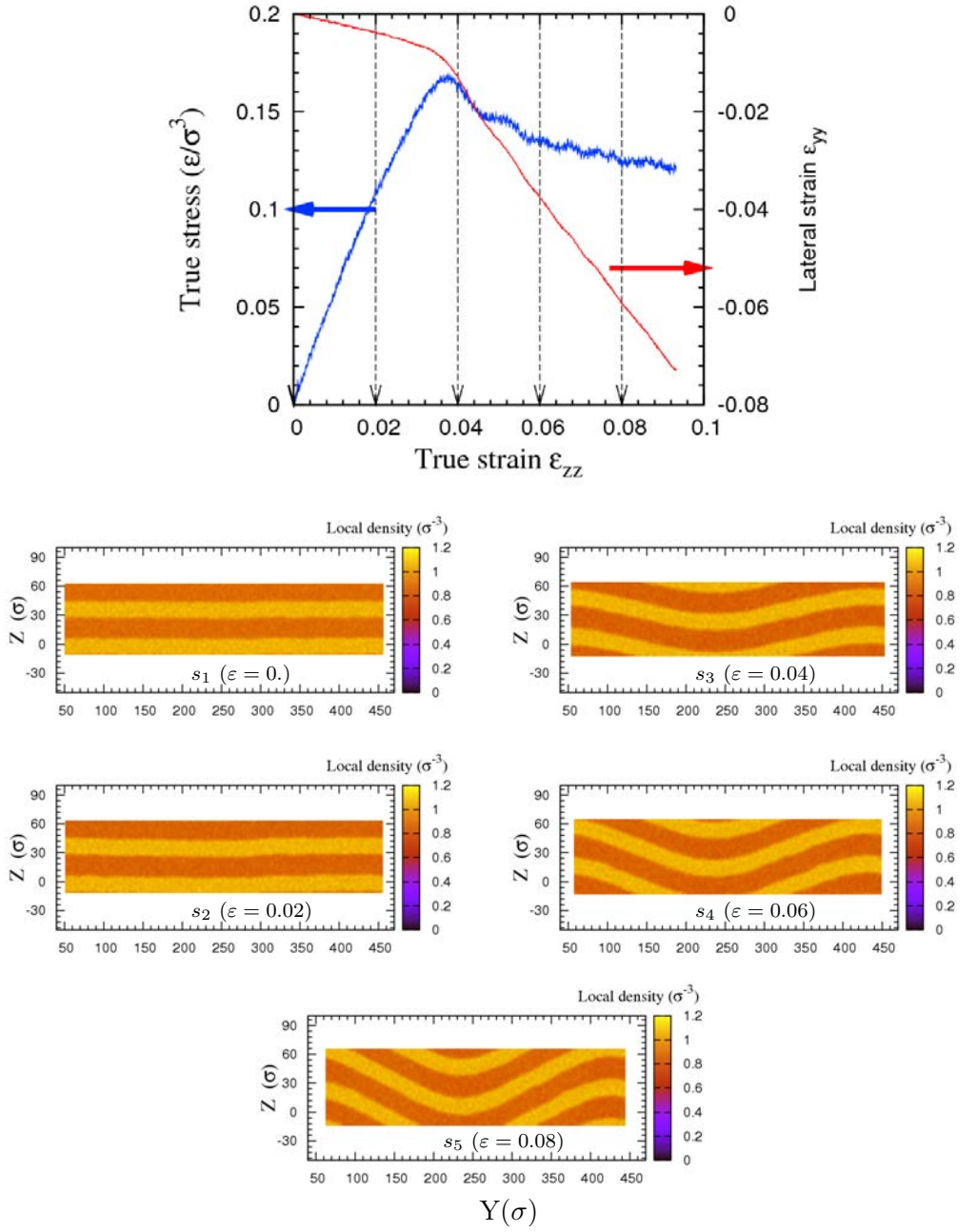

FIGURE 5.15 – Stress-strain curve compared to the lateral strain curve of 12 time replicated sample (same as in section 5.7) superimposed with the lateral strain curve to localize the buckling. Low strain rate is employed to stretch the sample. The local density maps taken at several strain levels are also shown. Cavities are completely absent from the rubbery phase.

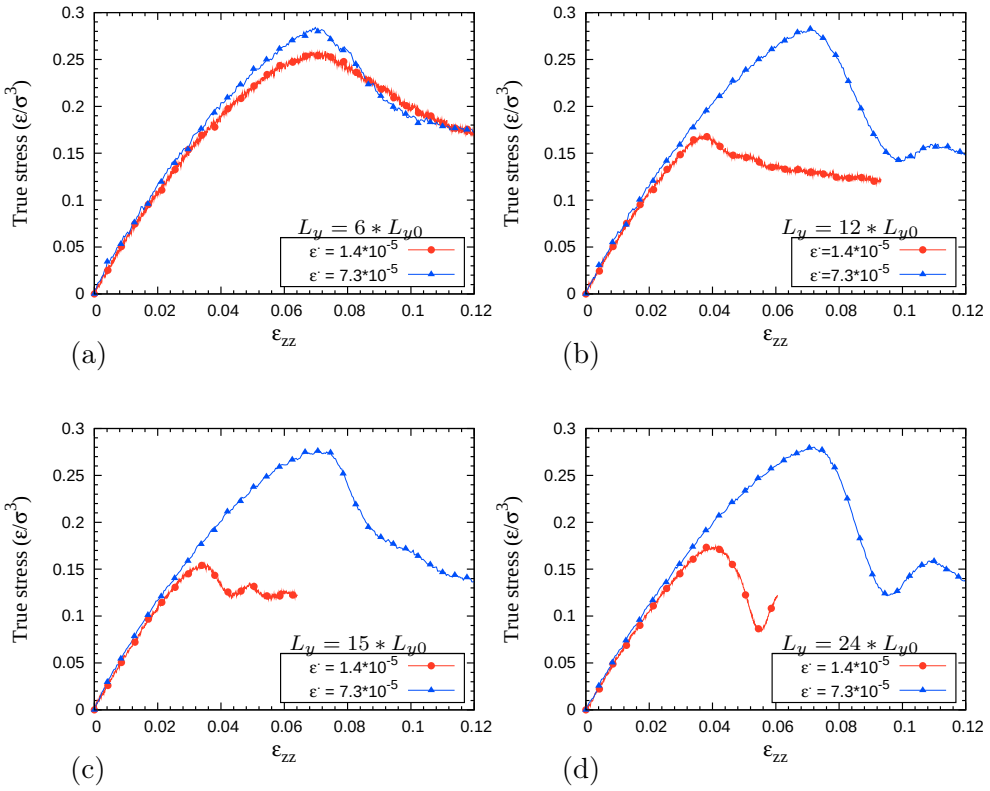

FIGURE 5.16 – Stress-strain curves for several samples with different lengths L_y. Comparison between two strain rates $\dot{\varepsilon_{yy}} = 1.4 \times 10^{-5}$ and $\dot{\varepsilon_{yy}} = 7.3 \times 10^{-5}$. An important change in the mechanical response is observed for long samples, as shown in (b),(c) and (d). At high strain rate, the cavitation is the main origin of stress softening and no buckling is observed for the shortest sample $L_y = 6 * L_{y0}$. At low strain rate : (I) All samples buckle at yield, and (II) cavitation is absent.

5.17a .The stress strain curves were superimposed (idem for the lateral strain in (b)). The elastic slope is still the same for all samples. The yield strain decreases as the sample size increases, except for the longest sample S_{24} that exhibits a higher yield threshold compared to S_{15} and S_{12}. The origin of this non monotonous behavior can be assigned to the buckling kinetics that will be slowed down as the buckling wave length increases. We postpone the discussion of this phenomenon to section 5.6.3. A large decrease of yield is observed as the sample size passes from S_6 to S_{12} this decrease is consistent with the buckling strain evolution predicted by Read's model .

The results for lateral strain are also compared in figure 5.18 for different system sizes and strain rates. The curves highlight a radical change in the mechanical response of the shortest sample S_6. In contrast to high strain rate behavior, the sample S_6 exhibits buckling at low strain rate and no cavities are present in the configuration at yield. For other samples (S_{12}, S_{15} and S_{24}) the buckling strain decreases as the strain rate increases, consistent with the observations in figure 5.16.

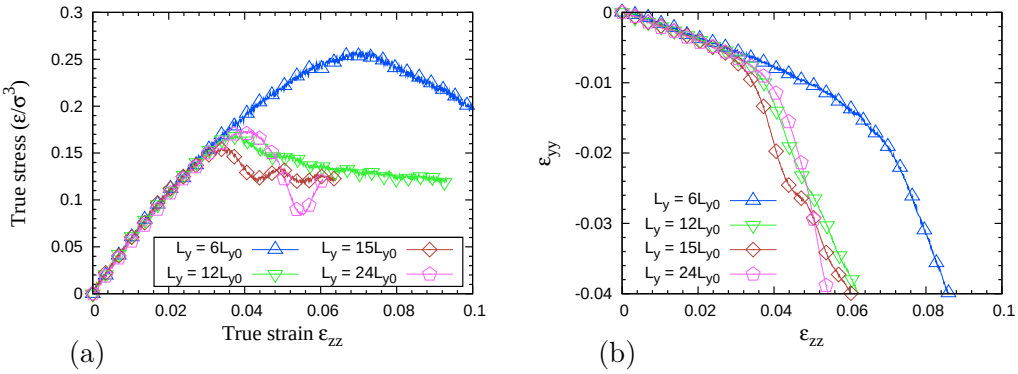

FIGURE 5.17 – (a) Comparison between the stress-strain curve of several samples with different sizes undergoing a uniaxial tensile test. (b) evolution of the lateral strain. The curves are shown for the strain rate $\dot{\varepsilon_{yy}} = 1.4 \times 10^{-5}$. All samples display buckling under these conditions. The buckling strain decreases as the sample size increases (except at $L_y = 24 * L_{y0}$). Note that the stress softening in (a) was correlated to the development of the buckling instability.

Figure 5.19 compares the configurations of samples S_6, S_{12} and S_{15} after buckling, at two different strain rates. The S_{24} configurations are shown separately in figure 5.24. The change of the yield mechanism from cavitation to buckling is well illustrated in these snapshots especially for the smallest sample S_6. The second important observation is that the wavelength becomes equal to the sample length at low strain rate. Finally, there are no cavities present in the rubbery phase of the lower strain rate configurations, compared to high strain rate configurations at the same strain. These snapshots confirm that the low energy buckling mode is selected by the system at the lowest strain rate. As expected, the bending energy of the buckled layers is reduced by increasing the buckling wavelength to its maximum allowed value.

5.6.3 Interpretation : buckling kinetics and sample size

It had been shown previously (section 5.4) that the onset of buckling at a certain wavevector k is determined by the function $F(\varepsilon_{zz}, k)$ defined as follows :

$$F(\varepsilon_{zz}, k) = f_2^{3D}(\varepsilon_{zz})k_i^2 + Kk_i^4 \tag{5.20}$$

where $f_2^{3D}(\varepsilon)$ is given in equation 5.18. This function is plotted in figure 5.20a as a function of wavevector at fixed strain , and in figure 5.20b as a function of strain at fixed wavevector. If $F(\varepsilon_{zz}, k) > 0$ the system is stable. Increasing the strain ε_{zz} gives rise to a negative part and then the curve has two roots, one at $k = 0$ and one at a finite value $k_0(\varepsilon_{zz}$. For a given system size L, the possible wavevectors are fixed, and the elastic instability can develop when the strain is such that $k_0(\varepsilon_{zz}$ reaches $2\pi/L$. As the sample size decreases, the onset of the buckling is delayed,

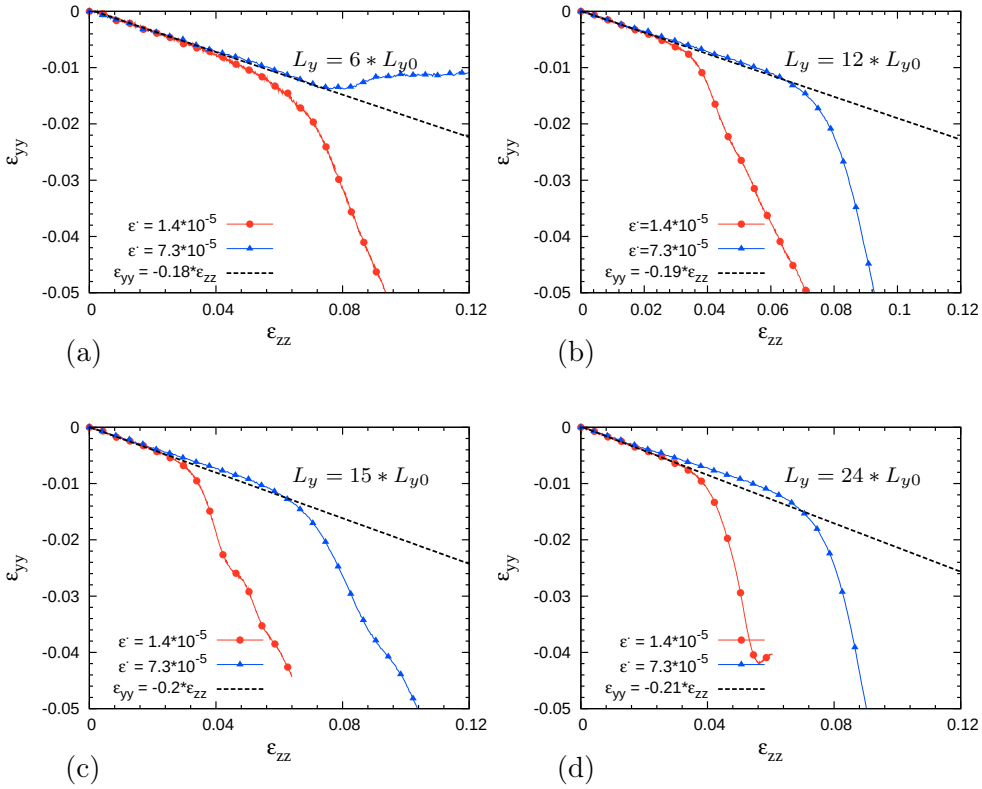

FIGURE 5.18 – Lateral deformation strain for several samples with different lengths, (the stress strain curves were shown in the previous figure). Depending on the applied strain rate, the behavior changes from cavitation to buckling for the shortest sample $L_y = 6 * L_{y0}$. The buckling strain decreases at low strain rate.

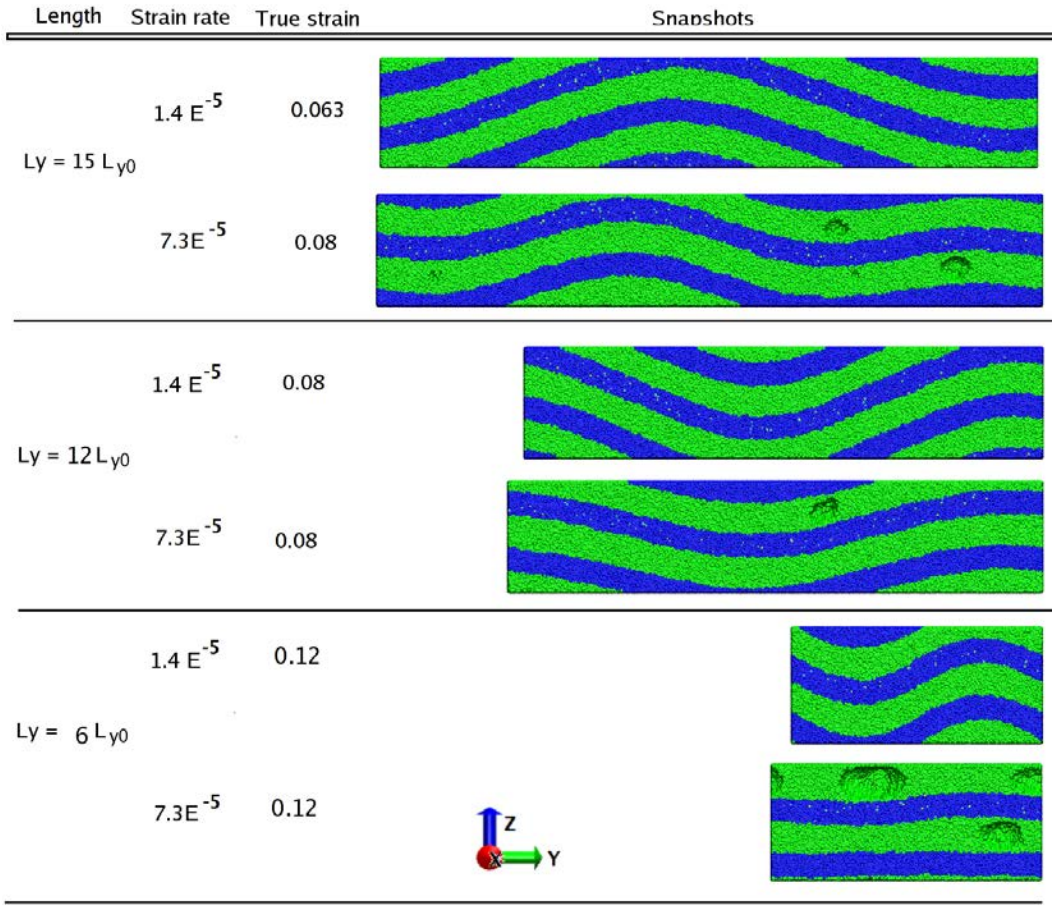

FIGURE 5.19 – Snapshots show several samples under a uniaxial tensile tests driven by two different strain rates ($\dot{\varepsilon_{yy}} = 1.4 \times 10^{-5}$ and $\dot{\varepsilon_{yy}} = 7.3 \times 10^{-5}$) . Several lengths are presented, at low strain rate all samples buckle. The buckling wave length is equal to the sample length which is not the case at high strain rate

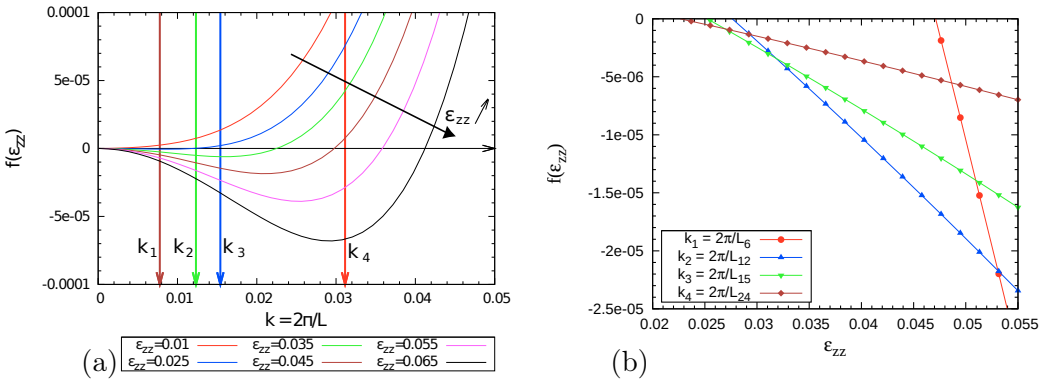

FIGURE 5.20 – Coefficient of the term that drives the buckling deduced from 5.19 plotted at constant strain as in (a) or at constant wavevector as in (b).

which is completely consistent with our simulation results at low strain rate. The critical strain first decreases rapidly with sample size, then saturates at a value of about 0.02, which would be the critical strain for an infinite sample, characterized by a change of sign of $f_2^{3D}(\varepsilon)$.

Identifying $-F(k,\varepsilon)$ as the driving force for the instability, we can understand qualitatively the behavior observed in our simulations. In small samples, figure 5.20.b shows that the driving force increases rapidly as soon as the threshold in strain is reached. Hence a small strain in excess of the threshold value will be enough to have a large driving force, hence a fast growth of the instability at the expected wavevector. On the other hand for larger systems the driving force will be smaller, and as the strain increases more modes may become unstable before the instability has been able to develop in a significant manner. Hence a competition between the growth of different modes, and potentially with cavitation, will be possible. These kinetic effects are obviously not part of the elastic theory, which is an equilibrium description corresponding to a very low strain rate, allowing a full development of the instability with the smallest wavevector before another one becomes unstable. The interplay between strain rate and cavitation effects for the observation of the buckling instabilities will be discussed in a slightly more quantitative manner in section 5.7 below, using a simple linear growth model.

5.6.4 Initiation of the instability and interface curvature

We had seen above that the yield and the buckling strains of the S_{24} sample at low strain rate are greater than those for S_{15}, in contrast to the general expectation that results from the discussion in the previous section. To understand the origin of this behavior the evolution of the configuration was inspected and the snapshots are shown in figure 5.21. In contrast to our expectations, the buckling does not appear simultaneously in all the sample length. Instead only a portion of the length starts to bends first, and the buckling propagates progressively in the rest of length,

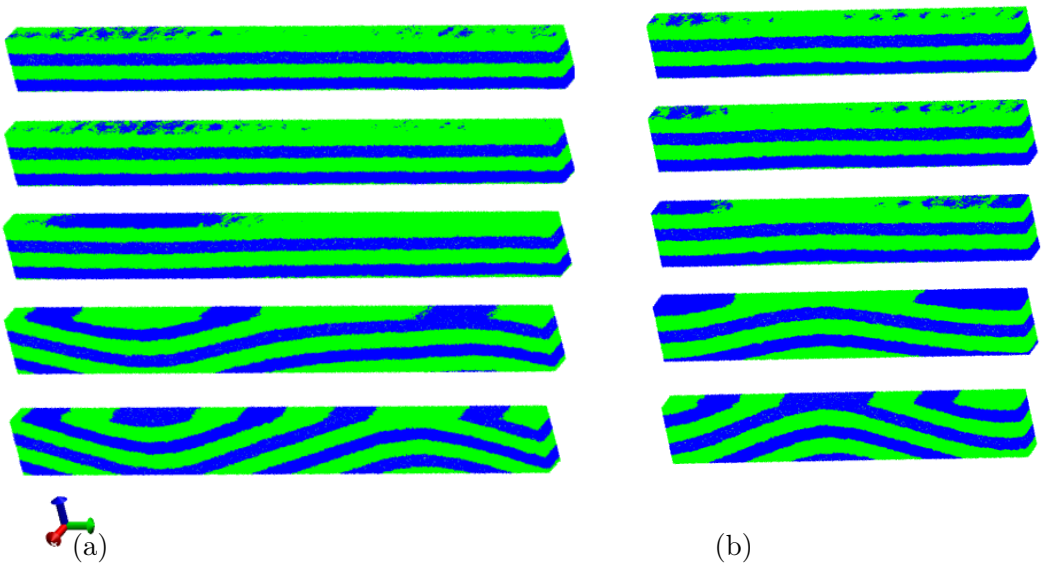

FIGURE 5.21 – Evolution of buckling in S_{24} in (a) and S_{15} in (b). in both cases the hard phase bending starts in a zone that is characterized by an slight change of interface orientation. (a local non planar interface) These zones can be easily distinguished by the glassy phase spots (blue spots) in the top of the undeformed sample. note that the blue color refers to the glassy phase and the green color refers to the rubbery phase.

to reach eventually a sinusoidal profile. Near to the first bended zone, an anomaly in the interface orientation can be distinguished. The glass-rubber interface is not perfectly planar, a slight curvature of the interface toward the positive z direction is noticed in the zone where buckling appears. Increasing the sample size will increase also the probability to find such defects which are important as initiators of the instability. In the presence of such defects, the onset of the buckling occurs locally well before becoming apparent on global measures. Furthermore, the lower buckling kinetic slows down the propagation of the undulation and makes the lateral strain less sensitive with the pre-buckling event. The progressive evolution of the pre-buckled portion relaxes a part of the lateral stress that was considered as the basic origin of the buckling. Under such conditions, the sample has to gain an excess of strain to compensate to trigger a complete buckling. As a consequence, the buckling and the yield strain are delayed in S_{24} case. Note that anomalies in the interface curvature are also found in S_{15} and S_{12} samples, the hard phase bending starts also from these zones but the buckling propagates more rapidly than in the S_{24} case.

5.6.5 Summary and discussion

The previous results show that the mechanical responses of the samples are strongly influenced by the strain rate. The cavitation is delayed, the buckling strain

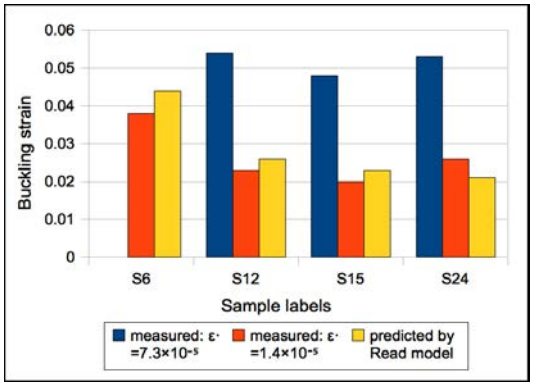

FIGURE 5.22 – Bar plot compares the buckling strain values for different samples. The buckling strain evaluated by Read's model corresponds well with the buckling strain measured at low strain rate.

decreases and the yield becomes correlated with the buckling rather than the cavitation at low strain rate. At high strain rate the sample size do not affect the yield or the buckling strain as shown in section 5.5 and the unstable wavelength is the same for all samples. This result, illustrated in particular by the S_{24} in which the buckling wavelength is half of the system size, was unexpected as it contradicts the prediction from the elastic theory. At low strain rate, a major change in the mechanical response is observed. The yield and the buckling strains decrease as the sample size increases, and the buckled configuration displays only one wave length equal the sample length. The results are consistent with elasticity predictions, except for the $S24$ sample, which shows a yield strain higher than the $S15$ sample. In this case an initial interface curvature coupled with slow buckling kinetics leads to a localized buckling in the earlier deformation stage of S_{24} sample. This pre-buckling event relaxes the compressive lateral stress and the buckling and yield are delayed.

Table 5.6.5 compares the buckling and the yield stress and strain for each sample. Figure 5.22 illustrates the comparison between the buckling strains (measured and predicted one). The plot shows that the predicted buckling strain by Read's model corresponds well with the buckling strain value measured at low strain rate.

5.7 A simple model for buckling kinetics

The mechanical response of S_{24} sample exhibits a variety of behaviours. Depending on the applied strain rate, the buckled sample may have one or more undulation per sample. At low strain rate, the occurrence of buckling is predictable by the analytic model developed by Read et al. However, the measured and predicted values of buckling become markedly different at high strain rate. To analyse the influence of kinetic factors on the buckling instability, new tensile tests have been performed on the S_{24} sample, with intermediate and high values of the strain rate : $\dot{\varepsilon}_{zz} = 1.4 \times 10^{-5}$, 7.3×10^{-5}, 1.4×10^{-4}, 3.6×10^{-4} and 7.3×10^{-4}. The resulting

Sample	$\dot{\varepsilon_{zz}}$	ε_{zz}^{yield}	σ_{zz}^{yield} (ε/σ^3)	ε_{zz}^{buck} (meas)	ε_{zz}^{buck} (pre)	σ_{zz}^{buck} (ε/σ^3)	$\frac{\varepsilon_{zz}^{yield}-\varepsilon_{zz}^{buck}}{\varepsilon_{zz}^{buck}}$
S_6	7.3×10^{-5}	0.07	0.284	-	0.044	-	-
S_6	1.4×10^{-5}	0.070	0.255	0.038	0.044	0.18	0.83
S_{12}	7.3×10^{-5}	0.071	0.282	0.054	0.026	0.25	0.31
S_{12}	1.4×10^{-5}	0.037	0.167	0.023	0.026	0.12	0.6
S_{15}	7.3×10^{-5}	0.070	0.276	0.048	0.023	0.23	0.46
S_{15}	1.4×10^{-5}	0.035	0.153	0.020	0.023	0.11	0.71
S_{24}	7.3×10^{-5}	0.072	0.28	0.053	0.026	0.24	0.36
S_{24}	1.4×10^{-5}	0.041	0.172	0.026	0.021	0.13	0.54

TABLE 5.2 – Strain and stress that correspond to the buckling and yield, comparison between two different strain rates 7.3×10^{-5} and 1.4×10^{-5}. These values were averaged over a short time interval (t=6τ that corresponds to a strain of 4.5×10^{-4}).

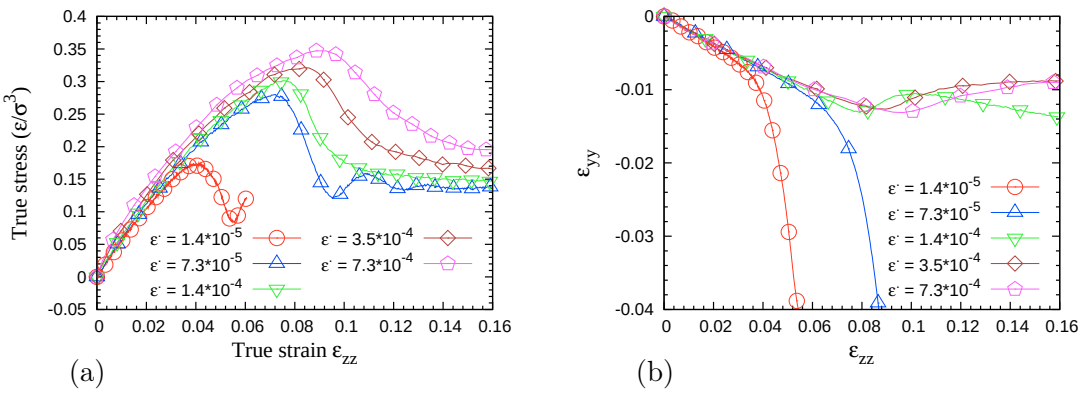

FIGURE 5.23 – (a) Stress strain curves of sample S24 submitted to several uniaxial tensile tests with different strain rates. The corresponding lateral deformation curves are shown in (b). At low strain rate (effectively when $\dot{\varepsilon}_{yy} \leq 7.3\times10^{-5}$) the sample buckles at a strain and wavelength (see figure 5.19) that are rate dependent. The nucleation of cavities and the absence of buckling mark the mechanical response at high strain rate.

mechanical responses are plotted and compared in figure 5.23 which shows the stress strain curves and the evolution of the lateral strain. Snapshots of the deformed configurations are shown in figure 5.24. These data illustrate clearly that the the sample can adopt different modes to relax the increase of stress in the elastic regime. At intermediate and low strain rates, the competition is between the different modes of the buckling instability. At high strain rate, a competition with the cavitation mechanism is observed. In the following we discuss these two competitions, using a schematic model for the growth of the buckling instability.

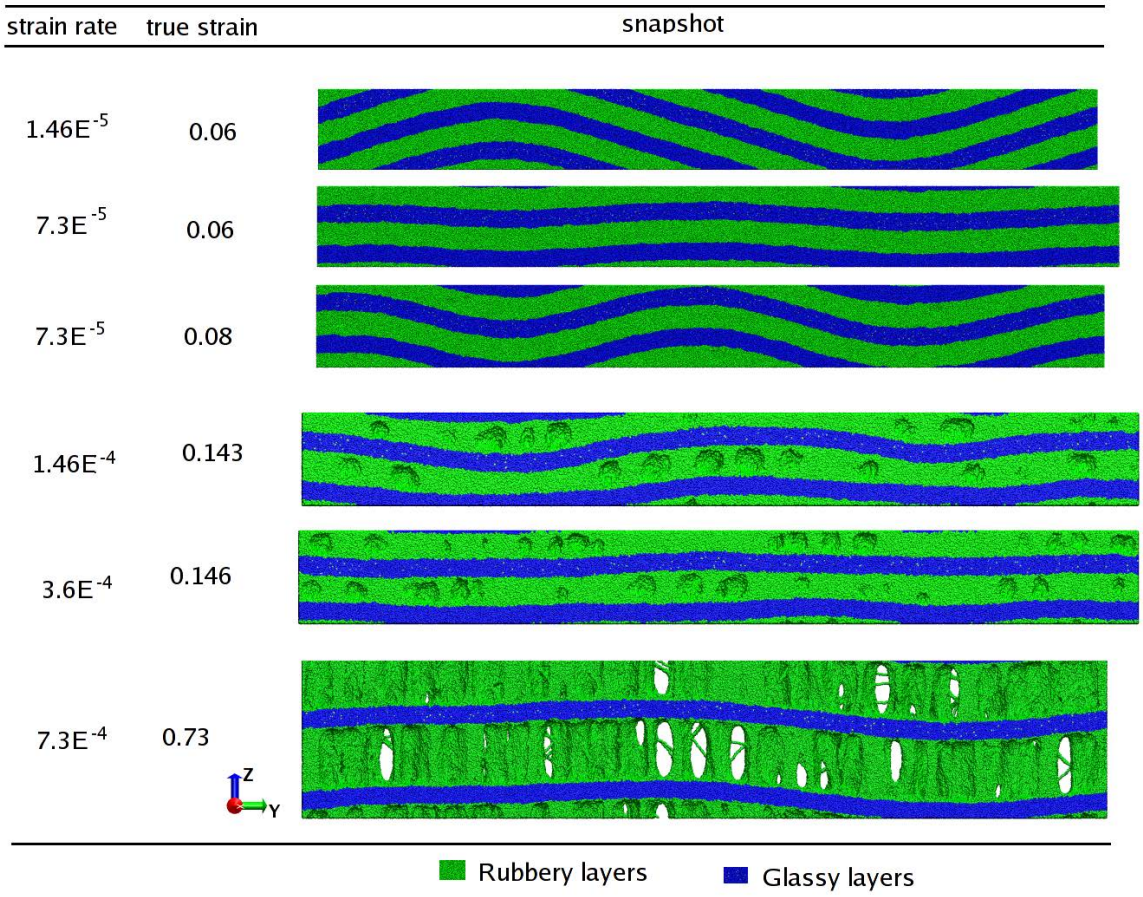

FIGURE 5.24 – Snapshots showing the buckling and the cavitation state of sample S24 for different strain rates. As the strain rate increases the wavelength of the buckle decreases ; At high strain rate cavitation in the rubbery phase governs the behavior.

5.7.1 Competition between buckling modes

The S_{24} sample have shown two different buckling modes at two different strain rates. To understand qualitatively this observation, we propose to describe the growth of the amplitude $U_n(t)$ of the mode with wavevector $k_n = 2n\pi/L$ using a simple linear relaxation equation of the form

$$\frac{dU_n}{dt} = -\lambda.F(\varepsilon, k_n).U_n \tag{5.21}$$

where $F(\varepsilon, k_n).U_n$ is the driving force that is derived from the energy equation 5.18. λ is a phenomenological coefficient which will be assumed to be independent of wavevector, which is reasonable as the growth is essentially a local process, The solution of this equation can be written as :

$$U_n(t) = U_n(0).\exp\left(-\lambda.\int_0^t F(\varepsilon(s), k).ds\right) \tag{5.22}$$

Note that the strain [3] ε is a time dependent variable $\varepsilon(t) = \dot{\varepsilon} \times t$. Equation 5.21 has been solved numerically for a value of $\lambda = 0.1$. This value is somewhat arbitrary as we do not have a physical interpretation of the parameter λ , which will be related to the local viscosity in the rubber phase. However, this choice gives a good illustration of the phenomenon of competition between modes.

Two buckling modes were considered ($k_1 = 2\pi/L_y$ and $k_2 = 4\pi/L_y$) at two strain rates ($\dot{\varepsilon}_1 = 1.4 \times 10^{-5}$ and $\dot{\varepsilon}_2 = 7.3 \times 10^{-5}$). The evolution of U_n with respect to the strain is shown in figure 5.25. The part (a) of the figure shows the function $F(\varepsilon, k)$ with respect to ε for the two wavevectors. (b) describes the solution of the equation 5.21 for $U_n(t)$, starting from a common small amplitude $U_n(t = 0) = 0.01$.

From these numerical solutions, the scenario that permits the observation of different buckling wavelengths depending on the strain rate is quite obvious. The instability associated with the largest wavelength mode is always initiated first. For low strain rates, this instability develops exponentially with time, and when the critical strain for the instability at k_2 is reached it already has a substantial amplitude. In the linear picture developed here, the instability at k_2 also develops exponentially, with a faster growth rate, and would eventually dominate. However, this only happens when the first instability has reached a large amplitude, so that the whole linear picture becomes questionable, and other phenomena such as cavitation at the hinges start taking place. On the other hand for a high strain rate the sweep rate of the $f(\varepsilon, k)$ curve is so high that the driving force for the k_1 instability in fact decreases with time. The growth is less that exponential in time, and when the strain for the k_2 instability is reached this instability quickly overwhelms the first one. If one moreover assumes that the observation of buckling into a given mode requires the amplitude of this mode to reach some threshold value, it is also clear from the evolutions shown in figure 5.25 that the observation of buckling will be

3. In this section we denote by ε the strain in the tensile direction z.

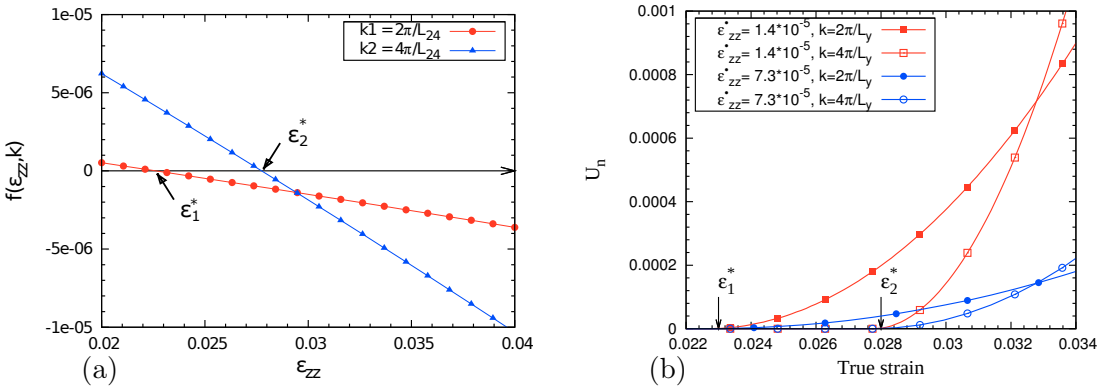

FIGURE 5.25 – (a) Buckling driving force coefficient $f(\varepsilon_{zz}, k)$ plotted for two k values : $k1 = 2\pi/L_y$ and $k2 = 4\pi/L_y$ that correspond respectively to one and two wave length per sample. (b) shows the amplitude of each mode as a function of strain (solution of equation 5.21) for the two wavevectors at two different strain rates.

delayed (in strain) as the strain rate is increased, leaving room to stress release via the cavitation phenomenon.

This description remains at a phenomenological level, and neglects any nonlinear interaction between modes. The exact results will depend on the choice of phenomenological parameter λ. However, we have checked that the general behavior is independent of this choice over a large interval ($0.001 \leq \lambda \leq 20$). Therefore we believe the model captures the essential features of the competition between modes. A detailed study of the instability onset as a function of strain rate would be necessary to adjust the values of the parameters, but also very costly in terms of computation times. (Note that this model has been recently developed, please see appendix 2 for more details).

5.7.2 Competition between cavitation and buckling

Competition between buckling and cavitation in the rubbery phase was encountered in several situations : (i) When modifying the interaction parameters to produce a weak interface, it was observed that the nucleation of cavities starts at the interface and takes place prior to buckling, which is shifted to a higher strain. (see figure 5.26) [4]

(ii) At relatively low strain rate, the sample displays the first mode of buckling and the yield becomes correlated with the occurrence of buckling. At higher strain rate ($\dot{\varepsilon} = 7.3 \times 10^{-5}$) the second mode of buckling dominates, and is directly followed by cavitation that gives rise to a large stress relaxation. When the applied strain rate becomes higher than ($\dot{\varepsilon} = 7.3 \times 10^{-5}$), the buckling in S_{24} sample seems to directly intercepted by the cavitation events that relaxes and annihilates the development

4. the influence of surface tension energy was studied only in a very preliminary fashion and will not be discussed here.

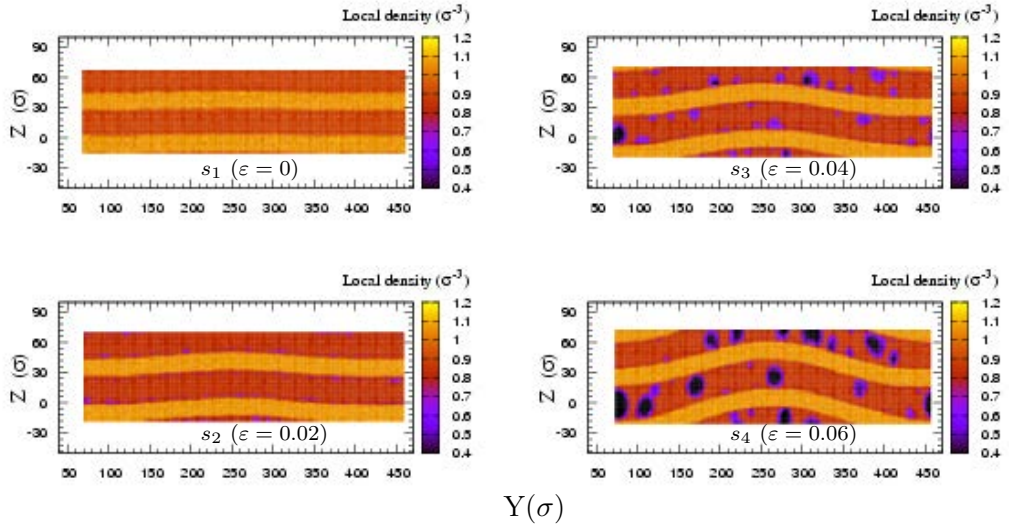

FIGURE 5.26 – Local density maps of weak interface sample (ε_{AA}=1, ε_{BB}=1, ε_{AB}=0.15), the panels show that the nucleation of cavities starts mainly at the at the interface. the cavities, which develop in the rubbery phase, don't prevent the development of the buckling.

of undulation. This process was shown in figure 5.24. The fourth snapshot taken at $\dot{\varepsilon} = 1.46 \times 10^{-4}$ shows small undulations in the glassy lamellae whereas the rubbery lamellae are perforated by the cavities. The nucleation of cavities in the rubbery phase relaxes the lateral compressive stress applied on the glassy layer, so that the development of the buckling instability becomes impossible.

In case (i) the cavitation will be preferentially nucleated at the interface, but the buckling remains allowed with the help of two main factors : the cavitation itself,which creates voids in the rubbery phase behind the interface, disturbs the stress balance in their vicinities and helps the development of the buckling. For the second case (ii), the cavitation begins in the core of the rubbery phase but the hard phase still not influenced. The cavitation in such cases relaxes stress and prevents the buckling instability.

The cavitation is expected when the local strain reaches a specific threshold from which the matter looses its cohesiveness. Increasing the strain rates will decrease this strain threshold in a similar way as the yield strain is figure 5.23. On the other hand, the growth of buckling becomes very slow at high strain rate, then the deformation can exceed the cavitation threshold before the development of the buckling. and this is what we observe in the behavior of S_{24} sample. Even if the higher (third) mode buckling is possible, the S_{24} sample can not develop this mode at high strain rate since the buckling becomes overwhelmed by the cavitation.

5.8 Conclusion

In this chapter, the mechanical response of triblock copolymer models has been investigated by using a coarse grained molecular dynamic simulation. Our MD samples were built by radical like copolymerization method. After a specific post processing, a lamellar triblock copolymer model with a sequence of glassy-rubbery layers is obtained. Uniaxial tensile tests were performed in the normal direction to the layers ; the resulting constitutive laws capture the main regimes of a real triblock sample deformed in the perpendicular direction. The elastic regime results from the serial coupling between phase stiffness. At yield, the growth of stress is intercepted by the cavitation or buckling events (depending on the strain rate). After a pronounced drop at yield the stress rises again in the strain hardening regime.

Depending on the applied strain rate, triblock samples exhibit a variety of microscopic deformation mechanisms. At relatively high strain rate, one observes (except for the smallest samples) a buckling into a wavelength that does not depend on sample size. The buckling is accompanied by the the nucleation of cavities and both aspects contribute to the stress drop at yield. At low strain rate, all samples (including the shortest one) exhibit buckling. The yield becomes correlated with the buckling ; and the cavitation is delayed. The undulation wavelength is equal to the sample length in this case.

This behavior was interpreted by the influence of kinetic factors that becomes relevant in the initial stages of the buckling instability. At a slow deformation rate, the sample can be effectively considered as in an equilibrium state, then the measured buckling strain corresponds very well to the value predicted by a simple elastic model, and the instability at large wavelength that is expected from elastic theory has time to develop. As the strain rate increases several modes come into competition, and the shortest wavelengths that correspond to a larger driving force can take over and dominate the instability pattern. In this case the strain for observing buckling can be markedly larger than predicted by elastic theory. This behavior was rationalized by using a simple model of mode growth based on a viscous dynamics and the elastic driving force for the mode amplitudes. A competition was also found between cavitation and buckling, this competition depends upon several factors, the strain rate, the sample size and the interface energy between phases. At high strain rate, the buckling kinetic is rather slow with respect to the deformation conditions. The cavitation intercepts the development of the buckling by relaxing the lateral compressive stress. Cavitation takes place before buckling develops, releasing the stress, so that the instability is suppressed. At lower strain rates buckling occurs first, and cavitation is localized preferentially at the hinges of the chevron structure that forms at large strain.

Chapitre 6

Conclusions and outlook

Contents

6.1 Conclusions

In this work the mechanical properties of homogenous polymers and nanostructured copolymers have been investigated using molecular dynamics simulations. A coarse grained, bead spring model was employed. In this model, the polymer chain can be assimilated to a sequence of beads that are connected each other by a strong bonds (FENE potential). The non connected beads interact via a Lennard-Jones potential to reproduce the Van deer Waals bonds. The simulation samples were built by a numerical analog of the radical like polymerization method. two kinds of samples were built : homogenous polymer samples and nano-structured co-polymer with various chain architectures.

The role of boundary conditions on the tensile test has been extensively studied. Two boundary conditions are used to drive the deformation : the homogenous deformation and the boundary driven deformation. in the homogenous deformation the simulation box is submitted to a sequence of two steps : (i) an affine deformation followed by a (ii) MD relaxation of the bead positions (figure 6.1.b). The homogenous deformation was applied in two tensile stress conditions : in the uniaxial tensile the bead position are rescaled in the tensile direction only the two remaining direction are authorized to deforms according the imposed pressure. In triaxial tensile the positions of the beads are rescaled in the tensile direction while the deformation in the two other directions is prohibited.

Another deformation method was tested, in which the deformation was applied on sample by a pair of "grips", as in a laboratory experiment (figure 6.1.a). In the uniaxial tensile, steered molecular dynamics was used to drive the movement of grips, this technique allows the deformation of grips in parallel to its tensile motion. Rigid grips were employed to drive the deformation in the triaxial tensile tests at constant velocity (or strain rate). Identical constitutive laws were obtained from the two methods in uniaxial and triaxial tensile for glassy and rubbery samples. This finding is not valid at extremely high strain rate (when the tensile velocity becomes comparable to the sound wave velocity) where the homogenous method leads to

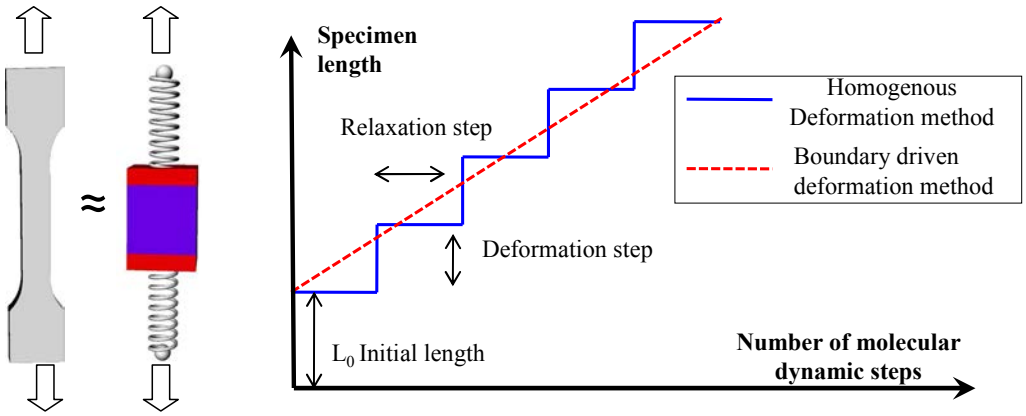

FIGURE 6.1 – (a) A sketch showing the principle of the boundary driven deformation method applied on the uniaxial tensile tests,(b) compares the tensile trajectory of the two methods used to drive the deformation : (i) Homogenous tensile test (ii) boundary driven deformation test

ductile-like behavior compared to a localized deformation behind the grips at high strain rate.

The mechanical response of homogenous glassy polymer submitted to a uniaxial tensile test is composed from three main regimes : (i) the elastic regime the (ii) yielding and (iii) the strain hardening regime. In the elastic regime the linear (quasi linear) increase of stress is caused by the LJ interaction that tend to bring the beads back to their initial configuration. The onset of plastic events begins at yield. The strain hardening regime, peculiar to polymer systems, has attracted much interest. This regime was found to fit the linear Gaussian strain hardening equation based on the entropic network model of the rubber. The entanglement density is then supposed to be constant. The evolution of the entanglement length in polymer sample under tensile strain was probed using the primitive path analysis. The results shows an increase of entanglement length (disentanglement) in the strain hardening regime. In fact, it is now known that the physical origin of strain hardening is not rubber elasticity, but rather that it results from the increasing rate of plastic events induced by the reorientation of chains in the tensile direction.

The nucleation of cavities in an amorphous polymer model under triaxial tensile strain was also studied. A set of local properties was examined in order to find the relationship between the cavitation and the local microstructure. In contrast to common assumptions, the nucleation of a cavity is not correlated with the local loss of density or chain connectivity in the vicinity of the cavity. Instead, a cavity in a glassy polymer nucleates in regions that display a low bulk elastic modulus (figure 6.2). This criterion allows one to predict the cavity position before the cavitation occurs. Even when the localization of a cavity is not directly predictable from the initial configuration, the weak zones identified in the initial state emerge as favorite

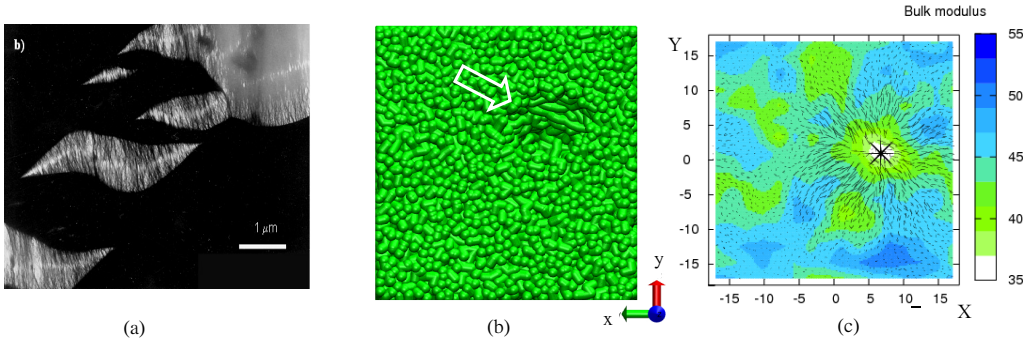

(a) (b) (c)

FIGURE 6.2 – (a) Late stage of crazing in polycarbonate polymer. The nucleation of a cavity in the simulation box (b) was correlated with a low elastic modulus region (c).

spots for cavity formation. As the deformation progresses, the weakness of one or more of these zones is amplified and cavities open in places where the local bulk modulus reaches its lowest value.

The mechanical response of nano-structured copolymers has been investigated in the later part of this work. several samples with various properties and chain architectures were tested. These samples are made of alternating hard (glassy) and soft (rubbery) phases connected by strong bonds. The constitutive laws of these samples exhibit an anisotropic composite response that captures the mechanical behavior of nano-structured polymers. The influence of chain architecture on the mechanical properties was investigated : our finding reveals an important role of the bridging molecules to ensure the stress transmission between phases at high strain. We find that the decrease of bridging chains amount against the cut chains leads to a stress concentration in the hard phase, which reduces severely the toughness of the sample. In contrast, this influence is absent in loop chain samples. No significant change in the mechanical response is observed when the bridging chains are replaced by loop chains. This observation was interpreted by the fact that the loop chains are long enough to link the two different hard blocks by entanglement. Therefore the role of knotted loop chains was found to be equivalent to the bridging chains.This assumption was verified by applying the PPA on a fully looped sample after freezing the hard blocks. The resulting configuration after PPA confirms that the hard blocks are linked together by the entangled loop chains.

The buckling instability of the copolymer sample was also studied. For this purpose, extremely large samples were built. Under uniaxial tensile condition these samples exhibit buckling at relatively low strain. The micro mechanical origin of buckling was investigated, we find that a compressive stress state in transverse direction of the hard phase is the main origin of the buckling. This stress results from the lateral contraction of the rubbery phase due to the poisson ratio effects under tensile strain condition. The buckling strain was detected by the fast change in

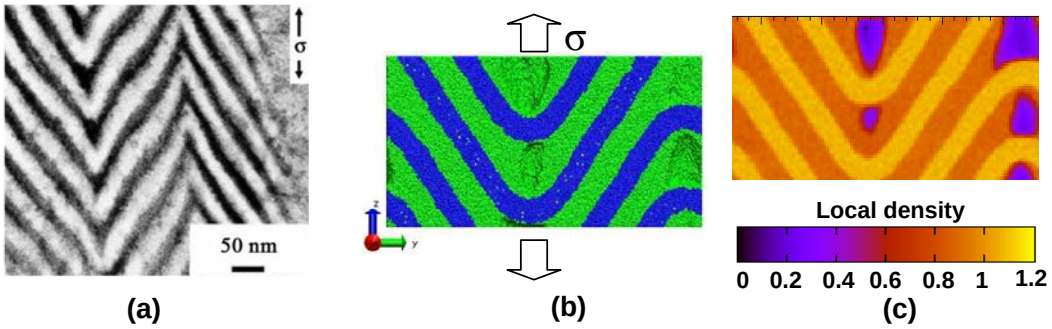

FIGURE 6.3 – (a) TEM image of buckled morphology SBS triblock copolymer "chevron morphology". The buckled configuration of a triblock copolymer is shown in (b) while the local density is shown in (c) The buckling was successfully simulated by molecular dynamics.

the Poisson ratio of the sample. The influence of several parameters on the buckling was studied. According to theoretical predictions, the buckling strain decreases as the sample length increases. Indeed, at low strain rate, we find a value of the buckling strain that corresponds well to the one expected from the elastic theory. The buckled configuration snapshots confirms that only one undulation per sample subsists. The undulation wave length is equal to the sample width due to the periodic boundary conditions. At high strain rate, however, the samples exhibits a completely different behavior : all the buckled configurations have roughly the same wave length, the buckling strains seems to be independent from the sample size. we find also that the occurrence buckling at fast strain rate is accompanied by the nucleation of cavities in the rubbery phase at yield.

In fact the influence of the strain rate highlights two different competitions in the sample. (i) competition between the cavitation and the buckling in relatively short samples. (ii) a competition between the first and the higher buckling modes in large samples.

In the first case, we provide a qualitative description of this competition, while a simple numerical model was suggested to interpret the second competition. This model takes into account the kinetic aspect of the buckling event in the initiation stage. The competition between the spontaneous kinetics of buckling and the imposed strain rate was found to be the origin of the observation of higher buckling modes in the sample.

6.2 Outlook

We believe that the work achieved in this thesis offers some challenging directions of future research. First, in the study of the cavitation, the correlation was found between the local elastic bulk modulus and the cavity position. The time

window between the prediction and the occurrence of the event is short compared to the trajectory of the elastic behavior. A way to increase this window for a better prediction, is to look for other mechanical properties that can more sensitive to the change of local microstructure. The shear modulus is the most successful candidate for this purpose. Other suggestion can be more adequate, is to look to the gradient of the elastic modulus rather than looking directly to its local value. This suggestion is inspired from the nucleation of damage in metals-inclusions material such as graphite iron alloys or aluminum-ceramic composites. In such materials the cavities nucleate preferentially in the regions that exhibit a strong gradient of their elastic properties, notably around the inclusions.

In short nano-structured samples (Chapter 4) all samples were tested at the same rate. However the role of the strain rate in the mechanical response of such material is crucial because of the glassy phase behavior that is strongly dependent on the tensile velocity. This issue was approached only for large samples that exhibit buckling, but for the short samples in which we studied the influence of chain architecture and conformations, the role of the strain rate on the system toughness and strain hardening remains an open question.

Concerning the buckling in triblock samples, some simulations were limited to a relatively small strain after the buckling for computational reasons, therefore large strain behavior still not well investigated. We have shown that the cavitation and buckling appear within the simulated strain range at high strain rate, but this is not the case for low strain rate behavior where the cavitation is delayed to a high strain that has not been attained in our simulations. More simulations are needed to achieve this study. Despite the fact that the constitutive law of large triblock samples was correlated to the change in the structural and morphological response, some questions remain to be addressed about the molecular origin of the strain hardening and the role of each phase in the process.

Other points remain to be explored like the role of molecular architecture (bridge and cut chains) on the initiation and development of buckling, or the role of surface energy in this instability. Changing the molecular architecture will eventually change the mechanical properties and the transmission of stress between phases, which could affect the buckling strain. The role of the interface energy between phases is also an interesting point to be investigated, especially for its potential influence on the competition between cavitation and buckling.

Annexe A

Radical like polymerisation

Contents

A.1 Introduction

Radical like polymerization is an efficient flexible tool to build homogenous and heterogeneous (di-block and tri-block) polymer samples. The efficiency of this method arises from its ability to generate and equilibrate chains simultaneously. Several methods have been developed to generate numeric polymer samples, namely, fast push off, slow push off, and double bridging hybrid [Auhl 2003]. These methods are based on two subsequent stages : (i) Random Gaussian chain generation followed by (ii) MD or/and Monte Carlo (MC) equilibration steps. Systems resulting from step (i) are far from their equilibrium states, thus a long equilibration run is required. These algorithms are limited to the generation of entangled polymer melts and they are not particularly well suited for more complex architectures.

As it mimics the central idea of radical polymerization, $AM^* + M \rightarrow AMM^*$, the RLP method builds the chains progressively in an interacting molecular dynamics solvent. As a consequence, the system will be equilibrated while groth occurs. Compared to other methods, the RLP can be adjusted to generate some complex systems such as polymer blends, star polymers and 3D cross-linked polymers (Thermoset polymer model) [Mukerji 2009].

The outline of the method will be first presented. Then, the application of this method to generate homogenous polymers and polymer blends with various chain architectures will be detailed. The post processing procedure is briefly described in section A.5.2. Note that, in this appendix, we refer mainly to the acknowledged work

of Perez *et al* [Perez 2008] who developed this method. The generation of tri-block systems will be detailed as it was briefly presented in the Perez *et al* paper.

A.2 Radical Polymerization reaction : highlights

The radical-Like Polymerization is inspired from the radical polymerization reaction. The living polymerization begins where radicals (interacting sites) are created by active molecules $M \rightarrow A^*$. Afterward, radicals start to interact with single monomers ($A^* + M \rightarrow AM^*$). The polymer chain grows by connecting its radical with single monomer as the polymerization propagates in the solvent as follow : $AM^* + M \rightarrow AMM^*$ (M^* is the radical site, M is a monomers and A is the rest of chain). After each monomer addition, the radical site moves to the new added monomer (at the chain end) allowing thus to capture a new single monomer from the solvent. Polymer chains grow until the end of the reaction (when all chains reached to desired size), where the polymerization is arrested. Referring to the presented stages of radial polymerization reaction, the RLP method was founded on the same concept of progressive chain growth. This concept was used to generate entangled polymer samples and tri-block copolymers as it will be shown below.

A.3 Modelling

Our simulations are carried out for a well established coarse-grained model in which the polymer is treated as a chain of $N = \sum_\alpha N_\alpha$ beads (where α denotes the species for block copolymers). Monomers of mass $m = 1$ are connected by a spring to form a linear chain. The beads interact with a classical Lennard-Jones (LJ) interaction :

$$\mathrm{U}_{\mathrm{LJ}}^{\alpha\beta}(\mathrm{r}) = \begin{cases} 4\varepsilon_{\alpha\beta}\left[(\sigma_{\alpha\beta}/r)^{12} - (\sigma_{\alpha\beta}/r)^{6}\right] & , r \leq r_c \\ 0 & , r \geq r_c \end{cases} \tag{A.1}$$

where the cutoff distance $r_c = 2.5\sigma_{\alpha\beta}$. α and β represent the chemical species (*e.g*, monomers before polymerization or the solvent s, A phase, B phases,...). In addition to (A.1), adjacent monomers along chains are coupled through the well known anharmonic Finite Extensible Nonlinear Elastic potential (FENE) :

$$\mathrm{U}_{\mathrm{FENE}}(\mathrm{r}) = \begin{cases} -0.5kR_0^2 \ln\left(1 - (r/R_0)^2\right) & , r \leq R_0 \\ \infty & , r > R_0 \end{cases} \tag{A.2}$$

The parameters are identical to those given in Ref. [Kremer 1990], namely $k = 30\varepsilon_{\alpha\beta}/\sigma_{\alpha\beta}^2$ and $R_0 = 1.5\sigma_{\alpha\beta}$, chosen so that unphysical bond crossings and chain breaking are avoided. All quantities will be expressed in terms of length $\sigma_{\alpha\beta} = \sigma$, energy $\varepsilon_{\alpha\beta} = \varepsilon$, pressure ε/σ^3 and time $\tau_{LJ} = \sqrt{m\sigma^2/\varepsilon}$.

Newton's equations of motion are integrated with velocity-Verlet method and a time step $\delta t = 0.006$ [Allen 1987]. Periodic simulation cells of cubic size were used under a Nosé-Hoover barostat,*i.e.* in the NPT ensemble.

Parameters	Signification
N_{monom}	Total number of beads in the simulation box
M	Total number of chains
N_i	Length for a chain i
N	Desired chain length
p	Nucleation probability
N_{growth}	Number of growth steps
n_{bg}	Number of MD steps between two growth steps
N_{eq}	Number of MD steps during equilibration stage
N_α	the number of beads/chain in the phase α (α may be A,B,or C)

TABLE A.1 – Parameters that are used to describe the RLP algorithm.

A.4 Generation of homogenous polymers

The radical-like polymerization process takes place in a solvent which is represented in our simulations as a LJ liquid of $N_{monom} = 50000$ to 600 000 monomers. This liquid has been prepared by melting an initial fcc crystal. The resulting density of the monomer melt is $\rho = N_{monom}\sigma^3/v = 1$, where v is the volume of the simulation box.

As a reminder, a summary of relevant parameters fully describing the radical-like polymerization algorithm is given in table A.4. Figure A.1 shows a schematic presentation of radical like polymerization algorithm which can be divided into five subsequent stages.

1. In the nucleation stage, each monomer has a probability p to be randomly functionalized as a radical. The total number of chains is $M = p * N_{monom}$.
2. In the growth stage, radical index i randomly chooses one of its first nearest monomer neighbours (if any available) to create a new covalent bond (with FENE potential) increasing thus the local chain length N_i of chain i. The amount of growth steps N_{growth}, defined initially, controls the maximum chain length $N_i^{max} = N_{growth}$. This procedure, as mentioned previously, mimics the polydispersity associated with living polymerization. This stage of the process is schematically depicted on figure A.1.b.
3. Relaxation is an essential ingredient of the method. Between two successive growth steps, radicals are allowed to explore their neighborhood during n_{bG} MD steps of the whole system. This is equivalent to let a chain evolve in the solvent and explore a part of its conformational phase space *in situ* while polymerization is taking place, hence permitting a partial relaxation.
4. In the termination stage, for polydisperse systems, the generation procedure is stopped after a fixed number of growth steps N_{growth}. To produce a monodisperse system, the process is stopped only when each chain has reached a desired size N, whatever the number of the growth steps. Naturally, the time

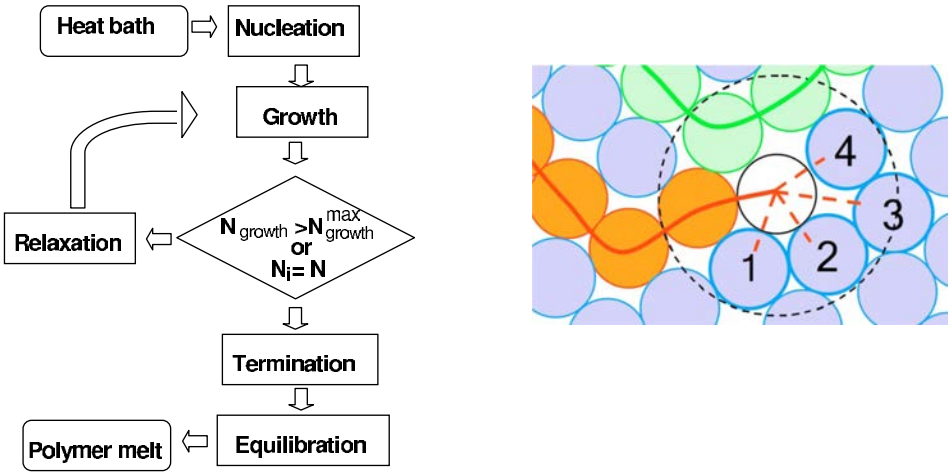

(a) (b)

FIGURE A.1 – (a) Schematic representation of radical like polymerization algorithm. The growth of chains is arrested when each chain reaches its requested length (monodisperse systems) or when the number of growth steps reaches its indicated value (polydisperse systems). (b) Chain growth during radical like polymerization, the radical (active site) selects one monomer from its available nearest neighbours. Since a linear chain system is requested, only chain ends behave as a radical. After the growth step, the new captured monomer becomes a radical

elapsed before termination will depend on the ratio $N \times M/N_{monom}$ (conversion rate). Low conversion rate leads to a poorly entangled system and high conversion rate take a long time to be achieved (the time required for radicals to approach remaining monomers), especially when monodisperse systems are requested. A good compromise was found at a conversion rate near to 80%.

5. Finally, in the equilibration stage, the residual monomers (or solvent) are removed and the system is equilibrated at low compressive pressure to reach the desired density during n_{eq} MD steps.

The previous procedure can be considered as the cornerstone of any generation process by RLP, particularly in the generation of segregated block copolymer samples, where the polymerization takes place under some restrictions as it will be detailed in the next section.

A.5 Generation of triblock lamellar copolymers

The generation of tri-block copolymer samples for coarse grained molecular dynamic simulations is a challenging problem. The complexity of such systems arises from their specific lamellar architecture that imposes several constraints on the chain conformation. Copolymer chains can not be Gaussian as it bridges several segregated phases (three or more) with different properties. The chain motion is then affected by the lamellar ordering and the self diffusion of chains is permitted

within the lamellar planes only. All these restrictions make the generation and the equilibration of coarse grained tri-block copolymer a difficult task. Several molecular dynamic and Monte-Carlo approaches have been developed to model the self assembly mixtures [Santos 2010] and diblock copolymers [Murat 1999]. But the generation of tri-block copolymer is seldom described in the literature, limiting thus the study of such systems by molecular dynamic simulations.

The RLP method has been adjusted to build tri-block copolymer samples. Each sample is composed of four segregated stacks $A-B_1-C-B_2$. A and C blocks will be in a glassy state after equilibration and cooling while B_1 and B_2 blocks will be the rubbery parts of the sample. Therefore, four stacks are then needed to describe a fully periodic sample (periodicity in three dimensions x,y and z).

Depending on the chain architecture, each copolymer chain shares its beads between two or three blocks as explained in the following.

For a chain with length N : $N/4$ beads are in A, $N/2$ beads are in B and the remaining $N/4$ beads are in C (tie molecule), or in A (loop molecule). This division leads to balanced specimens that have the same number of beads in each block.

A.5.1 Generation procedure

The generation of tri-block copolymers ABCB with four interfaces laying in (xy) plane is performed as follows. Starting from a LJ liquid of monomers, the simulation box is equally divided into four distinct regions along the z direction : A, B_1, C and B_2. Each region has a width of $L/4$ (figure A.2,a).

1. Radical beads are chosen randomly in A and C regions (figure A.2,b).
2. Growth is performed until chains reach the size $N/4$. Note that radicals are only allowed to combine with beads that are located in their own region (A or C, see figure A.2,c and A.3, a-b).
3. radicals of chains of length $N/4$ are then attracted to the nearest interface thanks to an additional sinusoidal potential.
4. Growth is then performed in the neighbouring region (B_1 or B_2) until chains reach the size $3N/4$.
5. radicals of chains of length $3N/4$ are then attracted to the appropriate interface thanks to another additional sinusoidal potential : either back to the initial region for loop chains or towards the third domain (C if the polymerization started from A and *vice versa*) for tie chains (see figures A.2, f and A.3, c-d).
6. Chain growth finally occurs until chains reach size N (figure A.2, g).

As for homopolymers, a number of n_{bG} of MD steps is performed after each growth step during which the system is relaxed in NPT ensemble at $k_BT = 2\varepsilon$ and an isotropic pressure $P_{xyz} = 0.5\sigma^3/\varepsilon$. Along the relaxation steps, LJ potential with $\varepsilon = 1$ and $\sigma = 1$ is applied between beads of the same domain and repulsive potential (LJ with $\varepsilon = 0.01$) is applied between beads of neighbouring domains ; avoiding thus mixing of phases.

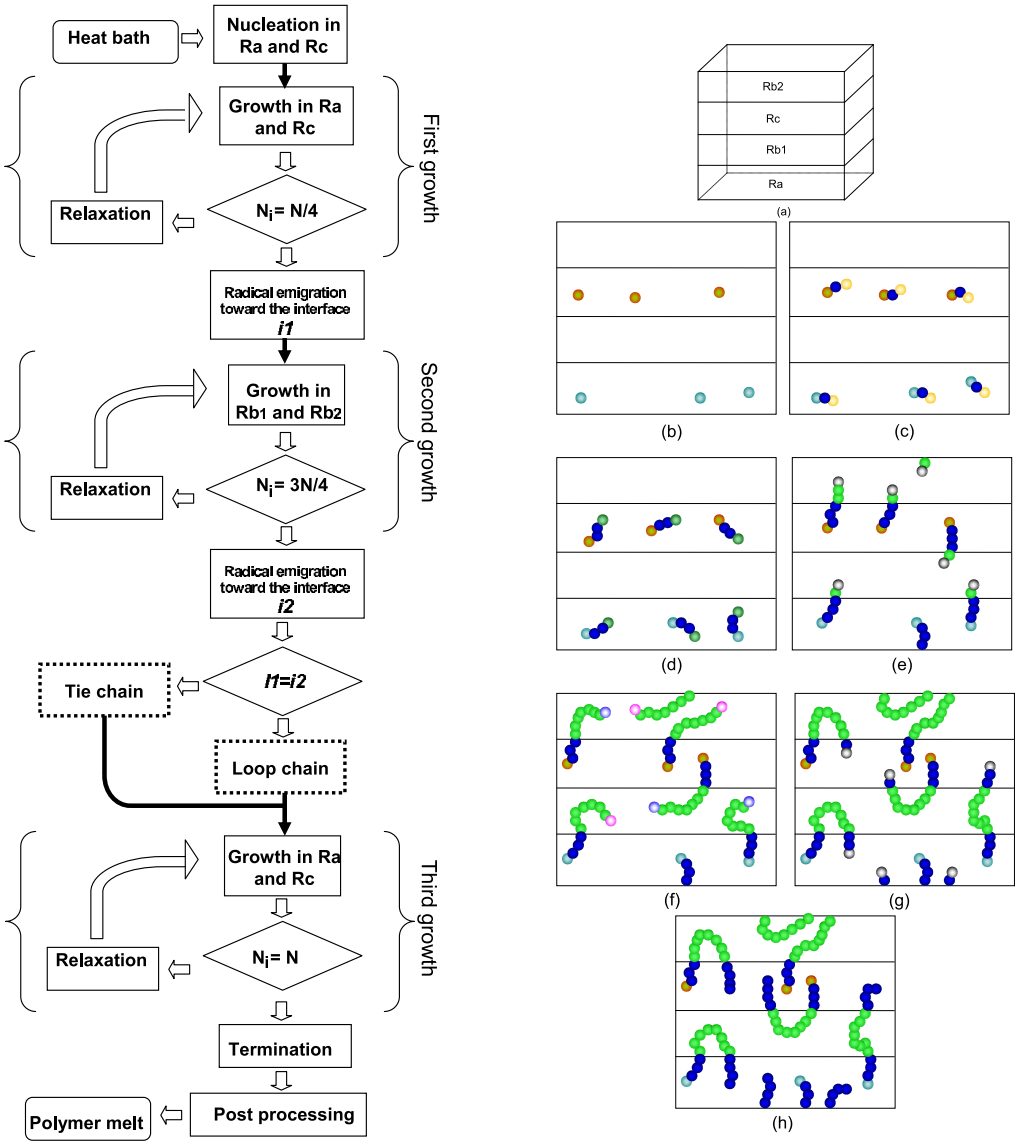

FIGURE A.2 – Left side : RLP algorithm that is used to build a tri-block copolymer sample (see text for more details). Right side : schematic representation showing the evolution of the generation procedure : (a) split the simulation box (b) nucleation stage, (c) growth within A and B, (d) migration of radicals toward nearest interface, (e) growth within B_1 and B_2, (f) migration of radical toward appropriate interface depending on chain type (loop or tie), (g) growth within A and C, (h) termination : the growth is stopped when chains reach requested length. The solvent is not shown in this figure.

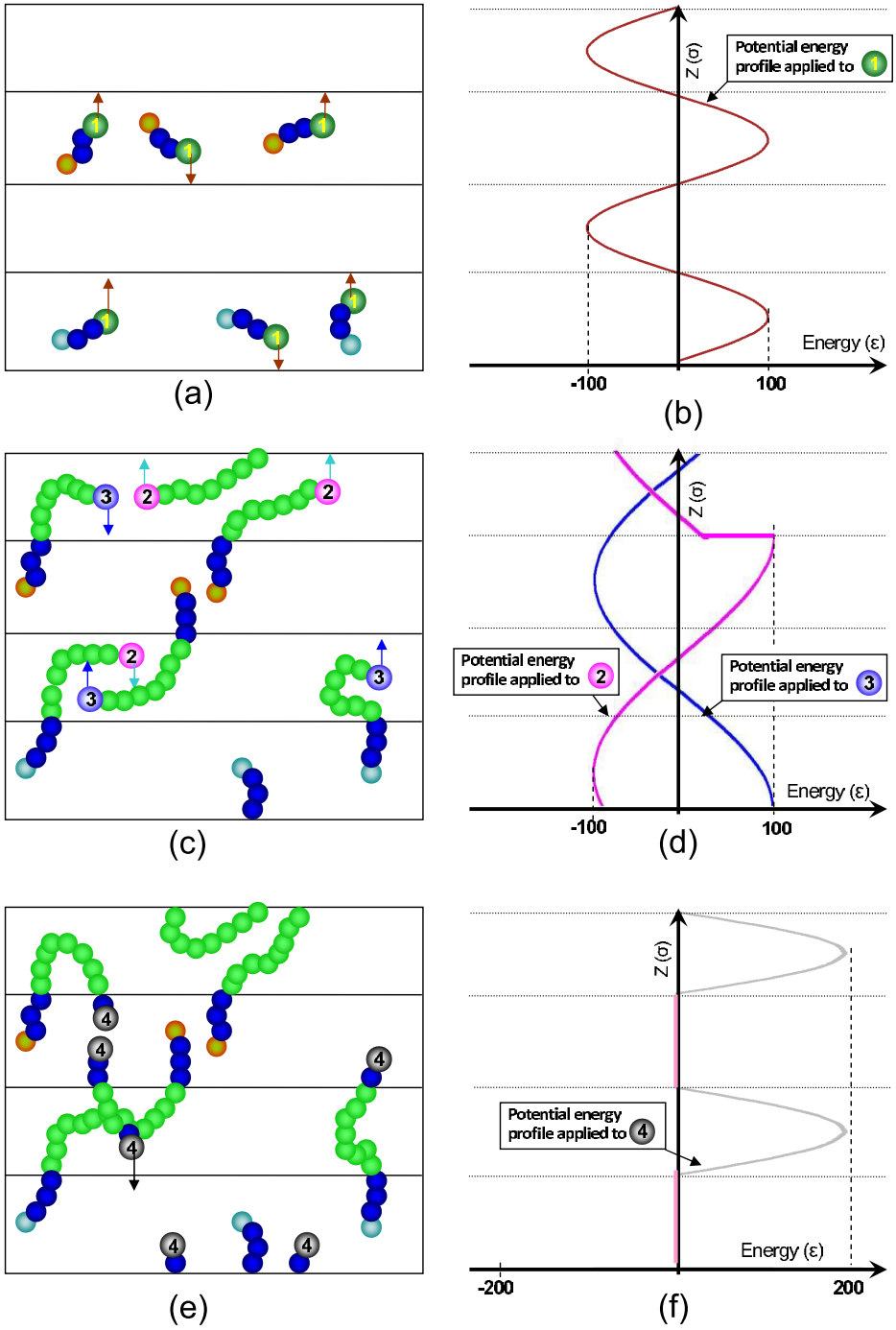

FIGURE A.3 – Potential energy profiles acting on radical beads. The resulting force drives the radical toward its nearest interface : (a) and (b), or the appropriate interface depending on the type of chain (loop or tie) : (c), (d), (e) and (f).

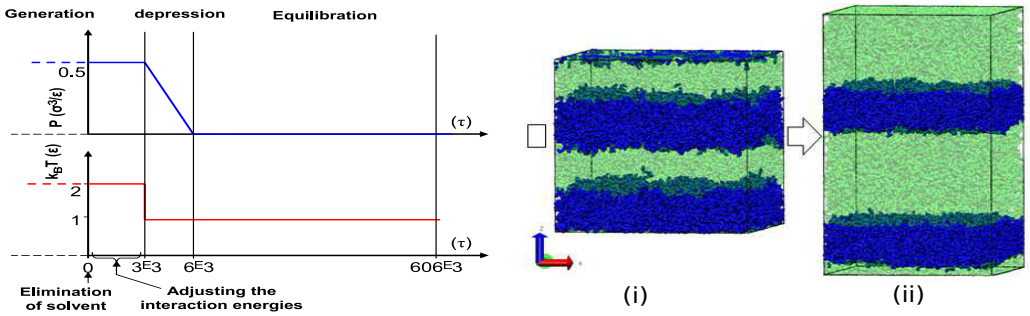

(a) (b)

FIGURE A.4 – (a) post processing steps : evolution of pressure and temperature from the generation to the end of the equilibration.(b) two snapshots of a segregated block copolymer : (i) just after generation, (ii) after equilibration (interaction energies for LJ potentials were $\varepsilon_{AA} = \varepsilon_{CC} = 1$, $\varepsilon_{BB} = 0.5$ and $\varepsilon_{AB} = 0.01$)

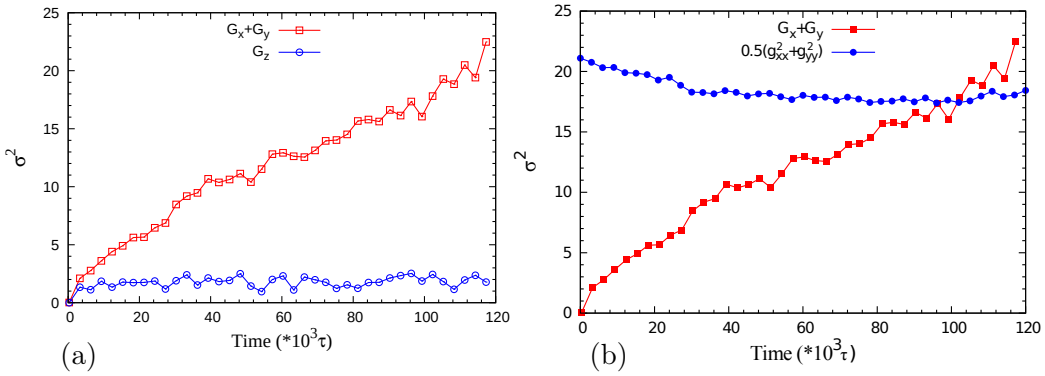

FIGURE A.5 – (a) Comparison between chain diffusion in two directions : parallel (G_z) and perpendicular ($G_x + G_y$) to the lamellar plane . (b) Parallel diffusion compared to the mean square gyration radius taken in x and y directions : the chain diffuses on a lengthscale larger than its own gyration radius.

When the generation is achieved, the sample will be subjected to a sequence of post-processing steps as it will be described in the next section (figure A.2, h).

Figure A.2 summarizes the tri-block generation algorithm as it was coded in the software SOMM [Perez 2006]. Note that this algorithm could be used to generate more complex tri-block systems with different phase morphologies (cylindrical, spherical...).

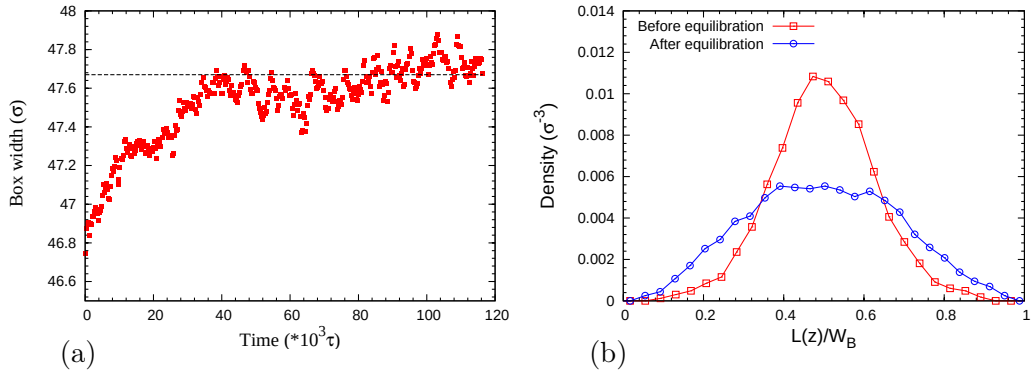

FIGURE A.6 – (a) Evolution of the simulation box width during equilibration stage. The simulation run is long enough as the box width converges to a new equilibrium value. (b) Density profiles of chain ends within the lamellae where the cutting is performed. The distribution becomes more flat after equilibration, and the chain ends are then homogeneously dispersed within the lamellae.

A.5.2 Post processing

After generation, a sequence of post processing stages has been performed in order to obtain an equilibrated tri-block sample :

1. The residual solvent is eliminated.
2. The interaction parameters are gradually adjusted to the desired values under a short run under NPT ensemble, with $k_BT = 1\varepsilon$ and an anisotropic pressure $P_{xx} = P_{yy} = P_{zz} = 0.5\sigma^3/\varepsilon$. Note that the compressive pressure is essential in this stage, in order to remove gaps that are led by the eliminated monomers (solvent).
3. Afterward, the pressure is zeroed progressively in 5×10^5 MD steps ($P_{xx} = P_{yy} = P_{zz} = 0\sigma^3/\varepsilon$)
4. Finally, the system is relaxed 10^7 MD steps in an NPT ensemble at $k_BT = 1\varepsilon$ and $P_{xx} = P_{yy} = P_{zz} = 0\sigma^3/\varepsilon$ with the final values of LJ potentials.

The temperature and pressure are maintained constant by a Nosé Hover thermostat and barostat. Note that, the temperature $k_BT = 1\varepsilon$ is well below the order disorder transition temperature, and above the glass transition temperature of all phases. Therefore, the relaxation stage conserves the segregated state of the rubbery phases. Due to the isotropic applied pressure and to the implemented interaction energies, the simulation box shape adjusts, as shown in figure A.4.

The plot in figure A.6 illustrates the evolution of the simulation box width as equilibration-segregation is in progress. The steady state value of box width denotes the convergence of the lamella thickness to an equilibrium spacing which implies that the segregation is in equilibrium state.

Another criterion is also employed to verify the equilibrium state of copolymer : the sample can be considered as well equilibrated when the diffusion of chains becomes comparable to their mean square gyration radius.

The chain self diffusion $G_{3\alpha}(t)$ is defined as follows :

$$G_{3\alpha}(t) = \langle [r_{cm\alpha}(t) - r_{cm\alpha}(0)]^2 \rangle \tag{A.3}$$

with $\alpha = x$, y or z. Here $r_{cm\alpha}(t)$ are the components of the centre of mass of a chain and $\langle \ldots \rangle$ denotes an ensemble average over all chains. The mean square gyration tensor is :

$$g_{\alpha\beta} = \langle \langle (r_{i\alpha} - r_{cm\beta})^2 \rangle_i \rangle \tag{A.4}$$

$r_{i\alpha}$ are the coordinates of the bead i and $\langle \ldots \rangle_i$ denotes an ensemble average over all beads within a chain. It has been demonstrated in Ref. [Murat 1999, Barrat 1991, Colby 1996] that the self diffusion of chains in lamellar systems can occurs only in lamellar plane (x and y in our case). The free energy penalty of pulling one block thought another prevents the diffusion of chains perpendicularly to the interface.

Figure A.5 a compares the diffusion of chains parallel and perpendicular to lamellar planes. The diffusion in perpendicular direction (G_z) is negligibly small compared to the diffusion in the parallel direction ($G_x + G_y$). The parallel diffusion of chains was also compared to the mean square gyration radius. Figure A.5 b shows that chains diffuse at least one time their own gyration radius in the parallel direction, pouving thus the good equilibration of the polymer sample.

A.5.3 Constructing samples with cilia chains

Additionally to loop and tie chains, a third type of molecular architecture was also implemented in our simulation in order to study the effect of tie molecules on the mechanical properties of nanostructured polymers. This type is called cilia chain hereafter. As a diblock chain, the cilia chain lies between two phases without looping.

Cilia chains were artificially manufactured by cutting randomly a number of tie molecules for a given equilibrated sample without loop chains. Samples with different amounts of cilia chains have been prepared in which tie molecules are cut in their middle. The sample is relaxed 10^7 MD steps in order to well disperse the new created chain ends as it shown in figure A.6 b. Since cilia chains are randomly chosen from tie molecules, the same number of cilia chains crosses each interfaces of the sample. Therefore, the chain ends are homogeneously distributed in the two phases after cutting.

A.6 Conclusion

The RLP is an effective technique to generate and equilibrate polymer and copolymer samples. The efficiency of this method arises from the progressive relaxation

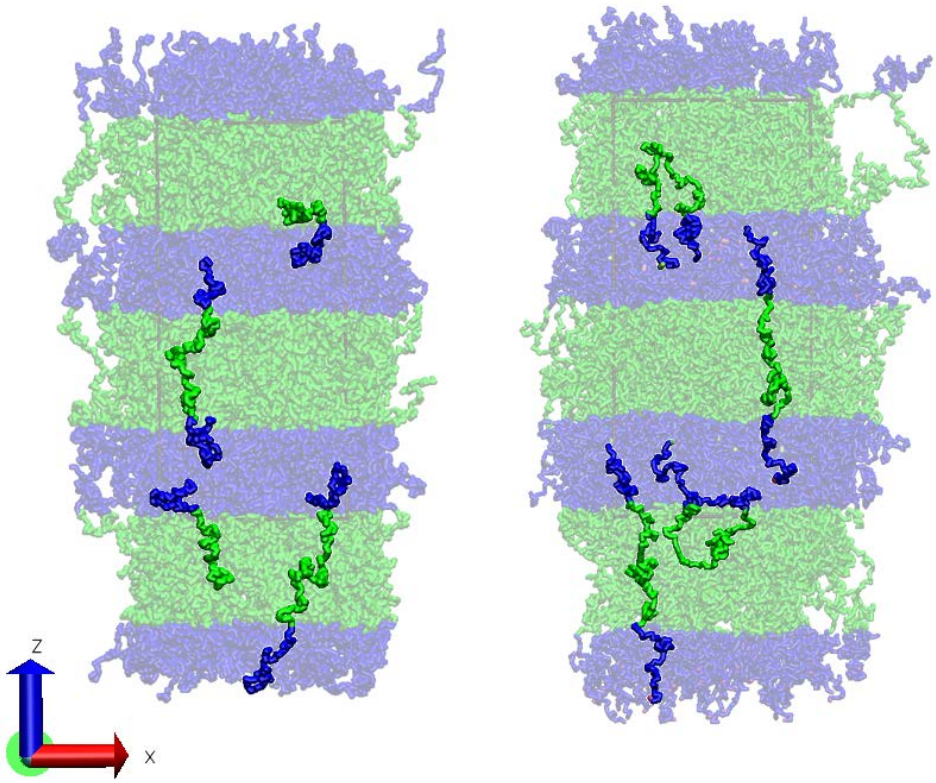

FIGURE A.7 – Two snapshots highlighting the different chain architectures : **Tie, loop, and cilia molecules**. Samples may contain one or two of these types : cilia (loop) and tie as in the left (right) image. A and C phases are coloured in blue B1 and B2 are coloured in green. A and C have the same inter-block and intra-block interaction energies. *idem* for B_1 and B_2. The relevant interactions are $\varepsilon_{AA} = 1$, $\varepsilon_{BB} = 0.2$ and $\varepsilon_{AB} = 0.35$.

of the chain during polymerization. Chains are relaxed before they become too long and too entangled.

The RLP algorithm has been adjusted to generate segregated block copolymers. Samples with two different chain conformations have been generated, loop chains and tie chains. Cilia chains may also be introduced into samples by cutting the tie chains at their middles. Figure A.7 shows two kinds of samples with different chain architectures after the segregation-equilibration procedure.

The stability of lamellar morphology and the lamellar spacing of generated and equilibrated tri-block led to the validation of RLP technique. The advantage of this method resides its ability to control the geometry and architectures of simulated block-copolymers.

Thanks to RLP method a rich database of samples with various chain architectures was built. These samples are used to simulate the mechanical response of nano-structured polymers and copolymers.

Annexe B

Increasing rate of buckling instability

Contents

B.1 The growth rate of the buckling instability

We have shown in the last chapter that the buckling mode depends sensitively on the applied rate of deformation and we have later suggested a linear equation that takes into account this kinetic factor. In this supplementary material we first show how we proceed to solve numerically this equation and we briefly describe and discuss the results.

The formal solution of equation 9 can be written as :

$$U_n(t) = U_n(0).\exp\left(-\Lambda.\int_0^t F(e_{zz}(s),k).ds\right) \tag{B.1}$$

Note that the strain in this case e_{zz} is a time dependent variable $e_{zz}(t) = \dot{e_{zz}} \times t$. The first time derivative of $U_n(t)$ described in equation (9), shows that the solution is not monotonous. The function passes trough a minimum before it rises exponentially. This minimum appears when e_{zz} corresponds to the buckling strain ($e_{zz} = e_{zz}^{buck}$) when $F(e_{zz}(t),k) = 0$. the decreasing part of the curve prior to buckling are irrelevant.

B.2 Solving scheme

Equation (9) has been solved numerically using fourth order Rung-Kutta method starting from an arbitrary small value of $U_n(0)$. We use the classical solving scheme that can be written as follow :

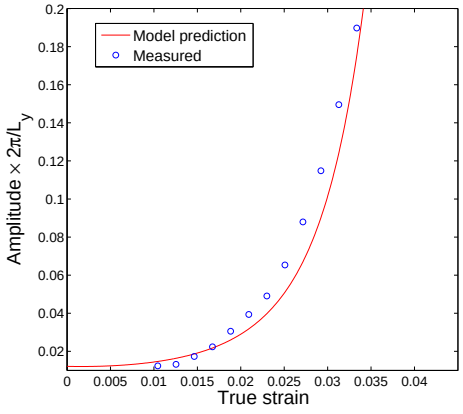

FIGURE B.1 – Comparison between the measured values of buckling amplitude (disconnected symbols) and the value calculated from equation 9 (continues line). The value of Λ taken here corresponds to the best fit of the measured values.

$$U_n(t_i) = U_n(t_{i-1}) + (h_1 + 2h_2 + 2h_3 + h_4) \times \delta t/6 \tag{B.2}$$

where δt is a time step ($\delta t = t_i - t_{i-1}$) chosen enough small to ensure the convergence of the solving scheme. h_1, h_2, h_3 and h_4 are the intermediate solving steps that can be written as follows :

$$\begin{aligned}
h_1 &= -\Lambda.F(e_{zz}(t_{i-1}), k) \times U_n(t_{i-1}) \\
h_2 &= -\Lambda.F(e_{zz}(t_{i-1} + \tfrac{\delta t}{2}), k) \times (U_n(t_{i-1}) + h_1 \tfrac{\delta t}{2}) \\
h_3 &= -\Lambda.F(e_{zz}(t_{i-1} + \tfrac{\delta t}{2}), k) \times (U_n(t_{i-1}) + h_2 \tfrac{\delta t}{2}) \\
h_4 &= -\Lambda.F(e_{zz}(t_{i-1} + \delta t, k) \times (U_n(t_{i-1}) + h_3 \delta t)
\end{aligned} \tag{B.3}$$

The value of Λ was determined by the solution that ensures the best fit of the bucking amplitude values measured during the deformation of the largest sample at low strain rate (see figure B.1). We find that Λ is equal to 370 for an initial value of 0.03. In the rest of this section we admit that lambda is independent from the strain rate, this assumption will be discussed later.

B.3 Results

Having fixed Λ, equation 9 has been solved for different values of wave vectors $2\pi/L_y$, $4\pi/L_y$ and $6\pi/L_y$ at the same strain rate. The results were plotted and compared in figure 2 (left panel). This figure shows, firstly, that the buckling strain increases as the buckling wave vector increases, as expected. Secondly, the higher

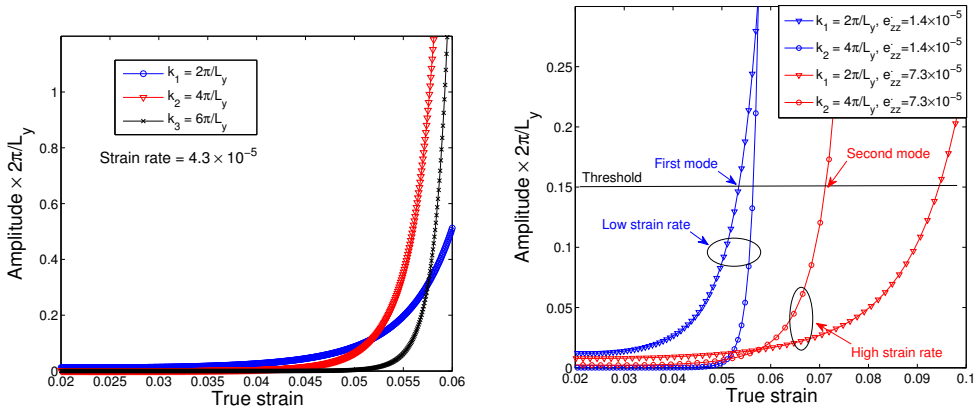

FIGURE B.2 – Left panel : Comparison between the buckling growth of the first three modes : the higher mode develops faster than the lower mode even if the instability of the latter is triggered at first. Right panel : comparison between the fundamental and the second buckling mode for the largest tested sample at two different strain rates. The threshold is chosen so that it cross simultaneously the fundamental mode growth at first at low strain rate and the second mode growth at first at high strain rate.

buckling modes are faster to develop compared to the lower wavevector buckling mode.

To illustrate the influence of the strain rate on the on the growth rate of the buckling instability, the right panel of figure 2 compares the amplitude growth of the first and second buckling modes of the largest sample at two different strain rates. As shown in the figure the second mode growth intercepts the fundamental buckling growth at a certain strain (called below switching strain, e_{sw}) for both strain rates. At this strain the second buckling mode can overwhelmed the fundamental mode if this later is not yet developed. for low strain rate case the fundamental buckling mode was basically triggered a low strain, the first mode of buckling still develops until the strain reaches e_{sw}. At this end the buckling amplitude is well developed and the sample can not switch to higher buckling mode, therefore the fundamental mode is selected. In contrast, at high strain rate when the sample reaches e_{sw} the first mode was *theoretically* triggered but it is barely developed so that the second mode can easily overwhelm the fundamental mode and the sample adopts a higher mode for buckling.

From the previous analysis one can define a critical buckling amplitude as the amplitude threshold after which the selection of the buckling mode is achieved. This mean that the buckling mode that reaches this threshold at the first is the one that is adopted by the sample to achieve the buckling. This mode is called hereafter the "winner mode". Quantitatively speaking the "winner mode" of buckling is defined when the strain elapsed to reach the critical amplitude is minimum.

The critical amplitude threshold can be determined approximatively from figure

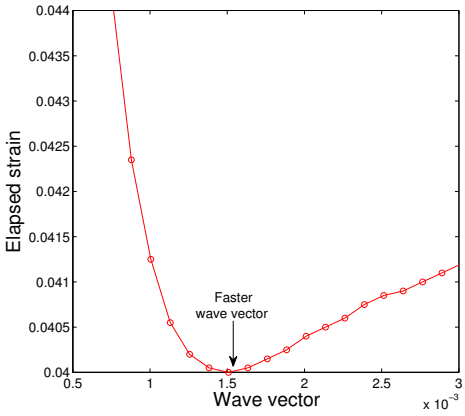

FIGURE B.3 – True strain elapsed from the beginning of the deformation to reach the threshold for different buckling wave vectors (buckling modes) the minimum corresponds to the "winner mode" : the mode selected by the sample to achieve the buckling ($\dot{e_{zz}} = 10^{-7},\ L_y = 10000\sigma$).

2 (right panel). This threshold graphically located in the amplitude interval delimited by the two switch points [1] for each strain rate curve. For the rest of analysis the amplitude threshold was chosen in the middle of the specified interval ($U^* = 0.15$) at this value the threshold crosses the fundamental mode growth at first at low deformation rate while it crosses the second mode at first at high deformation rate.

B.4 generalization

In order to generalize the previous analysis : let us consider an extremely large sample that is deformed at a chosen strain rate $\dot{e_{zz}}$: The choice of a large sample size leads to close values of wave vectors $2\pi/L_y \simeq 4\pi/L_y \simeq 6\pi/L_y...$. To identify the "winner mode", the growth of amplitude for each buckling mode was analyzed. The parameter Λ and the amplitude threshold U^* values are chosen as above. The strain elapsed for each buckling mode growth to reach the amplitude threshold U^* was measured. The result is plotted in figure 3. This figure shows the elapsed strain with respect the buckling wave vector. the curve passes trough a minimum that separates two regimes : the decreasing portion of the curve that corresponds effectively to the fact that the development of buckling becomes faster and faster as the buckling wave vector increases. therefore the elapsed strain decreases. the second regime where the curve rises after the minimum. This regime corresponds to the increase of buckling strain observed when the buckling wave vector increases. The minimum between the two regimes corresponds to the"winner mode".

1. This term designates the switching from the fundamental to the second mode only

B.5 summery

In this paper, we have shown that the strain rate is crucial in the determination of the buckling mode of triblock copolymer systems. In order to predict the selection of the buckling mode, a new model has been developed. The analysis steps of can be summarized as follows :

1. Determination of the parameter Λ from the fit of measured buckling amplitude by the solution of equation (9) (trial and error process)
2. Identification of the amplitude threshold that justifies the "winner mode" of buckling in the experimental results.
3. For any strain rate, the "winner mode" is the mode in which the strain elapsed to reach the amplitude threshold is minimum.

This last step allows one a *theoretical* prediction of buckling mode that must be adopted by the sample depending on the applied strain rate ; however, this prediction doesn't take into account the nucleation of cavities observed at extremely hight strain rate or in small sample size, or the possible variations of Λ with deformation rate.

Bibliographie

[Adhikari 2004] R. Adhikari and G. Michler. *Influence of molecular architecture on morphology and micromechanical behavior of styrene/butadiene block copolymer systems.* Progress in Polymer Science, vol. 29, pages 949–986, 2004. 81

[Allen 1987] M.P. Allen and D.J. Tildesley. *Computer Simulation of Liquid.* Oxford sci. pub., 1987. 9, 124

[Argon 1977] A. Argon and J. Hannoosh. *Initiation of crazes in polystyrene.* Phil. Mag., vol. 36, page 1195, 1977. 33

[Auhl 2003] R. Auhl, R. Everaers, G. Grest, K. Kremer and S. Plimpton. *Equilibration of long chain polymer melts in computer simulations.* The Journal of Chemical Physics, vol. 119, pages 12718–12728, 2003. 9, 36, 123

[Barrat 1991] J. L. Barrat and G. H. Fredrickson. *Diffusion of a symmetric block copolymer in a periodic potential.* Macromlecules, vol. 24, page 6378, 1991. 132

[Bartczak 2005] Z. Bartczak. *Effect of Chain Entanglements on Plastic Deformation Behavior of Linear Polyethylene.* Macromolecules, vol. 38, pages 7702–7713, 2005. 56

[Bates 1999] F. Bates and G. Fredrickson. *Block Copolymers-Designer Soft Materials.* Phys. Today, vol. 52, page 32, 1999. 52, 53

[Becquart 2010] C. Becquart and M. Perez. *Dynamique moléculaire appliquée aux matériaux.* Technique de l'ingenieure, pages RE 136–1, 2010. 2, 4

[Biot 1961] M. Biot. *Theory of folding of stratified viscoelastic media and its implication in tectonics and orogenesis.* Geological Society of America Bulletin, vol. 72, pages 1595–1620, 1961. 94

[Bowden 1973] P. Bowden and R. Oxborough. *A general critical-strain criterion for crazing in amorphous glassy polymers.* Phil. Mag., vol. 28, page 547, 1973. 34

[Brown 1991] D. Brown and J. Clarke. *Molecular dynamics simulation of an amorphous polymer under tension. 1. Phenomenology.* Macromolecules, vol. 24, page 2075, 1991. 11

[Capaldi 2002] F. Capaldi, M. Broyce and G. Rutledge. *Enhanced Mobility Accompanies the Active Deformation of a Glassy Amorphous Polymer.* Phys. rev. let., vol. 89, page 175505, 2002. 10, 11

[Capaldi 2004] F. Capaldi, M. Broyce and G. Rutledge. *Molecular response of a glassy polymer to active deformation.* Polymer, vol. 45, page 1391, 2004. 11

[Cohen 2000] Y. Cohen, R. Albalak and B. Dair. *Deformation of Oriented Lamellar Block Copolymer Films.* Macromolecules, vol. 33, page 6502, 2000. 55, 81, 83

[Cohen 2001] Y. Cohen. *Deformation of Oriented Lamellar Block Copolymer Films.* Macromolecules, vol. 33, pages 6502–6516, 2001. 81, 85

[Cohen 2003] Y. Cohen and E. Thomas. *Effect of Defects on the Response of Layered Block Copolymer to Perpendicular deformation : One Dimensional Necking.* Macromoleculs, vol. 36, pages 5265–5270, 2003. 83

[Colby 1996] R. Colby. *Block copolymer dynamics.* Colloid Interface Sci., vol. 1, page 454, 1996. 132

[David 2002] L. David and S. Etienne. *Introduction A La Physique Des Polyméres.* Dunod editions, 2002. 56

[de Gennes 1993] P. G. de Gennes and J. Prost. *The physics of liquid crystals.* Clarendon - Oxford, 1993. 81

[Detcheverry 2008] F. Detcheverry, H. Kang, K. Daoulas, M. Muller, P. Nealey and J. de Pablo. *Monte Carlo Simulations of a Coarse Grain Model for Block Copolymers and Nanocomposites.* Macromolecules, vol. 41, pages 4989–5001, 2008. 52

[Detcheverry 2010] F. Detcheverry, D. Pike, P. Nealey, M. Muller and JJ. de Pablo. *Simulations of theoretically informed coarse grain models of polymeric systems.* Faraday Discussions, vol. 144, pages 111–125, 2010. 42

[Doi 1986] M. Doi and S. Edward. *The Theory of polymer dynamics.* Clarendon Press, Oxford, 2, 1986. 23

[Doi 1995] M. Doi. *Introduction to polymer physics.* Press :Oxford science publications, 1995. 53

[Estevez 2000] R. Estevez, M. Tijssens. and E. Van der Giessen. *Micromechanical modelling of rate and temperature dependent fracture of glassy polymers.* J. Mech. Phys. Sol., vol. 48, pages 2585–2617, 2000. 33

[Flory 1953] P. Flory. *Principles of Polymer Chemistry.* Cornell University Press : Ithaca NY, 1953. 53

[Foteinopoulou 2006] K. Foteinopoulou, N. Ch. Karayiannis, V. G. Mavrantzas and M. Kroger. *Primitive Path Identification and Entanglement Statistics in Polymer Melts : Results from Direct Topological Analysis on Atomistic Polyethylene Models.* Macromolecules, vol. 39, pages 4207–4216, 2006. 28

[Gao 1995] J. Gao. *An efficient method of generating dense polymer model melts by computer simulation.* The Journal of Chemical Physics, vol. 102, pages 1074–1077, 1995. 9

[Gent 1970] A. Gent. *Hypothetical mechanism of crazing in glassy plastics.* J. Mater. Sci., vol. 5, pages 925–932, 1970. 34

[Goldhirsch 2002] I. Goldhirsch and C. Goldenberg. *On the microscopic foundations of elasticity.* Eur. Phys. J. E, vol. 9, pages 245–251, 2002. 42

[Gonzalez 2006] R. Gonzalez. *Etude du comportement sous deformation de copolymers blocs SBS et SBM morphologie lamellaire.* Phd thesis, National institute of applied sciences- INSA LYON-France, 2006. 65

[Grest 1996] G. Grest, M. Lacasse, K. Kremer and A. Gupta. *Efficient continuum model for simulating polymer blends and copolymers.* J. Chem. Phys., vol. 105, page 10583, 1996. 53

[G'Sell 1994] C. G'Sell and A. Dahoun. *Evolution of microstructure in semi-crystalline polymers under large plastic deformation.* Materials Science and Engineering, vol. A175, pages 183–199, 1994. 55

[Guo 2006] H. Guo. *Shear induced parallel to perpendicular orientation transition in amphiphilic lamellar phase : A non equilibrium molecular-dynamics simulation study.* J. Chem. Phys., vol. 124, page 054902, 2006. 85

[Hamley 1998] I. Hamley. *The Physics of Block Copolymers.* Oxford University Press : Oxford, 1998. 52

[Haward 1993] R. Haward. *Strain Hardening of Thermoplastics.* Macromolecules, vol. 26, pages 5860–5869, 1993. 56

[Hermel 2003] T. Hermel, S. Hahn, K. Chaffin, W. Gerberich and F. Bates. *Role of Molecular Architecture in Mechanical Failure of Glassy Semicrystalline Block Copolymers : CEC vs CECEC Lamellae.* Macromolecules, vol. 36, pages 2190–2193, 2003. 70, 82, 83, 84

[Herrmann 2002] K. P. Herrmann and V. G. Oshmyan. *Theoretical study of formation of pores in elastic solids : particulate composites, rubber toughened polymers, crazing.* International Journal of Solids and Structures, vol. 39, pages 3079–3104, 2002. 33

[Hoover 1984] W. Hoover. *Canonical dynamics : Equilibrium phase-space distributions.* Phys. Rev. A, vol. 31, page 1695, 1984. 10

[Hoy 2005] R. S. Hoy and M. O. Robbins. *Effect of equilibration on primitive path analyses of entangled polymers.* Phys. Rev. E, vol. 72, page 061802, 2005. 24, 26, 27

[Hoy 2006] R.S. Hoy and M.O. Robbins. *Strain hardening of polymer glasses : Effect of entanglement density, temperature, and rate.* J. Polymer Science B, vol. 44, page 3487, 2006. 7, 10, 16, 23, 28

[Hoy 2007] R. S. Hoy and M. O. Robbins. *Strain Hardening in Polymer Glasses : Limitations of Network Models.* Phys. Rev. Lett., vol. 99, page 117801, 2007. 30

[Hoy 2008] R. S. Hoy and M. O. Robbins. *Strain hardening of polymer glasses : Entanglements, energetics, and plasticity.* Phys. Rev. E, vol. 77, page 031801, 2008. 16, 28, 30

[Humbert 2009] S. Humbert, O. Lame and G. Vigier. *Influence de la topologie moléculaire et de la microstructure sur les propriétés mécaniques des Polyéthylènes.* Ph.D. Thesis - INSA de Lyon, 2009. 55, 57, 67

[Humbert 2010] S. Humbert, O. Lame, JM. Chenal, C. Rochas and G. Vigier. *New Insight on Initiation of Cavitation in Semicrystalline Polymers : In-Situ*

SAXS Measurements. Macromolecules, vol. 43, pages 7212–7221, 2010. 33, 56

[Izrailev 1998] S. Izrailev, S. Stepaniants, B. Isralewitz, D. Kosztin, H. Lu, F. Molnar, W. Wriggers and K. Schulten. *Computational Molecular Dynamics : Challenges and Methods and Ideas.* Lecture Notes in Computational Science and Engineering, vol. 4, page ., 1998. 12

[Khaliullin 2008] R. Khaliullin and J. Schieber. *Analytic Expressions for the Statistics of the Primitive-Path Length in Entangled Polymers.* Phys. Rev. Lett., vol. 100, page 188302, 2008. 23

[Kremer 1990] K. Kremer and G. Grest. *Dynamics of entangled linear polymer melts : A molecular-dynamics simulation.* The Journal of Chemical Physics, vol. 92, pages 5057–5086, 1990. 8, 9, 35, 124

[Kremer 2005] K. Kremer, S. Sukumaran, R. Everaers and G. Grest. *Entangled polymer systems.* Computer Physics Communications, vol. 169, pages 75 – 81, 2005. Proceedings of the Europhysics Conference on Computational Physics 2004. 23

[Kroger 1997] M. Kroger, C. Luap and R. Muller. *Polymer Melts under Uniaxial Elongational Flow : Stress-Optical Behavior from Experiments and Nonequilibrium Molecular Dynamics Computer Simulations.* Macromolecules, vol. 30, page 526, 1997. 18

[Kroger 2005] M. Kroger. *Shortest multiple disconnected path for the analysis of entanglements in two- and three-dimensional polymeric systems.* Computer Physics Communications, vol. 168, pages 209–232, 2005. 23

[Larson 1994] R. Larson. *Simulation of lamellar phase transition in block copolymers.* Macromolecules, vol. 27, pages 4198–4203, 1994. 52

[Léonforte 2010] F. Léonforte. *Evolution of entanglements during the response to a uniaxial deformation of lamellar triblock copolymers and polymer glasses.* Phys. Rev. E, vol. 82, page 041802, 2010. 72

[Lim 2005] L. S. Lim. Ph.d thesis, University of Mannesota, Minneapolis, MN, 2005. 85

[Lyulin 2004] A. Lyulin, N. Balabaev, M. Mazo and M. Michels. *Molecular Dynamics Simulation of Uniaxial Deformation of Glassy Amorphous Atactic Polystyrene.* Macromolecules, vol. 37, page 8785, 2004. 7

[Lyulin 2005] A. Lyulin, B. Vorselaares, M. Mazo and M. Michels. *Strain softening and hardening of amorphous polymers : Atomistic simulation of bulk mechanics and local dynamics.* Europhys. Lett, vol. 71, page 618, 2005. 16

[MacNeill 2010] D. MacNeill and J. Rottler. *From macroscopic yield criteria to atomic stresses in polymer glasses.* Phys. Rev. E, vol. 81, page 011804, 2010. 40, 41, 42

[Mahajan 2010] D. Mahajan, B. Singh, and S. Basu. *Void nucleation and disentanglement in glassy amorphous polymers.* Phys. Rev. E, vol. 82, page 011803, 2010. 34

[Mahanthappa 2008] M. Mahanthappa, M. Hillmyer and F. Bates. *Mechanical Consequences of Molecular Composition on Failure in Polyolefin Composites Containing Glassy, Elastomeric, and Semicrystalline Components.* Macromolecules, vol. 41, pages 1341–1351, 2008. 83

[Makke 2009] A. Makke, M. Perez, O. Lame and J.L. Barrat. *Mechanical testing of glassy and rubbery polymers in numerical simulations : Role of boundary conditions in tensile stress experiments.* J. Chem. Phys., vol. 131, pages –, 2009. 7, 28, 36

[Monasse 2008] B. Monasse, S. Queyroy and O. Lhost. *Molecular Dynamics prediction of elastic and plastic deformation of semi-crystalline polyethylene.* Int. J. Mater Form-Springer/ESAFORM, pages 949–986, 2008. 56, 57, 68

[Mori 2003] Y. Mori, L. Lim and F. Bates. *Consequences of Molecular Bridging in Lamellae-Forming Triblock/ Pentablock Copolymer Blends.* Macromolecules, vol. 36, pages 9879–9888, 2003. 54, 55, 71, 83, 84, 85

[Mukerji 2009] D. Mukerji and C.F. Abrams. *Mechanical behavior of highly cross-linked polymer networks and its links to microscopic structure.* phys. rev. E, vol. 79, page 061802, 2009. 123

[Murat 1999] M. Murat, G. S. Grest and K. Kremer. *Statics and Dynamics of Symmetric Diblock Copolymers : A Molecular Dynamics Study.* Macromolecules, vol. 32, pages 595–609, 1999. 127, 132

[Nose 1984] S. Nose. *A unified formulation of the constant temperature molecular dynamics methods.* The Journal of Chemical Physics, vol. 81, pages 511–519, 1984. 10

[Papakonstantopoulos 2007] GJ. Papakonstantopoulos, M Doxastakis, P. Nealey, J. de Pablo and JL Barrat. *Calculation of local mechanical properties of filled polymers.* Phys. Rev. E, vol. 75, page 031803, 2007. 7

[Papakonstantopoulos 2008] G. Papakonstantopoulos, R. Riggleman, JL Barrat and JJ. de Pablo. *Molecular plasticity of polymeric glasses in the elastic regime.* Phys. Rev E, vol. 77, page 041502, 2008. 7, 16, 34, 42, 44

[Perez 1998] J. Perez. *Physics and mechanics of amorphous polymers.* Balkema, Rotterdam, 1998. 33, 39

[Perez 2006] M. Perez, F. Leonforte and A. Makke. *Open Software for Molecular Modeling.* first edition 2006. 130

[Perez 2008] M. Perez, O. Lame, F. Leonforte and J.L. Barrat. *Polymer chain generation for coarse-grained models using radical-like polymerization.* The Journal of Chemical Physics, vol. 128, page 234904, 2008. 9, 35, 73, 124

[Phatak 2006] A. Phatak, L. Lim, C. Reaves and F. Bates. *Toughness of Glassy-Semicrystalline Multiblock Copolymers.* Macromolecules, vol. 39, pages 6221–6228, 2006. 55, 83, 85

[Rakshit 2006] A. Rakshit and R. C. Picu. *Coarse grained model of entangled polymer melts.* The Journal of Chemical Physics, vol. 125, page 164907, 2006. 8

[Ramberg 1964] H. Ramberg. *Selective buckling of composite layers with contrasted rheological properties.* Tectonophysics, vol. 1, pages 307–341, 1964. 94

[Ramsay 1987] J. Ramsay and M. Huber. *The Technique of Modern Structural Geology.* Academic-London, 1987. 81

[Read 1999] D. J. Read, R. Duckett, J. Sweeny and T. McLeish. *The chevron folding instability in thermoplastic elastomers and other layered material.* J. Phys. D : Appl. phys., pages 2087–2099, 1999. 55, 80, 81, 94, 98

[Riggleman 2009] R. Riggleman, G. Toepperwein, G.J. Papakonstantopoulos, JL Barrat and JJ. de Pablo. *Entanglement network in nanoparticle reinforced polymers.* J. Chem. Phys., vol. 130, pages –, 2009. 23

[Rottler 2001] J. Rottler and M. O. Robbins. *Yield conditions for deformation of amorphous polymer glasses.* Phys. Rev. E, vol. 64, page 051801, 2001. 18, 20, 34, 36

[Rottler 2003] J. Rottler and M. O. Robbins. *Growth, microstructure, and failure of crazes in glassy polymers.* Phys. Rev. E, vol. 68, no. 1, page 011801, Jul 2003. 7, 10, 16, 28

[Rottler 2009] J. Rottler. *Fracture in glassy polymers : a molecular modeling perspective.* J. Phys. : Condens. Matter, vol. 21, page 463101, 2009. 29

[Rycroft 2006] C. Rycroft, G. Grest, J. Landry and M. Bazant. *Analysis of granular flow in a pebble-bed nuclear reactor.* Phys. Rev. E, vol. 74, page 021306, 2006. 38

[Santos 2010] A. Santos, C. Singh and S. C. Glotzer. *Coarse-grained models of tethers for fast self-assembly simulations.* Phys. Rev. E, vol. 81, 2010. 127

[Schnell 2006] B. Schnell, J. Baschnagel and H.Meyer. *Etude par simulation numérique de la transition vitreuse et de l'état vitreux de polymères denses amorphes propriétés mécaniques et phénomne de cavitation.* PhD. thesis Université de Strasbourg, vol. -, pages –, 2006. 4, 7, 10, 16, 18, 27, 28, 36, 58

[Schrauwen 2004] B. Schrauwen, R. Janssen, L. Govaert and H. Meijer. *Intrinsic Deformation Behavior of Semicrystalline Polymers.* Macromolecules, vol. 37, pages 6069–6078, 2004. 56

[Semenov 1986] A. Semenov. *Theory of diblock-copolymer segregation to the interface and free surface of a homopolymer layer.* Macromolecules, vol. 25, page 4967, 1986. 52

[Seul 1992] M. Seul and R. Wolfe. *Evolution of disorder in two-dimensional stripe patterns : "Smectic" instabilities and disclination unbinding.* Phys. Rev. Lett., vol. 68, page 2460, 1992. 81

[Sides 2004] S. W. Sides, G. S. Grest, M. J. Stevens and S. J. Plimpton. *Effect of End-Tethered Polymers on Surface Adhesion of Glassy Polymers.* J. Polym. Sci. part B : Polym. Phys., vol. 42, 2004. 56, 57

[Sixou 2007] B. Sixou. *Molecular dynamics simulation of the first stages of the cavitation process in amorphous polymers.* Molecular simulation, vol. 33, pages 965–973, 2007. 18, 34

[Sollich 2009] P. Sollich, A. Barra, M. E. Cates, S. M. Fielding, P. Hebraud and F. Lequeux. *Soft glasses, rheology, and trap models.* http ://www.icts.res.in/uploads/document/1267765081Peter-Sollich-Jan11.pdf, page ., 2009. 44

[Stachurski 2003] Z. Stachurski. *Strength and deformation of rigid polymers : the stress-strain curve in amorphous PMMA.* Polymer, vol. 44, pages 6067–6076, 2003. 38

[Sternstein 1969] S. Sternstein and L. Ongchin. *Yield criteria for plastic deformation of glassy high polymers in general stress fields.* Polym. Prepr., vol. 10, page 1117, 1969. 34

[Sukumaran 2005] S. Sukumaran, G. Grest, K. Kremer and R. Everaers. *Identifying the primitive path mesh in entangled polymer liquids.* Journal of Polymer Science,Part B : Polymer Physics, vol. 43, page 917933, 2005. 23, 24, 27

[Thomas 2001] E. Thomas, Y. Cohen and M. Brinkmann. *Undulation, dilatation, and folding of layered block copolymer.* Macromolecules, vol. 114, pages 984–992, 2001. 81, 83

[Toepperwein 2011] G. N. Toepperwein and J. J. de Pablo. *Cavitation and crazing in rod-containing nanocomposites.* Macromolecules, vol. 44, pages 5498–5509, 2011. 48

[Tsamados 2008] M. Tsamados, A. Tanguy, F. Leonforte and J.-L. Barrat. *On the study of local-stress rearrangements during quasi-static plastic shear of a model glass : Do local-stress components contain enough information ?* Eur. Phys. J. E, vol. 26, pages 283–293, 2008. 41

[Tsamados 2009] M. Tsamados, A. Tanguy, C. Goldenberg and J.L. Barrat. *Local elasticity map and plasticity in a model Lennard-Jones glass.* Phys. Rev. E, vol. 80, page 026112, 2009. 34, 42, 44

[Tsamados 2010] M. Tsamados. *Plasticity and dynamical heterogeneity in driven glassy materials.* Eur. Phys. J. E, vol. 32, pages 165–181, 2010. 36

[Turnbull 1961] D. Turnbull and M. Cohen. *Free Volume Model of the Amorphous Phase : Glass Transition.* J. Chem. Phys., vol. 34, page 120, 1961. 38

[Turnbull 1970] D. Turnbull and M. Cohen. *On the Free Volume Model of the Liquid Glass Transition.* J. Chem. Phys., vol. 52, page 3038, 1970. 38

[Tzoumanekas 2006] C. Tzoumanekas and D. N. Theodorou. *Topological Analysis of Linear Polymer Melts : A Statistical Approach.* Macromolecules, vol. 39, pages 4592–4604, 2006. 23

[Vorselaars 2009] B. Vorselaars, Lyulin A V and Michels M A. *Microscopic Mechanisms of Strain Hardening in Glassy Polymers.* Macromolecules, vol. 42, page 5829, 2009. 30

[Weynant 1980] E. Weynant, J.M. Haudin and C. G'Sell. *In situ observation of the spherulite deformation in polybutene- 1.* J. Mater. Sci., vol. 15, pages 2677–2692., 1980. 55

[Wittmer 2002] J. Wittmer, A. Tanguy, JL. Barrat and L. Lewis. *Vibrations of amorphous, nanometric structures : When does continuum theory apply ?* Europhys. lett., vol. 57, pages 423–429, 2002. 42

[Wu 2004] L. Wu, T. Lodge and F. Bates. *Bridge to Loop Transition in a Shear Aligned Lamellae Forming Heptablock Copolymer.* Macromolecules, vol. 37, pages 8184–8187, 2004. 70, 83, 85

[Yoshimoto 2004] K. Yoshimoto, T.S. Jain, K. Van Korkum, P.F. Nealey and J.J. de Pablo. *Mechanical Heterogeneities in Model Polymer Glasses at Small Length Scales.* Phys. Rev. Lett., vol. 93, page 175501, 2004. 7, 16, 34, 44

[Yoshimoto 2005] P.F. Lutesko Yoshimoto G.J. Papakonstantopoulos and J.J. de Pablo. *Statistical calculation of elastic moduli for atomistic models.* Phys. Rev. B, vol. 71, no. 18, page 184108, May 2005. 34

SUMMARY

We use molecular dynamics simulation of a coarse grained model to investigate the mechanical properties of homogenous polymers and lamellar block copolymers. Polymer samples have been generated using "radical like polymerisation" method. These samples were submitted to uniaxial and triaxial tensile tests in order to study their mechanical responses.

First we compare two tensile test methods: the "homogenous deformation method" and the "boundary driven deformation method". We find that the two methods lead to similar results at low strain rate.

The change of the entanglement network in polymer sample undergoing a tensile deformation was investigated. We have found that the sample exhibits an increase of its entanglement length in uniaxial deformation test compared to triaxial deformation one.
Our finding was interpreted by the pronounced chain disentanglement observed in the uniaxial deformation test due to the lateral relaxation of the sample.

The cavity nucleation in amorphous polymers has been also studied. We have found that the cavities nucleate preferentially in zones that exhibit a low elastic bulk modulus. These zones can be identified from the initial undeformed state of the sample at low temperature (T~0K).

The second part of the work focused in the simulation of the mechanical response of block copolymers. The influence of chain architecture on the mechanical properties was investigated: our finding reveals an important role of the bridging molecules (cilia chains and knotted loop chains) on the stress transmission between phases at high strain.
The initiation of plasticity in copolymer samples was also studied. The role of the buckling has been found to be determinant in the mechanical response of the sample
The dependence of the buckling instability with the sample size and the deformation rate was investigated. We have found that the fundamental (first) mode of buckling develops at relatively low strain rate whereas at high strain rate the buckling of the sample occurs with the second or higher mode of buckling.
A new model that takes into account the buckling kinetic was developed to describe this competition between the buckling modes.

Keywords: plasticity, molecular dynamics simulation, polymers, mechanical properties, nanostructured polymers, bloc copolymers, buckling instability.

RESUME

Les propriétés mécaniques des polymères et des copolymères à blocs ont été étudiées par simulation de type dynamique moléculaire (modèle billes-ressorts). Les échantillons polymères ont été générés par la méthode de « radical like polymerisation ». Ces échantillons ont été soumis à des essais de traction uniaxiaux et triaxiaux dans le but d'étudier leurs réponses mécaniques.

Dans la première partie de ce travail on a comparé deux méthodes de traction : « méthode de traction homogène» et la traction « pilotée par les bords » de l'échantillon. Les résultats montrent que les deux méthodes sont équivalentes à faible vitesse de traction.
Le changement de distance entre enchevêtrement dans un polymère modèle sous traction est analysé, les résultats montrent que le désenchevêtrèrent des chaines est plus prononcé lorsque la déformation de l'échantillon est uniaxiale du fait de la relaxation latérale de l'échantillon.
La nucléation des cavités dans les polymères amorphes soumis à une déformation triaxial a été également étudiée. On a trouvé que les cavités se forment dans des zones qui sont caractérisées par un faible module d'incompressibilité élastique. Ces zones sont identifiables dès le début de la déformation à une température très basse (T~0K).

La seconde partie de ce travail se concentre sur la simulation de la réponse mécanique des copolymères à blocs. L'influence de l'architecture moléculaire sur le comportement mécanique de l'échantillon a été analysée. Les résultats montrent que le comportement mécanique des échantillons est piloté par le taux des chaines liantes qui assurent la transmission des contraintes entre les phases.

Le flambement des lamelles dans les copolymères à blocs a été également étudié, l'influence de la taille de l'échantillon et de la vitesse de déformation sur la réponse mécanique de l'échantillon a été explorée. Les résultats montrent un changement de mode du flambement selon la vitesse de déformation imposée.
Un nouveau modèle qui prend en compte le facteur cinétique du flambement est proposé pour décrire la compétition entre les modes.

Mots-clés : plasticité, polymères, propriétés mécaniques, simulation par dynamique moléculaire, polymères nanostructuré, copolymères à blocs, flambement des lamelles.